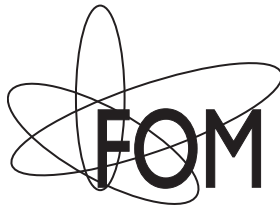


**Optical control of mesoscopic
spin ensembles in gallium arsenide**



Zernike Institute PhD thesis series 2015-17

ISSN: 1570-1530

ISBN: 978-90-367-8145-9 (printed version)

ISBN: 978-90-367-8146-6 (electronic version)

The work described in this thesis was performed in the research group Physics of Nanodevices of the Zernike Institute for Advanced Materials at the University of Groningen, the Netherlands. Funding was mainly provided via the research programme of the Foundation for Fundamental Research on Matter (FOM), which is part of the Netherlands Organisation for Scientific Research (NWO). During the final years of this project, it was embedded in a project funded by the European Research Council via ERC Starting Grant 279931. The project did profit from facilities funded through the Dutch national NanoLabNL initiative.

The cover graphic is an adaptation of an original from R.H. Thurston's *A history of the growth of the steam-engine* (D. Appleton & Company, New York, 1886)

Printed by Ipskamp Drukkers, Enschede



university of
 groningen

Optical control of mesoscopic spin ensembles in gallium arsenide

PhD thesis

to obtain the degree of PhD at the
 University of Groningen
 on the authority of the
 Rector Magnificus Prof. E. Sterken
 and in accordance with
 the decision by the College of Deans.

This thesis will be defended in public on
 Friday 23 October 2015 at 14.30 hours

by

Alexander Reinier Onur

born on 24 August 1983
 in Groningen, the Netherlands

Supervisor

Prof. C. H. van der Wal

Assessment committee

Prof. R. J. Warburton

Prof. Y. V. Nazarov

Prof. K. H. K. J. Jungmann

Abstract

This PhD thesis describes experiments and theory on the interaction of coherent light with the magnetic moment of localized electrons in a semiconductor. The prospects for achieving accurate control of the electrons spin are discussed, particularly addressing the limitations imposed by disturbance from surrounding nuclear spins. It is argued that feedback control is the way to stabilize the combined system of electrons and nuclei. It is demonstrated how this can be achieved using only laser excitation and exploiting the hyperfine interaction in the system.

Samenvatting

Dit proefschrift beschrijft experimenten en theorie over de koppeling tussen coherent licht en het magnetisch moment van gelokaliseerde elektronen in een halfgeleider. De vooruitzichten om nauwkeurige controle te krijgen over de elektronspin worden besproken, in het bijzonder de beperkingen hierin door verstoringen van omliggende kernspins. Er wordt beargumenteerd waarom controle met terugkoppeling een goede manier is om het samengestelde systeem van elektron- en kernspins te stabiliseren. Gevolgd door een demonstratie van hoe dit effect bereikt wordt door slechts gebruik te maken van laser excitatie van het elektron en de hyperfijn koppeling in het systeem.

Acknowledgements

The work described in this thesis has contributions from many people with whom I have had the privilege to work.

First of all I thank prof. Caspar van der Wal, my promotor. For introducing me to this subject of quantum optics and control of spin ensembles and for his guidance, patience and advise throughout the project. Also, for taking care of a good atmosphere in our team, which is one of the most important preconditions to enjoy work and be productive. I thank the members of the assessment committee, prof. Klaus Jungmann, prof. Yuli Nazarov, and prof. Richard Warburton, for taking the time to critically read this thesis and provide useful comments and suggestions where necessary.

Then my coworkers in the Quantum Devices team: With Alok Chaubal I shared several years of overlap during our PhD tenures. It was first and foremost very enjoyable to spend that time together. Regarding work I am greatly indebted to a wide range of physics discussions that we had while we were exploring the donor bound spin system and for his design of the multifiber optical microscope and his generally excellent skills in laser optics, which are almost as good as his skills in cooking. Similar words of thanks hold for Jakko de Jong and Danny O'Shea, who have made major contributions to chapters 4 and 5 of this thesis. I acknowledge both of them for giving the measurement setup a major upgrade, many results in this thesis could not have been obtained without it. I thank Maksym Sladkov and Morten Bakker for introducing me to the measurement setup in the early phase of my PhD, Jorrit Sloot and Rianne Lous for valuable contributions to the early DNP measurements, Rob Bremer for his contributions to theoretical understanding of the DNP process and Carmem Gilardoni, Urvashi and Sebastien Volker for contributing to the research by

their MSc and BSc projects they did in our team. I thank Sergii Denega, Olger Zwier, Xu Yang, Gerjan Lof, Diederik Perdok, Angad Singh, Xavi Bonet-Monroig and Javaid Iqbal for help and useful discussion while they worked on other projects within the team.

For valuable discussions I thank dr. Audrius Alkauskas and dr. Valerii Zapaskii, whose visits to Groningen brought insightful comments on the theoretical aspects of this work. I also want to acknowledge helpful discussion with dr. Kirill Kavokin and prof. Vladimir Korenev whom I had the pleasure of meeting at the PLMCN14 conference. I thank prof. Susanne Yelin and dr. Renuka Rajapakse for their hospitality and discussions during my stay in Cambridge and visit to Storrs. During my PhD I have also spent a fair amount of time in Delft, where Marco van der Krogt and Marc Zuiddam helped me to make waveguides out of the GaAs thin films at the Kavli Nanolab. I learned a lot about semiconductor fabrication techniques from them. I am thankful to prof. Andreas Wieck and prof. Dirk Reuter for growing the GaAs samples that were used in this work and for providing feedback on our measurements and articles.

Throughout this project I have very much appreciated the technical support of Siemon Bakker, Bernard Wolfs, Johan Holstein, Martijn de Roos, Herman Adema and Tom Schouten who keep the labs operational and very often the mood enjoyable. Also, Anna McEwan, for being supportive in many ways but also for being a focal point in the group who is always available to talk to, thank you very much.

For general discussions at group meetings, but also for the pleasant interaction at work that is not research related, I thank all the members of the Physics of Nanodevices group: prof. Bart van Wees and prof. Tanalika Banerjee, Aisha Aqeel, Jasper van den Berg, Madhu Bettadahalli, Ludo Cornelissen, Arjit Das, Kumar Sourav Das, Mallik Guram, Pep Ingla Aynes, Sander Kamerbeek, Alexey Kaverzin, Christian Leutenantsmeyer, Jing Liu, Siddhartha Omar, Saurabh Roy, Roald Ruiters, Juan Shan, Nynke Vlietstra, Eric de Vries and Paul Zomer. And former members: Marcos Guimares, Alina Veligura, Gaurav Rana, Subir Parui, Magdalena Wojtaszek, Fasil Dejene, Thomas Maassen, Joost Flipse, Juliana Brant, Juliane Junesh, Vishal Ranjan, Sander Blok, Vincent Cas-

tel, Andres Castellanos, Arramel, Frank Bakker, Bram Slachter, Nico Tombros, Jean-Paul Adam, Eek Huisman and Iván Vera Marín.

To my friends and family I express thanks for their support, especially during the times when work became demanding and there was less time to spend together. And of course for providing the sometimes very much needed distraction. I am very lucky to have you all in my life.

I thank my parents for giving me my education, freedom and encouragement to choose a path of development and their warm support throughout that journey.

Sander Onur
Groningen
September 21, 2015

Contents

Abstract	v
Samenvatting	vi
Acknowledgements	vii
1 Introduction - Engineering strong light-matter coupling for quantum technologies	1
1.1 Motivation	1
1.2 Why quantum technology?	2
1.3 This thesis: Coherent coupling between photons and bound electron spins in GaAs	4
2 Optical control of donor-bound electron spins in GaAs	7
2.1 Silicon donor in gallium arsenide	7
2.2 Optical interaction with a three level Λ -system	12
2.3 Electromagnetically induced transparency	15
2.4 Electron-nuclear spin interaction in GaAs	16
2.5 Measurement of EIT	24
3 Measurements of the local nuclear spin distribution by electromagnetically induced transparency	29
3.1 How the EIT lineshape reflects the nuclear spin state	30
3.2 Detection of optically induced dynamic nuclear polarization	31
3.3 Timescale of optically induced DNP buildup	32
3.4 Bidirectionality of DNP in the Λ -system	33
3.5 Invasiveness of the detection method	36
3.6 Dependence on pump laser intensity	37

4	Two-laser dynamic nuclear polarization with semiconductor electrons: feedback, suppressed fluctuations, and bistability near two-photon resonance	41
4.1	Introduction	42
4.2	Candidate Λ -system: D^0X in GaAs.	43
4.3	Influence of Overhauser field on CPT	46
4.4	Hyperfine coupling	47
4.5	Influence of CPT on DNP: feedback	49
4.6	Stochastic dynamics of the nuclear spin polarization	50
4.7	Results of the model	51
4.8	Conclusion	53
4.9	Supplementary Information	55
5	Stabilizing nuclear spins around semiconductor electrons via the interplay of optical coherent population trapping and dynamic nuclear polarization	65
5.1	Introduction	66
5.2	Experimental methods	67
5.3	Measurement of the nuclear spin distribution by CPT	68
5.4	DNP near the CPT resonance	69
5.5	Observation of one and two stable states	71
5.6	Laser power and frequency dependence of the CPT splitting	72
5.7	Time-dependent measurements	73
5.8	Conclusion	74
6	Optically induced dynamic nuclear spin polarization in n-GaAs mediated by shallow donor electrons	77
6.1	Introduction	78
6.2	X and D^0X magnetospectroscopy	79
6.3	Measurement of DNP near donors	83
6.4	Spectral dependence of DNP	87
6.5	Conclusions	91
7	Magnetospectroscopy of the bound trion levels	95
7.1	Introduction	96

7.2	Motivation for the study	96
7.3	Complementary spectroscopy	96
7.4	Results	97
7.5	Conclusion	101
8	Experimental methods	105
8.1	Sample preparation	106
8.2	Polarization maintaining fiber microscope	107
8.3	Multi-fiber microscope	108
8.4	Differential transmission spectroscopy	119
9	Conclusion and outlook	125
	Appendices	129
A	Epitaxial lift-off recipe	131
B	Microscope input/output analysis	133
	Wetenschappelijke samenvatting	139
	Scientific summary	145
	List of publications	151

Chapter 1

Introduction - Engineering strong light-matter coupling for quantum technologies

1.1 Motivation

The question that motivates the research described in this thesis is: Can the spin of localized electrons bound to impurities in a semiconductor serve to store a pulse of light? Realizing this would be a small step in a much larger (global) effort that strives to develop a new generation of faster, more energy efficient electronics that relies not only on conventional electron charge transport, but also uses light as well as the electron's spin as information carriers. This field, which is still taking shape, is commonly referred to by labels such as 'optoelectronics' or 'spintronics'. Manipulating light-matter interaction in this way is also important for quantum information science. The desire to use light as information carrier stems in one part from the fact that it moves at the ultimate speed. Optical fiber technology is nowadays widespread because it facilitates high-speed data transmission. To achieve high speed in electronic components such as integrated circuits, these devices have to be reduced in size (to reduce the distance traveled by the electrons). Current technology has rapidly approached the limit where the size of components is only tens of atoms. Besides that one atom would be a fundamental size barrier, at the current lengthscale there are other significant drawbacks, such as heating of the components due to resistivity in the circuit. This highlights another aspect of light, that it moves freely through space or along properly designed guiding structures. Energy consumption can thus be reduced by

developing an equivalent of electronic circuits based on light. However the last point relates to a major difficulty for using light in circuit-like components: it is more difficult to control than electrons, especially at small scale. Electronic currents can be switched (notably in a three-terminal transistor configuration) and electronic energy can be stored in memory elements. For light such active components are still being developed.

A final interesting prospect is that photons can mediate coherent interaction between material systems, while traveling over long distances. This makes optical circuit technology promising for quantum information applications: Quantum mechanics is at the heart of how all modern computers work, through CMOS technology. Quantum computers however aim to use quantum mechanical properties (such as state coherence) of the units on which computation is actually performed, the bits of information. With electron spins as a prime candidate of a material system that shows a high degree of coherence, even inside a crystal where the environment is very crowded with other (quasi)particles, it is desirable to create an interface between the two. Such an interface should allow to transfer the state of photons to the quantum state of electron spins and vice versa.

1.2 Why quantum technology?

The last point of the previous section is particularly interesting from a scientific point of view. Because the fundamentals of quantum physics still pose many open questions [1], it is therefore of current importance to keep extending the number of experimental testing grounds. The prospect of applications is however another matter. The use of scientific discovery can often not be envisioned at the moment when the discovery is done. For example, the first demonstration of a Maser proposed that it be used as a low noise amplifier and that it "may be useful in a restricted range of applications". Specifically, the authors suggest that it could serve to amplify microwave signals from outer space. The subsequent discovery of the Laser was first thought to be mainly useful for atomic spectroscopy. These scientists could not possibly have foreseen that laser beams would soon be used for precision cutting in industry and for surgical techniques,

and that they would connect people around the world by enabling fiber optic communications technology. The present quest for realizing quantum technologies could well be at a comparable stage. There is a general sense that it is important, but no guarantee that the applications we think of now are the ones that will have most impact. Not being able to look into the future we have to motivate ourselves with the main candidates we have now: quantum communication (mainly the aspect of cryptography) and quantum computation. The physical requirements for both applications concern to a large extent the same challenges, and we will further examine here the quantum computer to see what quantum technology is and what the challenges are.

Quantum computers aim to use quantum mechanical properties of the units on which computation is actually performed, the bits of information. To understand what the requirements for this are we look at the heart of the theory: The discovery of wave-particle duality led to a theoretical framework where the state of every physical entity is properly described by a wave function. The wave function contains probabilistic information of all properties of the system, it evolves according to the equations of motion in a deterministic way. But, curiously, measurement outcomes are given by the square of the wave function. The consequence of this is that the wave function can be multiplied by a complex phase factor without altering the measurement outcome. In the case of two systems (x and y) that have (hypothetically) never interacted the wave function of the combined system is $\psi_x\psi_y$, resulting in multiplication of probabilities in the classical sense. But when systems have a history of interaction there wave function will be ψ_{xy} which is generally not separable as a product of single system wave functions. When this is the case measurements on x influence measurements on y (and vice versa) in a way that has no counterpart in classical physics. The interaction in the past leads to this entanglement. Studies of entanglement have a history that goes back to the Einstein-Podolsky-Rosen paradox and the Bell inequalities, and is still central in current fundamental research (for a review see [2]).

Entanglement can be stronger or weaker depending on the interaction that caused it. For entangled systems the phase factor becomes important

and deterministic evolution of systems x and y with retention of their relative phase (i.e. coherent evolution) preserves the entanglement. In the context of quantum computing the systems x and y can be considered qubits and the inclusion of phase enables them to carry more information than classical bits. Proposals for quantum computing using qubits involve preparation of the states of the qubits, planning of the sequence of subsequent interaction between qubits (the interaction is the computation step) and readout of the final state of the qubits. After the interaction steps take place as planned the final state yields the result of the computation.

However, if system x subsequently has interaction with a system z they in turn become entangled and the triplet of particles (x,y,z) are now entangled together. When the interaction with z happened unknowingly (because during an experiment e.g. it is a particle in the environment that is not tracked and measured) it interrupts the deterministic, coherent evolution of the entangled pair (x,y) for the observer who is only tracking x and y . There cannot be a deterministic equation of motion for x and y that takes such interaction events (that can be described as scattering processes) with z into account, hence they must be added in the form of probabilistic decoherence (for elastic scattering) and decay (for inelastic scattering) processes. For quantum computation to be successful the computation should finish before decoherence and decay disturb the system.

Based on the foregoing discussion we can establish that in a quantum computer the objective is to keep the system isolated from the environment (at least as long as it takes to compute) and to make interactions within the system deterministic. Spins and photons are considered to in principle be able to fulfill the former, the latter requires the designed spin-photon coupling to be 'strong' which basically means that a photon should not miss its destination.

1.3 This thesis: Coherent coupling between photons and bound electron spins in GaAs

In this thesis we work with an ensemble of electron spins bound to Si donors in GaAs with the aim to use this material to store and retrieve a pulse of light. To this end we focus on measurement of electromagnetically

induced transparency (EIT) in the system. This effect is an important precursor to many methods in quantum communication [3, 4, 5] and also, but to a lesser extent, quantum computing [6].

We demonstrate EIT, but show that the interaction of the electron spin with the nuclear spins poses a severe difficulty for proceeding beyond this. These nuclear spins are in fact untracked particles in the environment of the system that we wish to control, in the sense it was discussed in the previous section. However the nuclear spins form a special type of environment which moves slowly compared to the dynamics of the electron. In contrast to a Markovian environment which is the same at every instant, the nuclear spin environment can be changed. In the main chapters of this thesis we develop and test a method that can prepare the nuclear spins in a state of reduced fluctuations, in order to extend the electron spin dephasing time. In the experiments we find partial confirmation of our method and point out several issues that can be improved on the experimental method.

The thesis is built up as follows: Chapter 2 is a technical introduction to the donor-bound electron system in GaAs, to electromagnetically induced transparency, and dynamic nuclear spin polarization. These are topics that are fundamental to the research described in this thesis. In Chapter 3 presents how electromagnetically induced transparency can be used to measure nuclear spin polarization. Optically-induced dynamic nuclear spin polarization (DNP) is demonstrated and its dynamics is characterized. Chapter 4 introduces the proposal for a technique to reduce nuclear spin fluctuations through DNP. It is shown that when the DNP is induced by two lasers that are on a two-photon resonance condition, this can have a stabilizing effect on the nuclear spins. Chapter 5 presents measurements that test the model and proposed control technique of Chapter 4. In Chapter 6, more details of the DNP process are studied, in particular the dependence on photon energy of the light that induces it. Chapter 7 shows spectroscopy measurements of the system in a magnetic field in order to resolve the level structure of the donor-bound exciton. Chapter 8 describes the methods used to do the experiments described in the earlier chapters, in particular the sample preparation, microscope

design and spectroscopy technique. Finally, conclusions from the various chapters are grouped and presented in Chapter 9.

References

- [1] Schlosshauer, M., Kofler, J. & Zeilinger, A. A snapshot of foundational attitudes toward quantum mechanics. *Studies in History and Philosophy of Science Part B: Studies in History and Philosophy of Modern Physics* **44**, 222 – 230 (2013).
- [2] Horodecki, R., Horodecki, P., Horodecki, M. & Horodecki, K. Quantum entanglement. *Rev. Mod. Phys.* **81**, 865–942 (2009).
- [3] Duan, L.-M., Lukin, M., Cirac, J. I. & Zoller, P. Long-distance quantum communication with atomic ensembles and linear optics. *Nature* **414**, 413–418 (2001).
- [4] Chaneliere, T. *et al.* Storage and retrieval of single photons transmitted between remote quantum memories. *Nature* **438**, 833–836 (2005).
- [5] Sangouard, N., Simon, C., de Riedmatten, H. & Gisin, N. Quantum repeaters based on atomic ensembles and linear optics. *Rev. Mod. Phys.* **83**, 33–80 (2011).
- [6] Beausoleil, R., Munro, W., Rodrigues, D. & Spiller, T. Applications of electromagnetically induced transparency to quantum information processing. *Journal of Modern Optics* **51**, 2441–2448 (2004).

Chapter 2

Optical control of donor-bound electron spins in GaAs

2.1 Silicon donor in gallium arsenide

The GaAs crystal structure is of the zinc-blende type, with lattice constant $a \approx 5.65 \text{ \AA}$ and an atomic number density of $\rho = 4.42 \times 10^{22} \text{ cm}^{-3}$. The valence (p-like) and conduction (s-like) band structure around electron wave number $k = 0$ are depicted in Fig. 2.1. At a temperature of 4.2 K the material has a direct bandgap of 1.51 eV, furthermore the valence band has a split-off part that is separated by $\Delta_{SO} = 0.34 \text{ eV}$ from the heavy/light hole parts. Silicon can substitute as a donor (in place of gallium) within the crystal, leading to n-type doping of the material, or as an acceptor (in place of arsenic), leading to p-type doping. Generally, both can occur simultaneously. However, under highly controlled growth conditions, crystals containing mostly donors and no acceptors can be produced. An isolated and non-ionized (electrically neutral) donor system is denoted as D^0 . Within the band diagram the donor electron energy is located just below the conduction band, indicating that the electrons are nearly free (i.e. it is a shallow donor). Their atomic wave function closely resembles that of the conduction band electrons (s-type Bloch function), but is additionally modified by a slowly varying envelope function that represents the electrostatic binding to the silicon atom. Within the effective mass approximation this part of the wave function resembles a hydrogen-like 1S, i.e. exponentially decaying along radius r , envelope. This is a solution

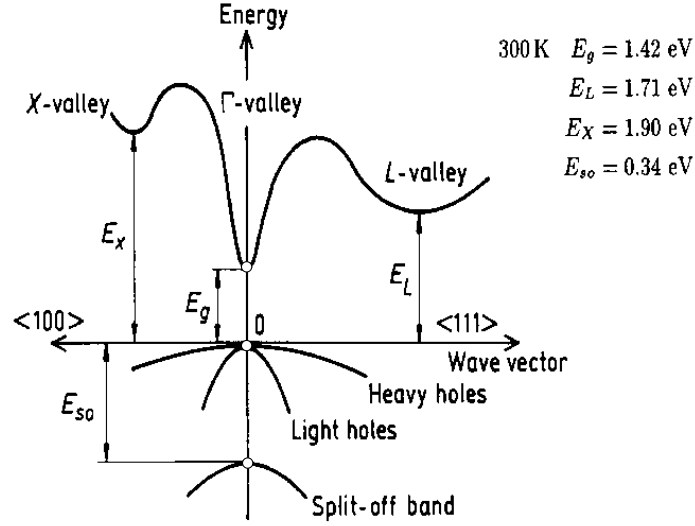


Figure 2.1: Band structure of GaAs at room temperature.
 (Source: <http://www.ioffe.ru/SVA/NSM>, dated 18 June 2015)

to the differential equation

$$\left(-\frac{\hbar}{2m^*} \left(\frac{\partial^2}{\partial r^2} + \frac{2}{r} \frac{\partial}{\partial r} \right) - \frac{e^2}{4\pi\epsilon r} \right) F(r) = EF(r). \quad (2.1)$$

Taking the dielectric constant $\epsilon = 12.56\epsilon_0$ and electron effective mass $m^* = 0.067m_e$ for GaAs results in an effective Bohr radius of $a_0 = 99 \text{ \AA}$ and a radial envelope function:

$$F(r) = \sqrt{\frac{1}{\pi a_0^3}} e^{-r/a_0}, \quad (2.2)$$

which is normalized according to $\int_{\text{space}} F(\mathbf{x})^* F(\mathbf{x}) d\mathbf{x} = 1$. To fully describe the electron density this envelope function is multiplied by the $k = 0$ Bloch function $u_0(\mathbf{x})$, where 0 labels the band index and hence comprises the s-like character of the D^0 orbital. In the effective mass approximation the ionization energy, obtained from solving Eqs. 2.1 and 2.2 at $r = a_0$, is 5.8 meV. Measured values for the donor ionization energy yield 6 meV. This energy corresponds to a temperature of ~ 70 K.

If the temperature is well below 70 K the thermal excitation of donor-bound electrons to the conduction band is suppressed. Additionally, if

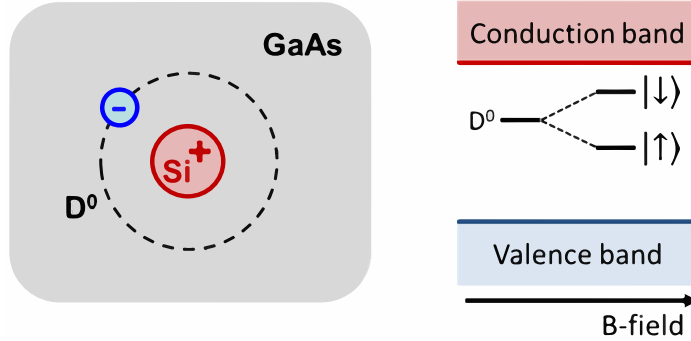


Figure 2.2: Left: The D^0 system in GaAs. Right: situated within the bandgap the bound electron provides an isolated energy level. The degeneracy is lifted by application of an external magnetic field, hence providing two localized states.

the donor density is well below the metal-insulator transition, which is around 10^{16} cm^{-3} , electron hopping between donors is also suppressed. If both these conditions are fulfilled, the donor-bound electrons can be considered as an ensemble of localized, non-interacting electrons within the GaAs crystal (see 2.2).

2.1.1 Magnetic properties

The spin-orbit (SO) interaction in GaAs modifies the response of the electrons to an external magnetic field, which is reflected in the electron g -factor of $g_e \approx -0.42$. This modification of the g -factor as compared to the free electron (which would display a value of $g_e = 2.0023$) indicates that the SO interaction mixes the pure spin states. An important consequence of this mixing is that it allows for spin relaxation by fluctuating electric fields. In clean samples these electric field fluctuations can be attributed to lattice vibrations and hence it is the (inelastic) interaction with phonons that dominates the spin relaxation process [1, 2]. However for donor-bound electrons the extent of their wavefunction (or simply their size) is small (of the order of a_0), while the density of phonons at wavelengths smaller than a_0 is strongly quenched at liquid helium temperature. The spin relaxation time, denoted by T_1 , for donor-bound electrons has been measured to be at least 3 ms in moderate magnetic fields (up to 4 T)

and was shown to decrease with B^{-4} for higher magnetic fields [3], having a value $T_1 = 770 \mu\text{s}$ at 6 T.

Additionally the donor-bound electron spin experiences dephasing due to elastic collisions with environmental degrees of freedom. The characteristic time for this process is denoted by T_2 and it generally holds that $T_2 \leq 2T_1$ since inelastic relaxation also reinitializes the phase. For donor-bound electrons in GaAs it was measured by optical spin-echo technique that at least $T_2 = 7 \mu\text{s}$ [4].

In experiments that measure the spin dynamics it is of practical necessity to measure a number of spins, i.e. either to measure a single spin many times in a row or to measure an ensemble of spins at once. In this thesis we do the latter. In these realistic cases one deals with the inhomogeneous dephasing time, T_2^* , which captures all inhomogeneities that affect spin dephasing. Inhomogeneity can be caused by electric strain fields (causing g-factor broadening through the SO-interaction), impurity electric fields and hyperfine interaction. Measurements have shown an inhomogeneous dephasing time for bound electrons in GaAs of the order of several nanoseconds, depending on temperature, impurity concentration and external magnetic field. For the case of clean, strain-free samples it is well established that the hyperfine interaction of the electron spin with nuclear spins is the dominant cause for the shorter T_2^* . This thesis focuses on controlling this hyperfine interaction and an elaborate discussion of the mechanism is discussed separately in Sec. 2.4.

2.1.2 Donor bound trion: a localized optical excitation

The Si impurity in GaAs also supports an excited state, where an additional electron-hole pair stays bound to the impurity site by the Coulomb force. This type of bound exciton state, first proposed by Lampert [5], is commonly called a trion state when bound to a neutral donor such as Si to emphasize the fact that three effective mass particles are bound to the impurity site.

The D^0X size determines much of its optical properties [6]: Because the wavelength of the excitation light inside the medium is larger than $2a_0$, approximately the D^0X diameter, the atomic dipole moments add coher-

ently, which results in large oscillator strength and short lifetime. Indeed the lifetime of D^0X has been measured by photoluminescence [7] to be 1.07 ns at 1.6 K. Also, the D^0X wave function stretches over many lattice sites (there are approximately 170.000 lattice sites in a sphere of $4\pi\rho a_0^3/3$) which polarize coherently during excitation [6]. Therefore, the excitation and emission display almost no vibronic coupling as is often the case for deep defects where the exciton size is localized on a few lattice sites. The fact that phonons do not play a part results in narrow absorption and emission lines for D^0X in GaAs.

The orbital motion of the three charged particles around the donor core ion, moving in each others electric potential poses, a hard problem for which only approximate solutions have been proposed [8]. When an external magnetic field is applied the energy level shifts are dominated by a strong diamagnetic shift. Together with the SO-coupling this complicates the analysis even further [9]. In Chapter 7 we spend separate attention to the nature of the trion states and also present accurate measurements of their energies in a magnetic field. To discuss the possibilities of optical excitation it is sufficient to point out that the magnetic field lifts the degeneracy and a specific level can be addressed in practice, provided the other levels are sufficiently far removed in energy by application of the magnetic field.

2.1.3 Optical orientation of the D^0 electron spin

Optical orientation is the process where a net magnetic moment builds up in a material by shining light on it. For the single atom/particle case it means controllably orienting a net spin by interaction with light. That this can be done is not obvious because, in the electric dipole approximation, it is the electric component of the light that induces a change in the electronic wave function through the electric dipole moment. This interaction can at first glance only induce changes in the electronic orbital motion (i.e. the charge distribution) and not in the spin part. However, in the presence of the spin orbit interaction the situation changes: spin and orbital components of the wave function mix. In particular for the exciton states in GaAs which contain a hole from the valence band, whose orbital

angular momentum $L = 1$ and the total angular momentum $J = 3/2$, this effect is significant. In the state representation

$$|J, m_J\rangle = \sum_{m_L} \sum_{m_S} \langle L, m_L, S, m_S | J, m_J \rangle |L, m_L, S, m_S\rangle, \quad (2.3)$$

where L, S and J are orbital, spin and total angular momentum respectively and $\langle L, m_L, S, m_S | J, m_J \rangle$ are the Clebch-Gordan coefficients that characterize the mixing. The state $|J, m_J\rangle$ now being a superposition of pure spin states can transfer of population between pure spin states of different m_s . GaAs, a material where spin orbit interaction is significant, is therefore a good material for this optical orientation process. More detailed background on this topic can be found in [10, 11] and a detailed study of the case of the trion and bound electron states in GaAs is treated in [12].

Optical orientation can be used on the bound electron spin states in GaAs because they have a transition dipole to a common excited state. This is beneficial for gaining control of the spin because the optical orientation can take place very fast, as compared to the lifetime of the spin state.

2.2 Optical interaction with a three level Λ -system

The spin states of the bound electron, optically coupled to a trion state, form a Λ system (due to its shape, see Fig. 2.3). In this section we analyze the optical excitation process in this system and pay particular attention to the effects of coherent population trapping, which is characteristic to this system and can be used to prepare a coherent superposition of the two ground states.

2.2.1 Dressed states the driven Λ -system

The atomic system is treated as point-like and interacting with the external electromagnetic field in the dipole approximation. We take the atomic and interaction parts of the Hamiltonian as

$$H_0 = \sum_{i=1}^3 \hbar\omega_i |i\rangle \langle i|, \quad V(t) = -\boldsymbol{\mu}\mathbf{E}(t) \quad (2.4)$$

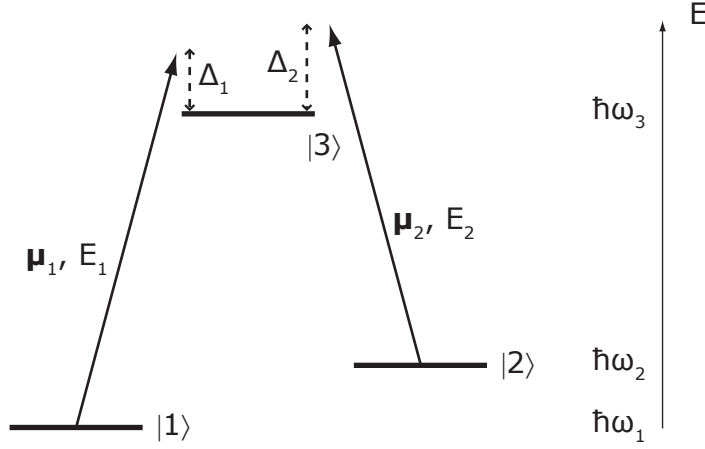


Figure 2.3: Generic depiction of a driven Λ -system consisting of states $|1\rangle$, $|2\rangle$ and $|3\rangle$ where lasers address the 1-3 and 2-3 transitions. The 1-2 transition is dipole forbidden, making state $|2\rangle$ relatively long-lived as compared to $|3\rangle$.

where ω_i are the energies of the atomic levels. The dipole operator is $\boldsymbol{\mu} = \boldsymbol{\mu}_1 |3\rangle \langle 1| + \boldsymbol{\mu}_2 |3\rangle \langle 2| + \text{h.c.}$, and we assume that the dipole moments are orthogonal [13]. The applied electric field is

$$\mathbf{E}(t) = \frac{\mathbf{e}_1 E_1}{2} e^{-i(\omega_3 - \omega_1 + \Delta_1)t} + \frac{\mathbf{e}_2 E_2}{2} e^{-i(\omega_3 - \omega_2 + \Delta_2)t} + \text{c.c.} \quad (2.5)$$

where \mathbf{e}_i are polarization vectors such that $\boldsymbol{\mu}_i \mathbf{e}_j = \mu_i \delta_{ij}$. The electric field thus consists of two modes that are orthogonally polarized at frequencies that match the atomic transitions plus detunings Δ_i , they have amplitudes $|E_i|$.

After defining zero energy to be $\hbar\omega_1$, applying the rotating wave approximation and making the transformation to a rotating frame for which

$$|1\rangle \longrightarrow |1\rangle, \quad (2.6a)$$

$$|2\rangle \longrightarrow e^{-i(\omega_2 + \Delta_1 - \Delta_2)t} |2\rangle, \quad (2.6b)$$

$$|3\rangle \longrightarrow e^{-i(\omega_3 - \omega_1 + \Delta_1)t} |3\rangle, \quad (2.6c)$$

the full Hamiltonian in matrix representation becomes:

$$H = H_0 + V = -\frac{\hbar}{2} \begin{pmatrix} 0 & 0 & \Omega_1^* \\ 0 & 2(\Delta_1 - \Delta_2) & \Omega_2^* \\ \Omega_1 & \Omega_2 & 2\Delta_1 \end{pmatrix} \quad (2.7)$$

where the Rabi frequencies are defined as $\Omega_i = \mu_i E_i / \hbar$. At two-photon resonance, i.e. when $\Delta_1 = \Delta_2 \equiv \Delta$ the characteristic polynomial of H is $\lambda^3 + 2\Delta\lambda^2 - (|\Omega_1|^2 + |\Omega_2|^2)\lambda$. Hence it has an eigenstate at zero energy corresponding to the eigenvector $(1, -\Omega_1/\Omega_2, 0)$. This dressed eigenstate of the system composed of atom and fields does not contain the bare atomic state $|3\rangle$. In the following section we discuss how this state can play a special role in more realistic three-level system dynamics.

2.2.2 Open system dynamics

To describe a more realistic case the previously depicted Λ -system must be augmented with appropriate decay, and dephasing rates (as it is depicted in e.g. Fig. 4.1). These describe processes that arise from interactions with the environment. Such processes, too complex to take into account in the deterministic Hamiltonian description, cause the emergence of statistical uncertainty in the evolution of the system. To deal with such an open system the state can be described by the density matrix and the evolution by a Lindblad master equation. This type of evolution is conveniently pictured in phase space, where the system takes up a certain volume and follows a particular trajectory during its evolution. The size of the phase space volume is a measure of uncertainty in knowledge about the state of the system. When the Λ -system is driven by lasers it is brought out of thermodynamic equilibrium, and the contact with the environment gives rise to dissipative processes. A special situation arises when the dissipative system has a so-called dark state, as described in the previous section to exist when the two-photon resonance condition is met: This state, denoted $|\psi_d\rangle = (\Omega_2 |1\rangle - \Omega_1 |2\rangle) / \sqrt{\Omega_1^2 + \Omega_2^2}$, is decoupled from the primary dissipative process in this system, which is spontaneous emission (the corresponding operators of which are proportional to $|2\rangle\langle 3|$ and $|1\rangle\langle 3|$). Because there are no other states with this property all other initial states will be subject to spontaneous emission and, after several optical excitation and emission cycles, end up in the dark state $|\psi_d\rangle$. This form of dissipative state preparation in the Λ -system is called coherent population trapping (CPT), since the state $|\psi_d\rangle$ is a pure state. The simplest example is optical orientation with a single laser, in that case one of the Rabi fre-

quencies is zero. For example, when $\Omega_1 = 0$ the state $|\psi_d\rangle = |1\rangle$. However, by controlling relative power and phase of the laser Rabi frequencies any coherent superposition of states $|1\rangle$ and $|2\rangle$ can be prepared and subsequently manipulated [14]. Despite of the state $|\psi_d\rangle$ being decoupled from spontaneous emission it is still subject to decay and dephasing between states $|1\rangle$ and $|2\rangle$, which are the electron spin states in our work. The spin decay and dephasing rates thus set limits on the lifetime of $|\psi_d\rangle$, but because these times can be relatively long compared to the time required for optical preparation and manipulation the CPT method provides a viable path towards coherent control over a qubit formed by the two ground states of a Λ -system. The mathematical formalism of CPT is described in e.g. [15, 11], which we use to formulate the equation of motion for our system (shown explicitly in Sec. 4.9.1).

2.3 Electromagnetically induced transparency

An effect closely related to CPT is electromagnetically induced transparency (EIT). Whereas in CPT the focus is on the state of the atomic system that is being prepared, EIT focuses on the effect on the propagating laser fields through a medium containing the Λ -systems. Inside this medium there arises an effective interaction between the photons of both lasers, mediated by the Λ -system. The susceptibility for laser 1 is therefore conditional on the presence of laser 2, and vice versa. When the two-photon resonance condition is met the scattering of laser light by spontaneous emission is suppressed. What remains is that photons are exchanged between the modes of laser 1 and 2 while maintaining coherence, mediated by the coherent evolution of the Λ -system, thus there is (ideally) no extinction of the laser beams in the medium. Without the presence of the other laser the medium appears opaque. EIT thus allows for a transistor-like effect where transmission of photons in a laser mode can be allowed by the presence of another laser. This optical switching has been demonstrated to be possible [16] and is valuable for the development of all-optical devices.

Practically the CPT state could be detected by measuring a decrease in fluorescence due to suppressed spontaneous emission. EIT is by definition

measured in transmission which is the main detection method used in subsequent chapters in this thesis.

2.4 Electron-nuclear spin interaction in GaAs

The dynamics of the composite system of electron and surrounding nuclear spins spans many timescales: from the subnanosecond optical orientation process up to the long decay time for the bulk nuclear spins which can last for hours, depending on temperature and magnetic field. To discuss these processes we subdivide this section and consider first only the nuclear spin bath, at equilibrium. Then the coupling of the electron spin to this bath and the influence of this on the electron spin coherence time. Then the way to modify the state of the nuclear spin bath by exerting control on the electron spin. Finally, the coupling of a polarized (local) nuclear spin bath to the rest of the nuclei in the bulk of the crystal, which leads to a flow of nuclear spin polarization away from the D^0 systems by a diffusive type of process.

2.4.1 Thermal equilibrium of nuclear spin bath at 'high' temperature

For the nuclear spin environment in thermal equilibrium with the lattice we consider a number, N , of non-interacting nuclear spins. In a magnetic field $\mathbf{B} = B\hat{z}$ the individual spins are governed by the Hamiltonian $H = -\mu_z B = -\gamma I_z B$, where μ_z is the magnetic dipole operator, γ is the gyromagnetic ratio in units of $\text{rad}\times\text{Hz}/\text{T}$ and I_z is the spin operator. The magnetization along the magnetic field direction, $M = N \langle \mu_z \rangle$, is obtained from the single spin density matrix $\rho = \frac{1}{Z} e^{-H/k_B T}$, with $Z = \text{Tr}(e^{-H/k_B T})$, and the relation

$$M = N \text{Tr}(\mu_z \rho). \quad (2.8)$$

Using $\mu = \hbar\gamma I$, with I the spin quantum number and μ the single spin magnetic moment, we define the high temperature approximation $\mu B/k_B T \ll 1$ such that we can substitute $e^{-H/k_B T} \approx \mathbb{1} - H/k_B T$. Evaluating the traces using $\text{Tr}(I_z) = 0$ and $\text{Tr}(I_z^2) = \hbar^2 I(I+1)(2I+1)/3$ it

follows that

$$M = N\mu \frac{\mu B}{k_B T} \frac{I+1}{3I}. \quad (2.9)$$

which is Curie's formula. In a similar manner the variance can be calculated, since $\sigma_M^2 = N [\text{Tr}(\mu_z^2 \rho) - \text{Tr}(\mu_z \rho)^2]$. The result in the high temperature limit, and using $\text{Tr}(I_z^3) = 0$, is

$$\sigma_M^2 = N \left(\frac{\mu^2(I+1)}{3I} - \frac{M^2}{N^2} \right). \quad (2.10)$$

In particular we can now look at the spin polarization, $p = M/\mu N$, which is the fraction of magnetization, and its corresponding $\sigma_p = \sigma_M/\mu N$. In terms of the system parameters these read:

$$p = \frac{\mu B}{k_B T} \frac{I+1}{3I}, \quad (2.11a)$$

$$\sigma_p = \frac{1}{\sqrt{N}} \sqrt{\frac{I+1}{3I} - p^2}. \quad (2.11b)$$

By these definitions p varies on a scale from -1 to $+1$. These expressions for the polarization are valid around $p = 0$, which is appropriate for all cases in subsequent chapters where we shall never encounter nuclear spin polarizations larger than 0.1. What is of essence here is that when we take the limit $p \rightarrow 0$ we can approximate the distribution of nuclear spin polarization as a Gaussian with mean at $p = 0$ and a full width at half maximum (FWHM) equal to:

$$2\sqrt{2 \log 2} \sigma_p \Big|_{p=0} = 2\sqrt{2 \log 2} \sqrt{\frac{I+1}{3IN}}. \quad (2.12)$$

2.4.2 Hyperfine interaction

The hyperfine interaction in principle comprises a multitude of shifts and splittings that originate from the interaction of the electron with the nucleus' electric and magnetic moments. For the D^0 electrons in GaAs the relevant part is the coupling between the electron angular momentum and the nuclear spin. The magnetic moment of the nucleus produces a vector

potential $\mathbf{A} = (\mu_0/4\pi)(\boldsymbol{\mu} \times \mathbf{r})/r^3$ at a distance r . The interaction of the electron with this vector potential is captured by the Pauli Hamiltonian:

$$H_{Pauli} = \frac{1}{2m_e} (\boldsymbol{\sigma} \cdot (\mathbf{p} + e\mathbf{A}))^2 = \frac{p^2}{2m_e} + \frac{e}{m} \mathbf{A} \cdot \mathbf{p} + \frac{e\hbar}{2m} \boldsymbol{\sigma} \cdot (\nabla \times \mathbf{A}) + O(A^2), \quad (2.13)$$

where the last two terms describe the interaction (neglecting the part that is proportional to A^2). In order to be able to deal with the electron spin density distribution we rewrite these terms following [17]: The first term describes the coupling between nuclear spin and electron orbital angular momentum, it can be rewritten as $H_l = \frac{\mu_0\mu_B}{2\pi} \frac{\boldsymbol{\mu} \cdot \mathbf{l}}{r^3}$, where $\mu_B = e\hbar/2m_e$ is the Bohr magneton and $\mathbf{l} = (\mathbf{r} \times \mathbf{p})/\hbar$ is the dimensionless orbital angular momentum of the electron. The other term can be rewritten as:

$$H_s = \frac{\mu_0\mu_B\gamma\hbar}{2\pi} \left[\frac{3(\mathbf{I} \cdot \mathbf{r})(\mathbf{S} \cdot \mathbf{r})}{r^5} - \frac{\mathbf{I} \cdot \mathbf{S}}{r^3} + \frac{8\pi}{3} (\mathbf{I} \cdot \mathbf{S})\delta(\mathbf{r}) \right], \quad (2.14)$$

where we introduced the dimensionless spin vectors $\mathbf{I} = \boldsymbol{\mu}/\hbar\gamma$ and $\mathbf{S} = \boldsymbol{\sigma}/2$, whose elements are operators such that e.g. $S_z |S, m_s\rangle = m_s |S, m_s\rangle$. Both H_s and H_l have dimensions of energy per cubic metre. To obtain the energy of the system we need to evaluate $\langle \psi_e | H_l + H_s | \psi_e \rangle$, i.e. to multiply with the electron density and integrate over space. Now H_s is put in a convenient form where the first two terms describe magnetic dipole-dipole interaction (giving H_{dd}) and the last term is known as the Fermi contact interaction (giving H_{fc}). So, if we accordingly write $H_s = H_{dd} + H_{fc}$ it holds that for p-electrons (the zero orbital amplitude at the origin gives a contribution zero for H_{fc}) $\langle \psi_e | H_l + H_s | \psi_e \rangle = \langle \psi_e | H_l + H_{dd} | \psi_e \rangle$. For s-electrons (spherically symmetric, finite at origin, but the orbital integration leads to zero contributions for H_l and H_{dd}) $\langle \psi_e | H_l + H_s | \psi_e \rangle = \langle \psi_e | H_{fc} | \psi_e \rangle$, for which the integration leads to $H = \frac{4}{3}\mu_0\mu_B\gamma\hbar \mathbf{I} \cdot \mathbf{S} |\psi_e(0)|^2$, where the zero position refers to the location of one particular nucleus. This expression is appropriate for D^0 electrons because they have an s-like wave function. We have to take into account all nuclei by summing their contributions:

$$H = \frac{4}{3}\mu_0\mu_B\hbar \sum_n \gamma_n \mathbf{I}_n \cdot \mathbf{S} |\psi_e(\mathbf{r}_n)|^2. \quad (2.15)$$

To be able to carry out the summation we firstly have to take into account that there are different nuclei in the crystal: The primitive cell contains one ^{75}As atom and one Ga atom of which 60% are ^{69}Ga and 40% are ^{71}Ga . The gyromagnetic ratios of these isotopes are $\gamma/(2\pi) = 7.3, 10.3$ and 13 MHz T^{-1} respectively. Secondly, the electronic density is slightly different on cation and anion sites: In reference [18] this effect, while not directly measured in GaAs, was estimated from the measured atomic hyperfine interaction and measurements of electron density in InSb. Using these numerical values it is insightful to write equation 2.15 first as a Zeeman-type magnetic field seen from the point of view of a nucleus:

$$H = -\gamma\hbar\mathbf{I}_n\mathbf{B}_e^n, \quad (2.16a)$$

$$\mathbf{B}_e^n = -\frac{4}{3}\mu_0\mu_B\alpha_n\mathbf{S}|F(\mathbf{r}_n)|^2. \quad (2.16b)$$

where $\alpha_n = 4434.38$ for As and 2624.4 (dimensionless constants) for Ga nuclei represents the difference between cation and anion sites [18]. The expectation value $\langle\mathbf{B}_e^n\rangle$ is the Knight field [19] and it follows that the maximum Knight field, when $\langle S\rangle = 1/2$, is 11.3 mT for As and 6.7 mT for GaAs.

Similarly, we can write equation 2.15 from the point of view of the electron (below here $c_{69\text{Ga}}$, $\gamma_{69\text{Ga}}$, and $u_{69\text{Ga}}$ denote the relative isotopic abundance, the nuclear gyromagnetic ratio, and the Bloch wave function at the site of the ^{69}Ga isotope, respectively, and similar for the other isotopes):

$$H = -\boldsymbol{\mu}_e\mathbf{B}_n = -g\mu_B\mathbf{S}\mathbf{B}_n, \quad (2.17a)$$

$$\mathbf{B}_n = -\frac{4}{3g}\mu_0\hbar\sum_n\gamma_n\mathbf{I}_n|\psi_e(\mathbf{r}_n)|^2, \quad (2.17b)$$

$$\mathbf{B}_n = -\frac{4}{3g}\mu_0\hbar \sum_n \gamma_n \mathbf{I}_n |u_0(\mathbf{r}_n)|^2 |F(\mathbf{r}_n)|^2, \quad (2.18a)$$

$$\begin{aligned} \mathbf{B}_n = & -\frac{4}{3g}\mu_0\hbar \times \\ & \left(c_{69Ga} \gamma_{69Ga} |u_{69Ga}|^2 + c_{71Ga} \gamma_{71Ga} |u_{71Ga}|^2 + c_{75As} \gamma_{75As} |u_{75As}|^2 \right) \times \\ & \sum_n \mathbf{I}_n |F(\mathbf{r}_n)|^2, \end{aligned} \quad (2.18b)$$

$$\mathbf{B}_n = -\frac{4}{3g}\mu_0\hbar \sum_i c_i \gamma_i |u_i|^2 \sum_n \mathbf{I}_n |F(\mathbf{r}_n)|^2. \quad (2.18c)$$

The effective magnetic field $\langle B_n \rangle$ is called the Overhauser field [20]. If the nuclear spin polarization is uniform we can calculate the contribution for the different isotopes. Taking $g = -0.42$ we calculate $\langle B_n^{As} \rangle = -1.89 \langle \mathbf{I} \rangle$, $\langle B_n^{69Ga} \rangle = -0.948 \mathbf{I}$ and $\langle B_n^{71Ga} \rangle = -0.797 \mathbf{I}$ which gives a total field of $3.64 \langle I \rangle$, in units of Tesla. Hence the fully polarized nuclear spins will apply an Overhauser field to the electron of 5.46 T.

Given the high nuclear spin temperature we expect the equilibrium Overhauser field to be zero. But the fluctuations in the nuclear spin polarization result in a fluctuating Overhauser field. This has as a consequence that the electron spins in an ensemble precess at slightly different frequencies. Following section 2.4.1 we assume these frequency differences to be Gaussian distributed. The effect of this is that information about the spins' phase is lost, this is captured by:

$$C(t) = \int_{-\infty}^{+\infty} \frac{1}{\sqrt{2\pi}\sigma_p} e^{-(p/\sqrt{2}\sigma_p)^2} \cos\left(\frac{g\mu_B B_{max} p}{\hbar} t\right) dp = e^{-\left(\frac{g\mu_B B_{max}\sigma_p}{\sqrt{2}\hbar}\right)^2 t^2}, \quad (2.19)$$

where the dephasing time

$$T_2^* = \left| \frac{\sqrt{2}\hbar}{g\mu_B B_{max}\sigma_p} \right| \quad (2.20)$$

with σ_p as in 2.11b.

2.4.3 Dynamical nuclear spin polarization

It is possible to force the state of the nuclear spin bath to deviate from its thermal equilibrium configuration described in Section 2.4.1. This process changes the distribution of the nuclear spins to another distribution, $P(\delta)$, that replaces the aforementioned Gaussian distribution. The dephasing process of the electron spin is then described by an integral similar to Eq. 2.19, where the Gaussian distribution is replaced by $P(\delta)$. For the integration over an arbitrary distribution one can resort to numerical methods and the dephasing time remains defined as the time at which $C(t) = 1/e$. In general, when $P(\delta)$ has a narrower width than the thermal, Gaussian distribution this results in reduced dephasing of the electron spin.

To influence the nuclear spin states directly one can resort to driving the nuclear spin transition directly by nuclear magnetic resonance at microwave frequency. This has a depolarizing effect and hence cannot change the nuclear spin polarization much if it was initially unpolarized. Another method relies on a combination of the optical orientation of the electron spin, hyperfine contact interaction between this electron and the nuclei, and the relaxation processes of the electron spin. In this scheme there is no external field applied at the frequency of nuclear spin transitions. The physical nature of this method known as dynamic nuclear spin polarization (DNP) is that, due to rapid electron spin relaxation, the Knight field that the nuclear spin feels from the electron becomes a random function of time. When the noise spectrum of this randomly fluctuating field possesses a frequency component that matches the frequency of nuclear spin splitting it is able to induce transitions between the nuclear spin states (which are often called *flips* in this context). DNP originates from the hyperfine interaction Hamiltonian in Eq. 2.15. When treated as a perturbation of which the electron's spin part is fluctuating in time (i.e. $\mathbf{S}(t)$) this leads to a master equation that governs the nuclear spin polarization. This calculation is extensively outlined in Ref. [21, Chapter 5] resulting in the equation of motion for the spin polarization of a single nucleus, $\langle I_z \rangle$:

$$\langle \dot{I}_z \rangle = -\Gamma_h \left(\langle I_z \rangle - \langle \bar{I}_z \rangle - \frac{I^2 + I}{S^2 + S} [\langle S_z \rangle - \langle \bar{S}_z \rangle] \right). \quad (2.21)$$

Here Γ_h is the rate of spin flips and the overbars denote the thermal equilibrium value of the spins' expectation values. The underlying dynamics is probabilistic and both directions of nuclear spin flips, increasing as well as decreasing the nuclear spin quantum number, do occur. In fact on a microscopic level the transition involves simultaneous flips of the electron and nuclear spin, conserving overall angular momentum. The equation 2.21 shows how the nett rate of change of the nuclear spin polarization is dependent on the electron spin polarization's deviation from thermal equilibrium. The power of the DNP mechanism lies in the fact that using optical orientation techniques ($\langle S_z \rangle - \langle \bar{S}_z \rangle$) can easily be driven to larger values, while ($\langle I_z \rangle - \langle \bar{I}_z \rangle$) remains (at least in the system studied in this thesis) close to zero. The electron spin polarization can thus determine the direction of nuclear spin polarization, which can be driven to positive as well as negative values. For Equation 2.21 to hold it is required that (1) An external magnetic field is applied, along some direction here denoted by z ; and (2) The dynamics of the electron spin is faster than that of the nuclear spins, in particular the random fluctuations of the Knight field should be fast compared to the frequency of nuclear spin splitting by the Knight field.

2.4.4 Nuclear spin diffusion

The equation 2.21 contains a depolarizing term ($\langle I_z \rangle - \langle \bar{I}_z \rangle$) (which is opposite in sign to the term containing the electron spin polarization) that represents the tendency of the nuclear spins to relax towards their thermal equilibrium state. Another depolarizing mechanism is spin diffusion, as depicted in Figure 2.4. It represents the flow of nuclear spin polarization away from the localized electron spin. Strictly speaking this only mimics the effect of a depolarizing mechanism because it does not involve decay of the nuclear spin polarization in the crystal. The built up nuclear polarization that spreads to remote regions does not influence the electron spin anymore and is therefore effectively lost. Nuclear spin diffusion around the donors in GaAs has been studied in the work of Paget [22]. The microscopic mechanism is the dipolar coupling between nuclear spins which allows for two nuclear spins at different locations to flip their spin

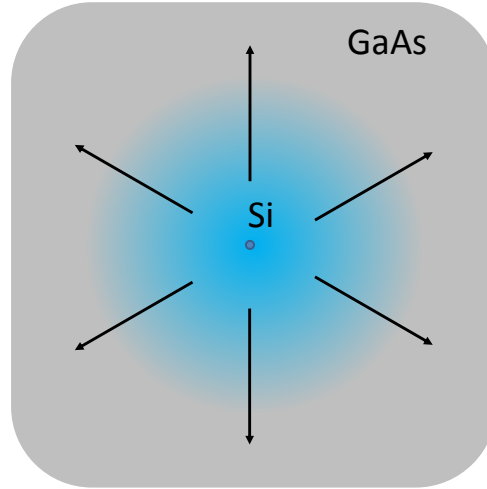


Figure 2.4: Polarized nuclear spins around the donor (blue region is the extent of the D^0X wave function) will diffuse to the bulk (gray region) resulting in a perceived decay of nuclear spin polarization for the donor electron. Spin diffusion is mediated by dipole-dipole interaction between nuclear spins of the same species (because their Zeeman energy matches). Additionally, when the electron spin is partially polarized diffusion will be suppressed because there is a radial gradient in the Knight shift perceived by the nuclei around the donor. The resulting mismatch in level splittings reduces the probability of spin flips among the nuclei.

in opposite direction. Because of the narrow line widths of nuclear spin transitions this mechanism is suppressed among nuclei with different gyromagnetic number (in the presence of an external magnetic field). Another factor that suppresses the spin diffusion mechanism is the presence of an inhomogeneous magnetic field: Close to the donor impurities the Knight field is spatially inhomogeneous, causing nuclei to have different energy level splittings dependent on their position. Hence when the electron spin is (partially) polarized the nuclear spin diffusion away from the donor site is suppressed.

2.5 Measurement of EIT[†]

To conclude this chapter we demonstrate that it is possible to measure EIT using the bound states of the D^0 - D^0X system in GaAs. This measurement is performed on a Λ -system formed by a D^0X level and the two D^0 electron spin states, where the lower energy transition is labeled A and the higher energy transition A^* (to keep the labeling consistent with earlier work on this system [9, 23]). The measurements reported here were realized at 4.2 K and in an applied magnetic fields in the range 6 to 8 T. The observation of EIT is shown in Fig. 2.5. For these results we fixed the control laser central on the A transition (with linear V polarization, defined as parallel to the externally applied magnetic field), while the probe laser is scanned across the A^* transition (H polarization, orthogonal to the externally applied magnetic field). When the control and probe field meet the condition for two-photon Raman resonance (the difference in photon energy exactly matches the D^0 spin splitting), a narrow peak with enhanced transmission appears inside the broader A^* absorption dip, which is the fingerprint of EIT. In Fig. 2.5(a) this occurs inside an A^* absorption with optical density 1.0, while for the sample with $n_{Si} = 3 \times 10^{13} \text{ cm}^{-3}$ this is 0.3 (Fig. 2.5(b)). We further focus on this latter sample since higher resolution of the EIT spectra makes it more suited for our further studies.

The lines in Fig. 2.5 and 2.6 are results of fitting EIT spectra with the established theory [15]. This involves calculating the steady-state solution of a density-matrix equation for the three-level system, and accounts for coherent driving by the lasers and relaxation and dephasing rates between the levels. The free parameters are the inhomogeneous broadening γ_{A^*} (typically 6 GHz) for the optical transition A^* , the spin dephasing time T_2^* and the control-field induced Rabi frequency Ω_c (and $\Omega_p \ll \Omega_c$). The rest of the parameters are the same as in Ref. [23], and we found Ω_c always consistent with an independent estimate from the optical intensity and electric dipole moment. We obtain good fits and the main features in our results are consistent with EIT, as we discuss next.

Figure 2.5(b) shows EIT spectra taken at different intensities I_c of the

[†] This section is based on reference 1 on page 151.

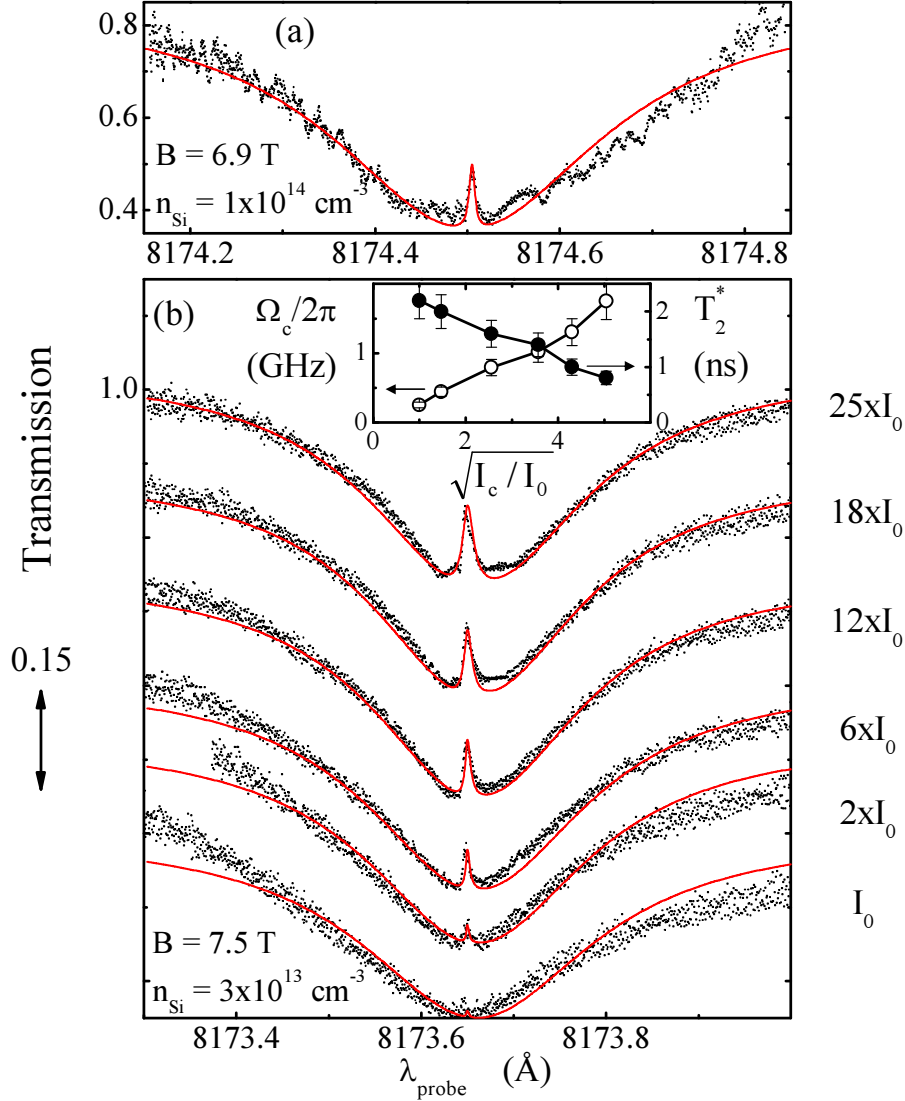


Figure 2.5: (a) EIT spectrum from sample with Si doping at $1 \times 10^{14} \text{ cm}^{-3}$. Dots - experiment. Line - numerical fit. (b) EIT spectra from sample with Si doping at $3 \times 10^{13} \text{ cm}^{-3}$, for probe-field intensity 0.04 W cm^{-2} and a range of control-field intensities I_c with $I_0 = 0.4 \text{ W cm}^{-2}$. The inset shows the fitting results for Rabi frequency Ω_c and spin dephasing time T_2^* .

control field, where a stronger control field yields a higher and broader EIT peak. As expected for EIT, we observe that Ω_c from fits scales linearly with $\sqrt{I_c}$ (Fig. 2.5(b), inset). The Ω_c values reach an angular frequency of $2\pi \times 2$ GHz, and we could only obtain clear EIT spectra with such high Ω_c in samples with complete adhesion onto the sapphire substrate. Our results from samples with incomplete adhesion (and work with epi-layers that are not removed from the original GaAs substrate [23, 24, 4]) suffer from heating, which is observed as a broadening of the free exciton line into the region of the D⁰X resonances.

Figure 2.6 shows how the EIT peak position depends on detuning of the control field from the *A* transition. As expected, the EIT peak follows the detuning of the control field. However, the EIT peak in the blue-detuned traces is clearly more prominent than in the red-detuned cases. We attribute this to a change in the effective Rabi frequency Ω_c that results from the weak Fabry-Perot interference within the GaAs film, and we can indeed fit the results with fixed $T_2^* = 2$ ns and varying Ω_c (Fig. 2.6, inset). We can exclude that the difference in the quality of EIT spectra is coming from optical coupling to a level outside our Λ -system, since all other transitions are well separated spectrally and in polarization dependence (see Chapter 7 for a study of the spectral position of these other levels).

References

- [1] Khaetskii, A. V. & Nazarov, Y. V. Spin relaxation in semiconductor quantum dots. *Phys. Rev. B* **61**, 12639–12642 (2000).
- [2] Khaetskii, A. V. & Nazarov, Y. V. Spin-flip transitions between zeeman sublevels in semiconductor quantum dots. *Phys. Rev. B* **64**, 125316 (2001).
- [3] Fu, K.-M. C. *et al.* Millisecond spin-flip times of donor-bound electrons in GaAs. *Phys. Rev. B* **74**, 121304 (2006).
- [4] Clark, S. M. *et al.* Ultrafast optical spin echo for electron spins in semiconductors. *Phys. Rev. Lett.* **102**, 247601 (2009).
- [5] Lampert, M. A. Mobile and immobile effective-mass-particle complexes in non-metallic solids. *Phys. Rev. Lett.* **1**, 450–453 (1958).
- [6] Rashba, E. & Gergenishvili, G. Edge absorption theory in semiconductors. *Sov. Phys. Solid. State* **4**, 759 (1972).

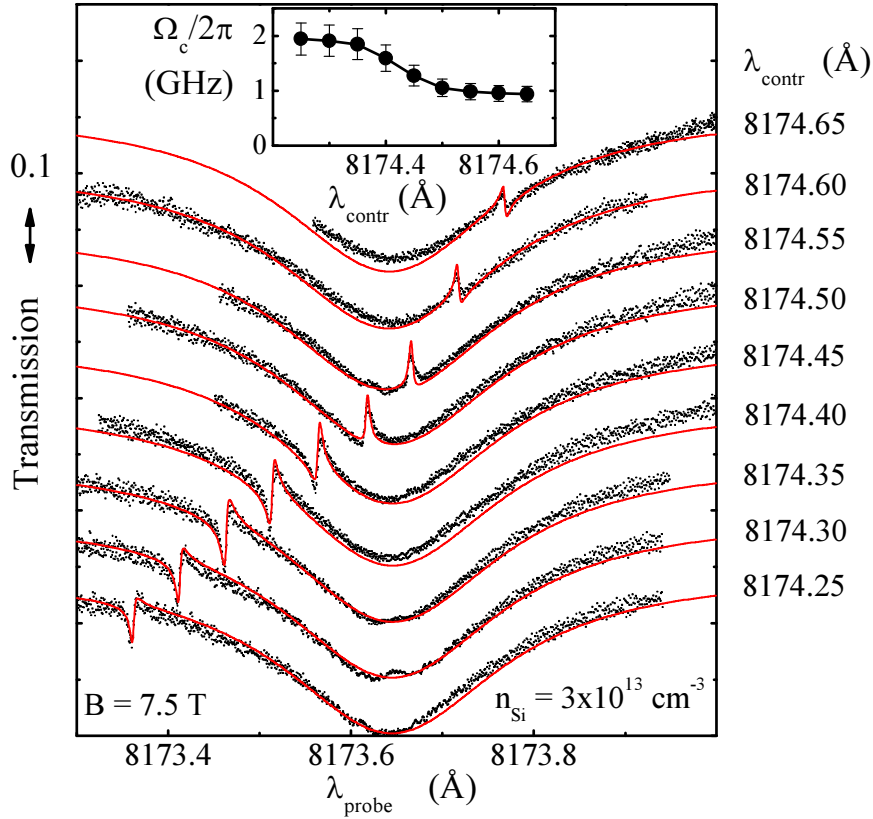


Figure 2.6: Dependence of EIT spectra on control-field detuning. The position of the EIT peak follows precisely the control-field detuning from transition A. Dots - experiment with control (probe) intensity 6 (0.04) W cm^{-2} . Lines - fits with $T_2^* = 2 \text{ ns}$ and Ω_c as presented in the inset.

- [7] Hwang, C. & Dawson, L. Lifetime of excitons bound to neutral donors in high-purity GaAs. *Solid State Communications* **10**, 443 – 446 (1972).
- [8] Herbert, D. C. Electron correlation and bound excitons in semiconductors. *Journal of Physics C: Solid State Physics* **10**, 3327 (1977).
- [9] Karasyuk, V. A. *et al.* Fourier-transform magnetophotoluminescence spectroscopy of donor-bound excitons in GaAs. *Phys. Rev. B* **49**, 16381–16397 (1994).
- [10] Meier, F. & Zakharchenia, B. *Optical orientation*. Modern problems in condensed matter sciences (North-Holland, 1984).
- [11] Shore, B. *The Theory of Coherent Atomic Excitation, Multilevel Atoms and Incoherence* (Wiley, 1990).
- [12] Bremer, R. *Optical control of donor-bound electron and nuclear spins in n-doped*

- semiconductors*. Master's thesis, University of Groningen (2012).
- [13] Sladkov, M. *et al.* Electromagnetically induced transparency with an ensemble of donor-bound electron spins in a semiconductor. *Phys. Rev. B* **82**, 121308 (2010).
 - [14] Yale, C. G. *et al.* All-optical control of a solid-state spin using coherent dark states. *Proceedings of the National Academy of Sciences* **110**, 7595–7600 (2013).
 - [15] Fleischhauer, M., Imamoglu, A. & Marangos, J. P. Electromagnetically induced transparency: Optics in coherent media. *Rev. Mod. Phys.* **77**, 633–673 (2005).
 - [16] Chen, W. *et al.* All-optical switch and transistor gated by one stored photon. *Science* **341**, 768–770 (2013).
 - [17] Abragam, A. *The Principles of Nuclear Magnetism*, p. 171. The International Series of Monographs on Physics (Oxford University Press, Amen House, London E.C.4, 1961), first edn.
 - [18] Paget, D., Lampel, G., Sapoval, B. & Safarov, V. I. Low field electron-nuclear spin coupling in gallium arsenide under optical pumping conditions. *Phys. Rev. B* **15**, 5780–5796 (1977).
 - [19] Townes, C. H., Herring, C. & Knight, W. D. The effect of electronic paramagnetism on nuclear magnetic resonance frequencies in metals. *Phys. Rev.* **77**, 852–853 (1950).
 - [20] Overhauser, A. W. Polarization of nuclei in metals. *Phys. Rev.* **92**, 411–415 (1953).
 - [21] Abragam, A. *The Principles of Nuclear Magnetism*. The International Series of Monographs on Physics (Oxford University Press, Amen House, London E.C.4, 1961), first edn.
 - [22] Paget, D. Optical detection of nmr in high-purity gaas: Direct study of the relaxation of nuclei close to shallow donors. *Phys. Rev. B* **25**, 4444–4451 (1982).
 - [23] Fu, K.-M., Santori, C., Stanley, C., Holland, M. & Yamamoto, Y. Coherent population trapping of electron spins in a high-purity *n*-type GaAs semiconductor. *Phys. Rev. Lett.* **95**, 187405 (2005).
 - [24] Fu, K.-M. C. *et al.* Ultrafast control of donor-bound electron spins with single detuned optical pulses. *Nature Physics* **4**, 780–784 (2008).

Chapter 3

Measurements of the local nuclear spin distribution by electromagnetically induced transparency

Abstract

We demonstrate how nuclear spin polarization can be induced and detected by optical interaction with donor-bound electrons in GaAs. Resonant addressing of a Λ -system formed by the Zeeman-split bound-electron spin states and a donor-bound exciton state results in nuclear spin polarization either along or opposite to an external magnetic field. The coherent population trapping effect in the Λ -system is used to detect spin polarization of nuclei at the donor location. We present how this technique is used as a tool to monitor the local build-up and relaxation of nuclear spin polarization.

3.1 How the EIT lineshape reflects the nuclear spin state

The lineshape of the EIT resonance contains information on the spin polarization of the nuclei near the donors. In two-laser spectroscopy the measured transmission of each of the lasers through the GaAs sample is determined by the amplitude transfer function $T(\omega_i, \Omega_i | \omega_j, \Omega_j) = \exp(i\omega_i nd/c\chi(\omega_i, \Omega_i | \omega_j, \Omega_j)/2)$, where d is the thickness of the medium, n is the refractive index of GaAs and c is the speed of light, $i, j \in 1, 2$ with $i \neq j$ labels the laser frequencies ω and powers expressed as Rabi frequency Ω , as also introduced in Fig. 3.1. The notation of separating the variables in T and χ by a vertical line is meant to indicate that we consider the transfer function with variables ω_i, Ω_i conditional on ω_j, Ω_j which then assume the role of parameters. The susceptibility χ is obtained by considering the polarization density of a medium filled with donors with concentration ρ , each represented as a Λ -system as described in Chapter 2. The dependence of the transmittance on the decay and dephasing parameters of the Λ -system is implicit. The susceptibility is made up from the polarizabilities of individual systems β which can, and generally will, show small differences, thus forming an inhomogeneous ensemble. We focus on the inhomogeneity arising from the nuclear spin polarization. This inhomogeneity gives rise to a distribution of Overhauser shifts $P(\delta)$ and we express the susceptibility for the medium accordingly as

$$\chi(\omega_i, \Omega_i | \omega_j, \Omega_j) = \rho \int P(\delta) \beta(\omega_i, \Omega_i | \omega_j, \Omega_j, \delta) d\delta. \quad (3.1)$$

The polarizability β exhibits an EIT resonance (β decreases as the transmission increases). When this resonance is narrow as compared to $P(\delta)$ (such that it can be approximated by a Dirac delta function), Eq. 3.1 implies that the transmission near EIT resonance takes the shape of $P(\delta)$. We now show that in this GaAs system the EIT lineshape indeed changes as we induce a nuclear spin polarization by optical pumping. For this experiment we use the setup as described in Sec. 8.2 where two laser beams co-propagate through the sample and are collected immediately behind the sample on a photodiode. One of the laser beams is modulated by a chopper at 6 kHz and we isolate the modulated part of the total transmission signal by lock-in detection (for details see Sec. 8.4).

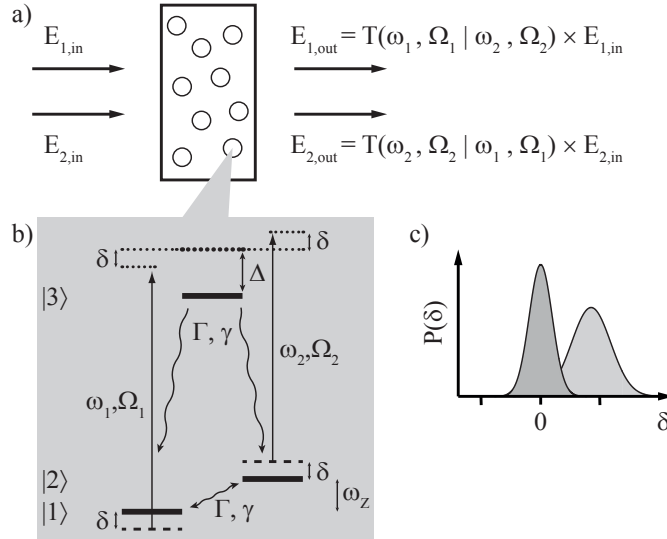


Figure 3.1: Transmission through a medium containing inhomogeneous Λ -systems. (a) The transmission of each of the two laser fields is determined by an amplitude transfer function, T , which is conditional on the intensity and frequency of the other laser when the lasers are both close to resonance with the transitions of a Λ -system. T follows from the susceptibility, which is an effective description of the medium and is in turn derived from the polarizabilities of the individual Λ -systems. One of these is depicted in (b) (see also Fig. 4.1a). Nonzero nuclear spin polarization causes a (antisymmetric) contribution to laser detuning, δ . The parameter Δ is the single-laser detuning with respect to exact resonance for the case $\delta = 0$ (we use positive Δ for the blue-detuned case). (c) The inhomogeneity in nuclear spin polarization is introduced through having δ governed by a probability distribution $P(\delta)$. Dynamic nuclear polarization can change the position and shape of the initial $P(\delta)$ (dark gray), such that the mean shifts away from zero (e.g. light gray area).

3.2 Detection of optically induced dynamic nuclear polarization

Dynamic nuclear polarization (DNP) resulting from optical pumping is detected by comparing the initial EIT lineshape, with the nuclear spins at thermal equilibrium, to the EIT lineshape after pumping. Figure 3.2a shows the initial EIT resonance measured in the transmission signal of a $10\ \mu\text{m}$ thick film of n-GaAs. The EIT lineshape contains information of

the underlying nuclear spin distribution (Eq. 3.1), so any modification of the nuclear spin state by optically induced dynamic nuclear polarization (DNP, as explained in Section 2.4.3) will be reflected in the EIT resonance. When the same scan is taken again after 30 minutes of optical pumping, with a single pump laser resonant on the A^* transition (defined in Fig. 3.2a), the EIT resonance has shifted and broadened. This is visible in Panel b where the two EIT scans are compared. Since the EIT shift relates to the underlying nuclear spin distribution as described in the previous section, we can associate the shift with a change in the average of the distribution $P(\delta)$ and hence a net buildup of nuclear spin polarization. The shift of $4\ \mu\text{eV}$ depicted in the figure corresponds to an average Overhauser field of approximately 0.2 T. The broadening indicates an increased inhomogeneity of the Overhauser field. As we discuss in the next section, there is a dependence of the Overhauser shift on pump laser intensity. Due to the experimental setup we cannot address the ensemble within the laser spot with equal intensity. The first reason for this is that the spot is Gaussian and therefore the pump laser intensity for individual donors decreases with increasing radial distance from the spot center. Another factor is that because of reflections at the GaAs film surface a standing wave intensity distribution forms inside the sample. The former effect could be mitigated by shaping the profile of the pump beam and the latter could be improved by applying anti-reflection coating on the GaAs film.

3.3 Timescale of optically induced DNP buildup

In Fig. Fig:toolFig1b we observe the EIT lineshape after a duration of pumping sufficiently long for the DNP process to saturate, i.e. when a balance is established between the polarizing effect of the pump laser and the depolarizing effect of spin diffusion. However it is also possible to monitor the evolution of the system during optical pumping to get insight into the timescale at which the DNP process takes place. This is shown in Fig. 3.3. Panel a shows repeated EIT scans which were taken while the pump laser was on. The stronger laser that is fixed on resonance with the A^* transition fulfills the function of optical pumping during most of the

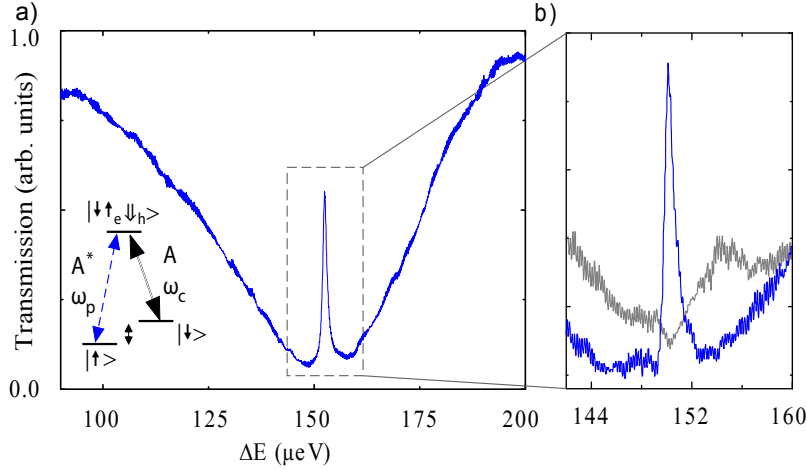


Figure 3.2: (a) Electromagnetically induced transparency (EIT) from an ensemble of donor-bound electrons in n-GaAs. The ensemble is addressed in a Λ -configuration (see inset), formed by the Zeeman-split spin states of the electron and the lowest level of the donor-bound exciton complex. A control laser is fixed at the A-transition while a probe laser scans across the A*-transition, with photon-energy difference ΔE between the lasers. (b) Zoom-in of the spectrum in (a) showing the EIT peak before (blue) and after (gray) 30 minutes of optical pumping on the A*-transition. The EIT peak in the gray trace (arrow) shows a shift and broadening.

time of the experiment, but simultaneously functions as a control for the EIT scans when the weak probe laser is scanned over the A-transition. Panel b) shows the time evolution of the average of the EIT resonance as extracted from the scans in Panel a). The solid line through the datapoints is an exponential fit to the data which reveals a time constant for DNP build up of 340 seconds.

3.4 Bidirectionality of DNP in the Λ -system

The Λ -system allows for optical orientation of the electron spin along or against the magnetic field. We verify in Fig. 3.4 that polarization of the electron spin by pumping on the A transition reverses the direction of the EIT shift. This is done by first pumping for 30 minutes on either the

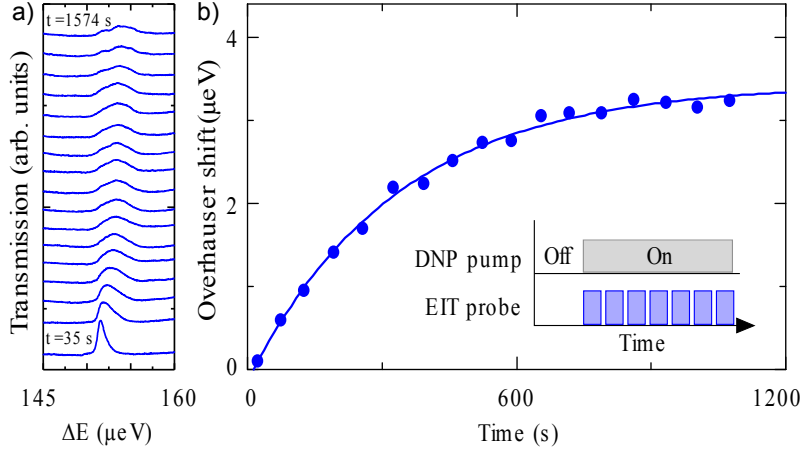


Figure 3.3: (a) Build up of nuclear spin polarization measured by taking EIT scans repeatedly, using the strong pump laser (6 W cm^{-2} on A^*) as the control. A weak probe laser (0.1 W cm^{-2}) periodically scans the A -transition (see time labels). Time $t = 0$ is the moment where the pump laser is switched on after keeping the sample in the dark for an hour (see inset of (b)). (b) The Overhauser shift as fitted from the data in (a) as a function of time (dots). The solid line is a fit for exponential build-up, with a time constant $\tau_{\text{build}} \approx 340$ s.

A^* - or A -transition, the resulting datasets are color-coded blue and red respectively. The shift of the EIT resonance immediately after pumping indicates the presence of a non-zero Overhauser field, which is opposite in sign for the blue and red cases. To confirm this observation we continue taking EIT scans to observe relaxation of the center of EIT resonance towards its initial value. In this manner it also becomes apparent on which timescale the nuclear spin polarization decays: The solid lines are exponential fits yielding decay times, τ_d of 600 s after pumping on the A transition, and 480 s after pumping on the A^* transition.

The presence of bidirectionality also excludes that the EIT shift is due to heating of the sample during the optical pumping, which would give a shift in only one direction.

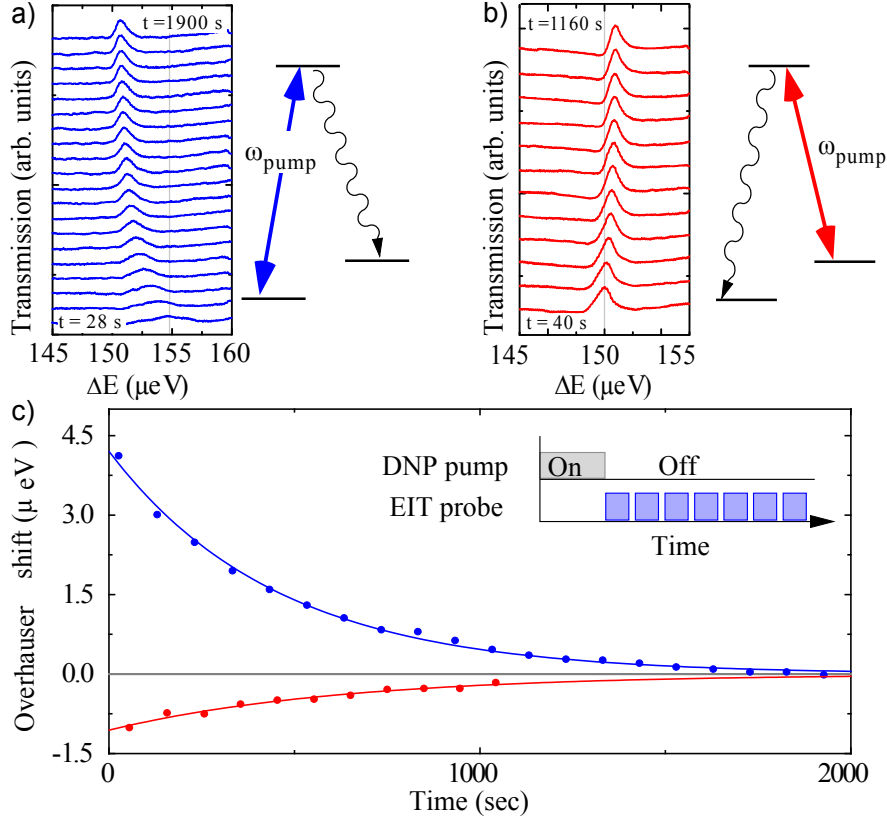


Figure 3.4: Bi-directionality and relaxation of the induced Overhauser shift. (a) A sequence of scans taken after 30 minutes of optical pumping on A^* with intensity of 6 W cm^{-2} showing the evolution of the EIT resonance over time during the relaxation of prepared DNP. EIT scans are taken with control (2.37 W cm^{-2}) on the A -transition and scanning probe (0.109 W cm^{-2}) on the A^* -transition (see inset of (c)). (b) Same sequence of EIT scans after optical pumping on A . (c) The Overhauser shift as derived from the data in (a) and (b) as a function of time (dots). The solid lines are fits for exponential decay, with time constants τ_d of 600 s (after pumping on the A -transition) and 480 s (after pumping on the A^* -transition).

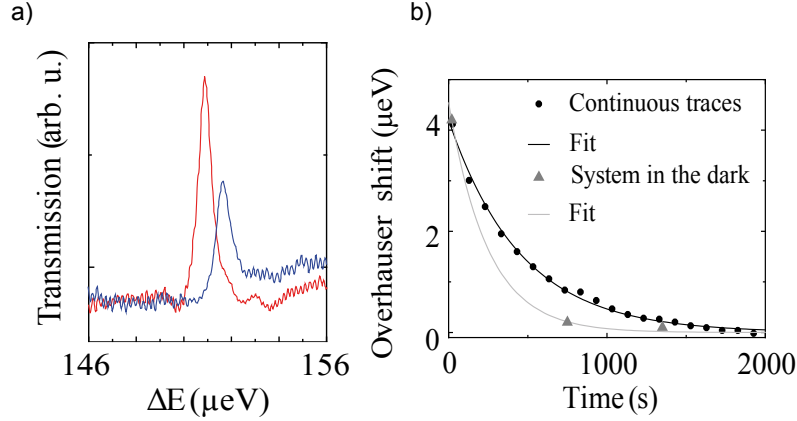


Figure 3.5: The invasive character of EIT measurement on DNP. (a) The difference in EIT peak position for the control laser on the A- (red) and A*-transition (blue), taken with similar intensities for the control laser (2 W cm^{-2}) in the two cases, and weaker probe lasers (see main text). (b) Relaxation of the nuclear spin polarization. Datapoints show fitted EIT peak positions for different times after optical pumping on A* (6 W cm^{-2}). Gray triangles: fitted EIT peak positions from scans taken after a dark time following 30 minutes of optical pumping on A* with intensity of 6 W cm^{-2} (pumping was repeated for each datapoint). Black dots: fitted EIT peak positions of a sequence of scans taken after 30 minutes of optical pumping on A*. Corresponding lines are exponential fits.

3.5 Invasiveness of the detection method

The optical pumping is closely related to the EIT probing. Therefore we investigate how EIT measurements influence the DNP process. This is shown in Fig. 3.5. The difference between taking EIT with control on the A or A* transition is shown in Panel a. There is a minor shift of $1 \mu\text{eV}$. Panel b shows how EIT measurement influences the relaxation of the nuclear spins. When the system is kept in the dark the spins relax faster. We attribute this to the inhomogeneous Knight shift which protects against spin diffusion when the electron spin is (partially) polarized.

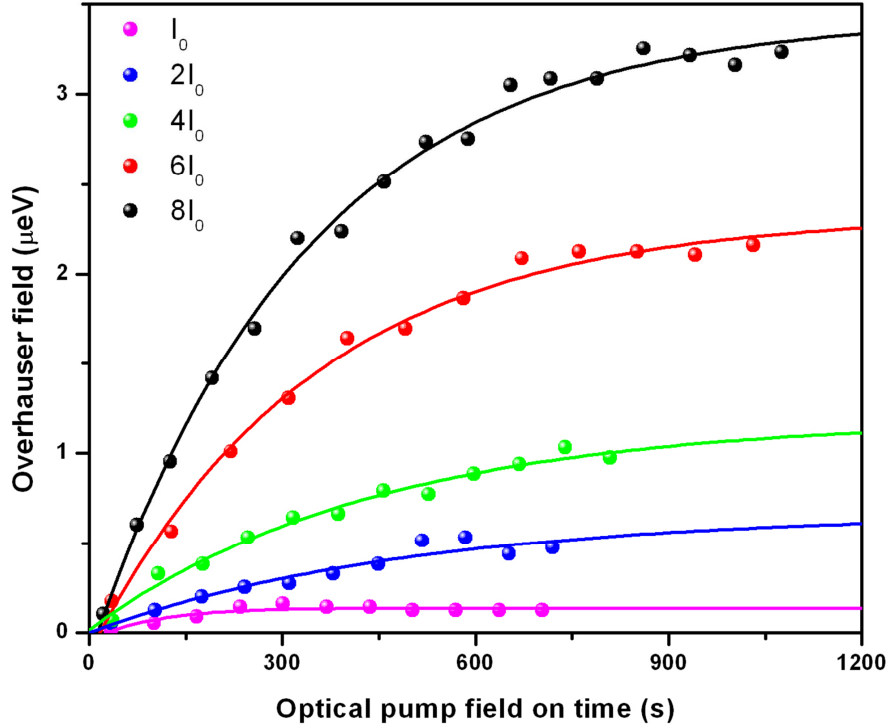


Figure 3.6: Intensity dependence of DNP. All data sets were acquired in the same way as for Fig. 3.3b. The intensity is increased in steps from $I_0 = 1 \text{ W cm}^{-2}$ to $8I_0$.

3.6 Dependence on pump laser intensity

The dependence on pump laser intensity is presented in Fig. 3.6, with a series of measurements performed in the same way as was done for Fig. 3.3b. The intensity of the pump laser is from $I_0 = 1 \text{ W cm}^{-2}$ to $8I_0$. For intensities over $8I_0$ it was not possible to obtain these measurements because of increased noise levels in the detection setup and a stronger broadening of the shifted EIT peak. However, the fact that the steady state Overhauser field increases roughly linear with pump laser intensity (rather than quickly saturating), as shown in Fig. 3.6, needs additional explanation. The long D^0 spin relaxation times suggest that the pump laser completely polarizes the electron spin, already for pump intensities far below $8I_0$. It has been shown that for pump laser intensities as low as

10 mW cm⁻² the electron spin polarization is already well over 50% [1].

This discrepancy can be explained by unintended pumping, such as shown in Fig. 3.7, which causes the dependence of the maximum Overhauser shift on the optical pump intensity to increase up to high intensities. The mechanism behind this is as follows: when the pump laser is tuned to resonance with the transition $|\uparrow\rangle\text{-}|A\rangle$ there may be unintended coupling to the $|\downarrow\rangle\text{-}|B\rangle$. This has as effect that the optical excitation rate (and with it the electron spin flip rate) increases linearly up to high intensities. Without the unintended pumping this rate is limited by $1/T_2$ because the electron has spin has to decay before the next optical cycle can be initiated; with the unintended coupling the system is optically excited from both ground states, this increases the fluctuation rate of the electron spin. In the calculation for the plot we used $T_2 = 10\ \mu\text{s}$, corresponding to a maximum optical excitation rate of 0.1 MHz. The excitation rate is seen to extend beyond $1/T_2$ and the hyperfine flip rate Γ_h will increase with it as described in Sec. 2.4.3.

References

- [1] Clark, S. M. *et al.* Ultrafast optical spin echo for electron spins in semiconductors. *Phys. Rev. Lett.* **102**, 247601 (2009).

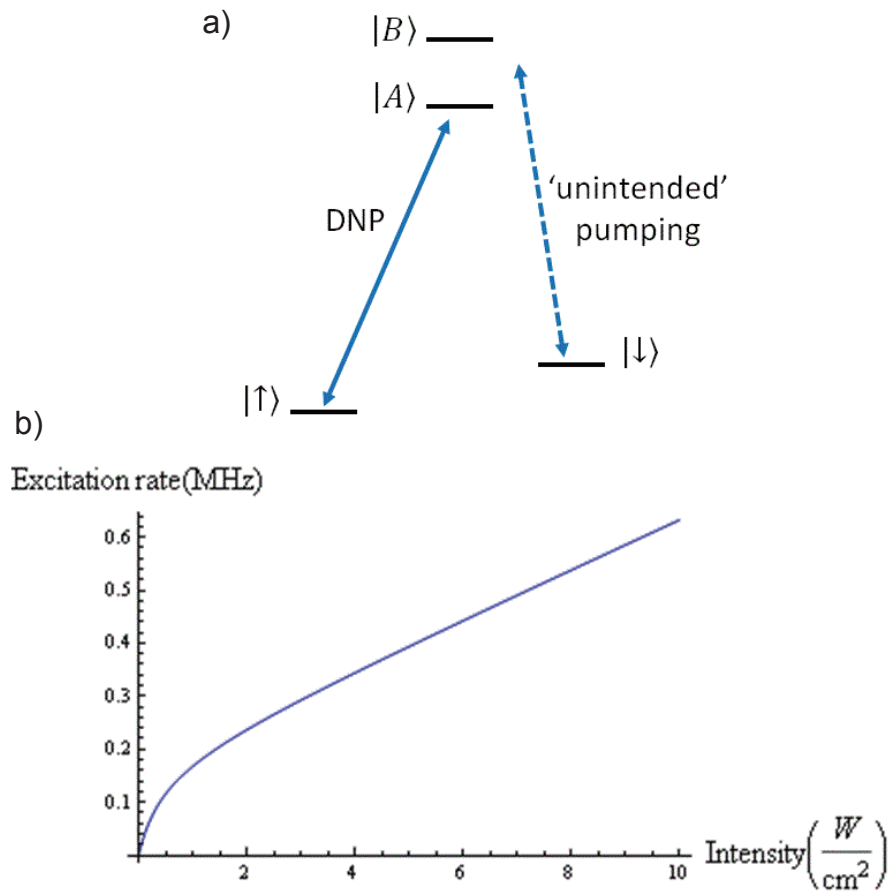


Figure 3.7: (a) When the pump laser is tuned to resonance with the transition $|\uparrow\rangle-|A\rangle$ there can be unintended coupling to the $|\downarrow\rangle-|B\rangle$. (b) This has as effect that the optical excitation rate (and with this the effective electron spin flip rate) increases linearly up to high intensities.

Chapter 4

Two-laser dynamic nuclear polarization with semiconductor electrons: feedback, suppressed fluctuations, and bistability near two-photon resonance

Abstract

We present how optical coherent population trapping (CPT) of the spin of localized semiconductor electrons stabilizes the surrounding nuclear spin bath via the hyperfine interaction, resulting in a state which is more ordered than the thermal equilibrium state. We find distinct control regimes for different signs of laser detuning and examine the transition from an unpolarized, narrowed state to a polarized state possessing a bistability. The narrowing of the state yields slower electron spin dephasing and self-improving CPT. Our analysis is relevant for a variety of solid state systems where hyperfine-induced dephasing is a limitation for using electron spin coherence.

This chapter is based on reference 4 on page 151

4.1 Introduction

Feedback control is a powerful tool to stabilize systems for which precision control is difficult to impose directly, such as the environment of an open quantum system. Reduction of noise from the environment is a major challenge on the road to harnessing delicate quantum effects such as superposition and entanglement. In particular spin states of defects and quantum dots in semiconductors display promising coherence properties for future applications, often being limited by disturbance from disordered nuclear spins in their environment. Here we show how optical coherent population trapping (CPT) of the spin of localized semiconductor electrons stabilizes the surrounding nuclear spins via feedback control. We find distinct control regimes for different signs of laser detuning and examine the transition from an unpolarized, narrowed state to a polarized state possessing a bistability. The narrowing of the state protects the electron spin against dephasing and yields self-improving CPT. Our analysis is relevant for a variety of solid state systems where hyperfine-induced dephasing is a limitation for using electron spin coherence.

A localized electron spin coupled to nuclear spins in a solid allows for studying the dynamics of mesoscopic spin ensembles. It forms a realization of the Gaudin (central spin) model [1] with the number of spins ranging from ~ 10 – 10^6 . From an application perspective the isolated dynamics of the electron spin is interesting as it can be used for quantum information processing. In thermal equilibrium the nuclear spins act as a source of dephasing for the electron spin. Optical orientation of the electron spin can be used to prepare out-of-equilibrium nuclear spin states via dynamic nuclear polarization (DNP) [2, 3, 4]. In turn, polarized nuclear spins induce an energy shift for the electron spin states, which can be described as an effective magnetic (Overhauser) field. DNP can also reduce thermal fluctuations in the nuclear spin polarization, which increases the electron spin dephasing time. This can be done either by creating a large nuclear spin polarization or by squeezing the polarization into a narrowed distribution [5, 6]. Significant achievements have been made for both cases via electron transport, electron spin resonance, and optical preparation techniques [4, 7, 8, 9, 10, 11, 12, 13, 14, 15, 4, 16, 17]. We present here how

optical coherent population trapping (CPT) of localized semiconductor electrons [18] stabilizes the surrounding nuclear spin bath in a state which is more ordered than the thermal equilibrium state.

CPT is the phenomenon where two-laser driving from the electron spin states to a common optically excited state displays –on exact two-photon resonance– a suppression of optical excitation due to destructive quantum interference in the dynamics [19], and is a key effect in quantum information processing [20]. Its sharp spectral feature allows for highly selective control over absorption and spontaneous emission of light. With atoms this has been applied in selective Doppler and sideband cooling [21, 22, 23]. Similarly, in semiconductors the CPT resonance can selectively address localized electrons that experience a particular Overhauser field [24, 25, 26]. This can lead to trapping of the combined electron-nuclear spin system in a dark state which was demonstrated as a measurement-based technique for reducing uncertainty of the nuclear spin state around a nitrogen vacancy center [15].

The CPT-based control scheme we propose relies on an autonomous feedback loop, existing for detuned lasers only, and does not require measurement or adaptation of control lasers [24]. Earlier work found such a feedback loop in an effective two-level description of a driven three-level Λ system [26]. We use a full description of the Λ system dynamics and uncover distinct control regimes for different signs of the detuning and examine the transition from an unpolarized, narrowed state for blue-detuned lasers to a polarized state possessing a bistability for red-detuned lasers. With a stochastic approach that was previously used in the context of electron spin resonance experiments [27, 11] we analyze the evolution of thermalized nuclear spins to a state of reduced entropy.

4.2 Candidate Λ -system: D^0X in GaAs.

We tailor our analysis to the case of the donor-bound electron in GaAs. Unlike Refs. [12, 28] our work does not include the hyperfine interaction between the hole and nuclear spins. It was shown [29] that this interaction can be put in an effective scalar form (even though it has magnetic dipole origin) with a coupling strength that is an order of magnitude smaller than

that for the electron. On this ground we choose to neglect it, although it should be noted that the bound hole spin in a symmetric potential (without heavy-light hole splitting) has a more complex spin structure, as was discussed in recent work [30]. Nevertheless, interaction with the hole spin can be important in self-assembled quantum dots where a non-collinear hole-nuclear spin coupling [31] arises due to anisotropy [32]. And furthermore, when the lattice is strained there will be a noncollinear interaction between the electron and nuclear spin [33], this we also do not consider in our model. In this sense our result is more in line with other recent works [34, 35] that have also discussed nuclear spin stabilization only mediated by the contact hyperfine interaction with the electron. The physical systems that are covered by our model are thus characterized by low strain and spherical symmetry of the confining potential. Besides the donor-bound electron in GaAs we expect it to be applicable to strain-free quantum dots [36] and other solid state spin defects where hyperfine contact interaction for the ground state electron is dominant. Our method thus expands the established CPT technique for coherent electron spin preparation and manipulation [37] to one that can also improve the electron spin dephasing time by nuclear spin preparation. It does not require hyperfine relaxation within the excited state and gives different features than [12], easily distinguishable in experiment. The prerequisites are a high nuclear spin temperature and a non-zero electron spin temperature (ensuring bidirectional DNP). In example calculations we use parameters that approach (in order of magnitude) the values that apply to localized electrons in GaAs [4].

Figure 4.1(a) presents the electronic part of our model: a Λ system with spin states $|1\rangle$ and $|2\rangle$ that each have an optical transition to state $|3\rangle$. Nuclear spin polarization gives an Overhauser shift $-(+)\hbar\delta$ of the state $|1\rangle$ ($|2\rangle$), and we assume the Overhauser shift of $|3\rangle$ to be negligible. The values of energy differences $\hbar\omega_{13}$ and $\hbar\omega_{23}$, and Zeeman splitting $\hbar\omega_z$ between these states are defined for $\delta = 0$. Two laser fields with frequencies ω_1 and ω_2 (and Rabi frequencies Ω_1 and Ω_2) selectively drive the two transitions. The decay and decoherence rates of the system are the spin flip rate Γ_s , excited state decay rate Γ_3 , spin decoherence rate γ_s

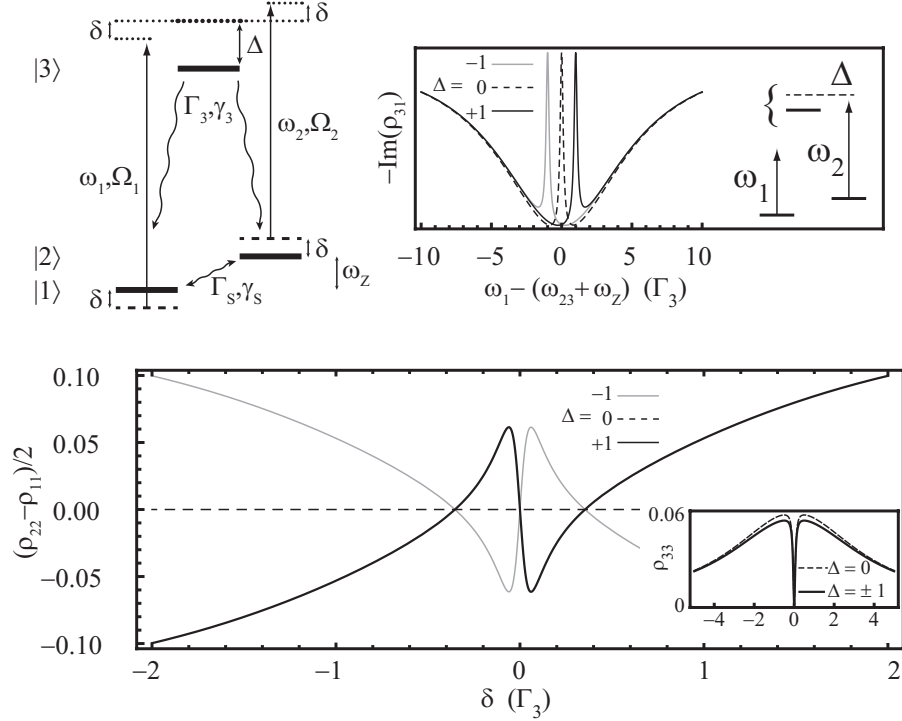


Figure 4.1: Electronic level scheme and response under two-laser driving. (a) Schematic of energies and shifts of the electronic three-level system. Thick black lines are the (not Overhauser shifted) spin states $|1\rangle$, $|2\rangle$ and optically excited state $|3\rangle$. Γ_s, γ_s and Γ_3, γ_3 are spin and excited state decay and decoherence rates, respectively. Two lasers (frequencies ω_1 and ω_2) couple to the system with Rabi frequencies Ω_1 and Ω_2 , excited state detuning Δ , and Overhauser shift δ (see further main text). (b) Conventional depiction of CPT (here for $\delta = 0$ Overhauser shift) showing the narrow CPT resonance within a broader absorption line. Laser 1 scans over the resonance while laser 2 is held fixed at $\omega_2 = \omega_{23} + \Delta$, for detunings Δ as labeled. (c) Electron spin polarization as a function of Overhauser shift δ , with lasers fixed at $\omega_1 = \omega_{13} + \Delta$ and $\omega_2 = \omega_{23} + \Delta$. Inset: trion population as a function of Overhauser shift (same parameters as main figure). In (b) and (c) results are presented as elements ρ_{ij} of the steady-state density matrix. Parameters are normalized with respect to $\Gamma_3 \equiv 1$: $\gamma_3 = 10, \Gamma_s = 10^{-4}, \gamma_s = 10^{-3}, \Omega_1 = \Omega_2 = 0.5$.

and excited state decoherence rate γ_3 . We take all decay rates symmetric for the two electron spin states (for Γ_s this implies temperature $k_B T \gg \hbar\omega_z$), to avoid needless complication of the discussion, but our conclusions remain valid for the non-symmetric case. For modeling the CPT effects we directly follow Ref. [20]. The Supplementary Information specifies this in our notation. For this system, CPT occurs for driving at two-photon resonance (TPR, *i.e.*, for $\delta = 0$, $\omega_1 = \omega_2 + \omega_z$). In the conventional picture of CPT only one laser is fixed at single laser detuning Δ while the other is scanned across the resonance. At the TPR point the system shows reduced absorption, getting trapped in a dark state that equals (for ideal spin coherence) $|\Psi\rangle \propto \Omega_2 |1\rangle - \Omega_1 |2\rangle$. Figure 4.1(b) presents this for different Δ in terms of the system's steady-state density-matrix element ρ_{13} .

4.3 Influence of Overhauser field on CPT

For our DNP analysis, however, we study CPT as a function of δ while the two lasers are fixed to exact TPR for $\delta = 0$. We formulate the laser detunings in such a way that the effect of an Overhauser shift on this configuration is emphasized: The detuning of laser 1 (2) from its corresponding transition is denoted as $\Delta - (+) \delta$. This is the electron's point of view on how a finite Overhauser shift breaks the ideal CPT condition, and the dependence on δ reflects the sharp spectral CPT feature. Figure 4.1(c) presents how this works out for the electron spin polarization, $(\rho_{22} - \rho_{11})/2$ in terms of the steady-state density matrix. The effect of a non-zero Overhauser shift is to break the TPR setting of the lasers. For $\Delta = 0$ this has no effect on the spin polarization since δ drives both lasers away from resonance by an equal amount. For finite Δ , however, the Overhauser shift leads to uneven detunings from the excited state, resulting in the electron spin polarization changing rapidly as a function of δ near TPR. It is interesting to observe that for $|\delta| \gtrsim 0.4$ the spin population has the sign which is expected from standard optical pumping (population is transferred from the spin state associated with the more resonant laser), whereas close to the TPR it has the opposite sign (see Supplementary Information). Moreover, the electron spin polarization acquires a sign change as the sign of

Δ is reversed. Notably, the excited state population (ρ_{33} , inset) shows no change with the sign of Δ , which distinguishes the feedback mechanism that we discuss from that which is dependent on the excited state population (which was described in [12]). How this electron spin polarization as a function of δ drives DNP (which in turn will influence δ) is the core of our further analysis. To this end, we consider the Λ -system to be embedded in the crystal lattice where it couples to nuclear spins within the electron wave function. We study the combined dynamics of the driven Λ system and its surrounding nuclear spin bath, and also take into account that this nuclear spin bath in turn couples to other nuclear spins of the crystal that are not in contact with the electron, leading to leakage of nuclear spin polarization by spin diffusion (Fig. 4.2(a)).

4.4 Hyperfine coupling

We first introduce relevant aspects of this hyperfine interaction. We concentrate on the common scenario where an external magnetic field is applied which defines a quantization axis for the spins, which we label $\hat{\mathbf{z}}$. This suppresses non-secular (not energy conserving) terms in the nuclear spin dipole-dipole interaction and we can approximate the nuclear spins to be frozen on the timescale of electron spin dynamics [38, 39, 40]. The hyperfine Hamiltonian has electron-nuclear flip-flop terms that describe the transfer of spin angular momentum along $\hat{\mathbf{z}}$ between the two systems (the Supplementary Information provides a summary in our notation). For a single nuclear spin coupled to an electron, treated perturbatively, this results in the relaxation equation [41]

$$\langle \dot{I}_z \rangle = -\Gamma_h \left(\langle I_z \rangle - \langle \bar{I}_z \rangle - \frac{I^2 + I}{S^2 + S} [\langle S_z \rangle - \langle \bar{S}_z \rangle] \right). \quad (4.1)$$

Here I and I_z are the nuclear spin quantum number and spin component along $\hat{\mathbf{z}}$, and similarly for electron spin S . The overbar indicates that the expectation value is taken at thermal equilibrium. The effective hyperfine relaxation rate Γ_h is proportional to $\tau_c / (1 + \omega_z^2 \tau_c^2)$, which reflects how the electron spin correlation time τ_c determines the spectral density of the fluctuating hyperfine coupling [42]. The nuclear spin flips along $\hat{\mathbf{z}}$ are allowed

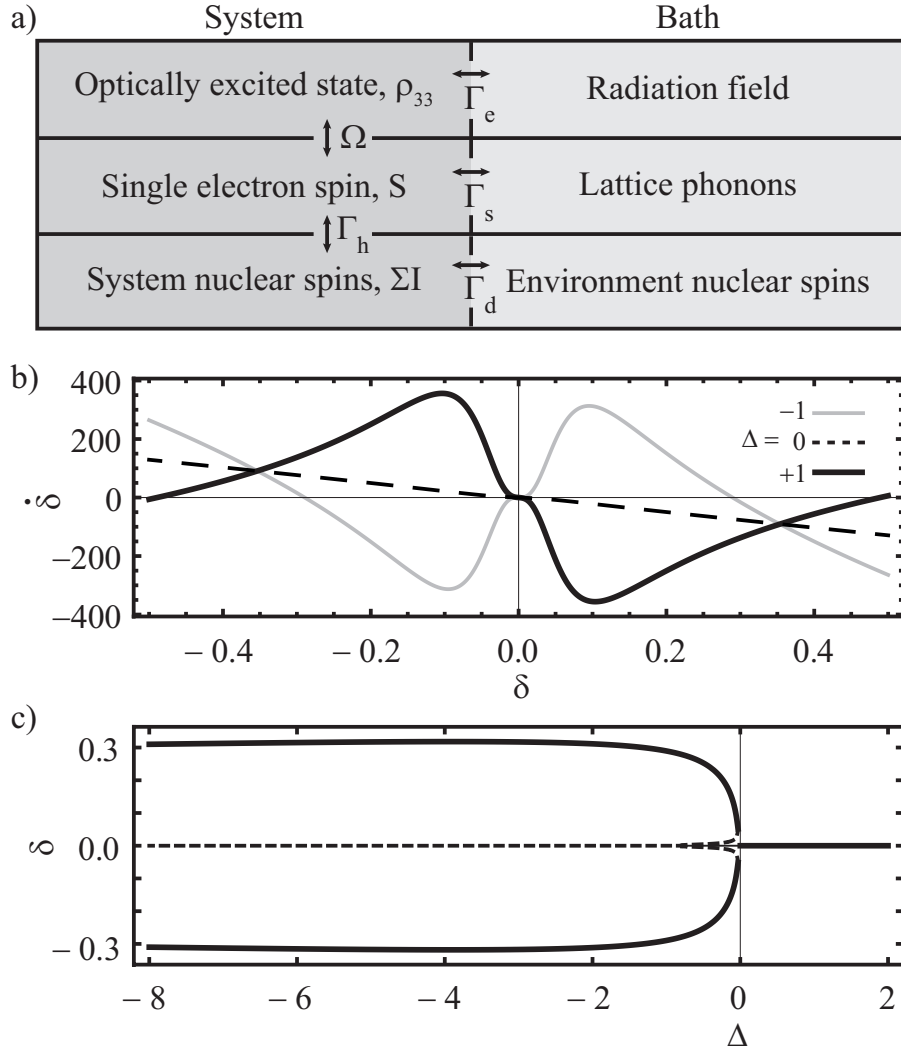


Figure 4.2: Open system schematic, response function and transition between distinct control regimes. (a) Overview of components and interactions of the laser-driven electron–nuclear-spin-ensemble system, with for each component its relaxation bath. Competition between the interactions and relaxation mechanisms govern the dynamics of the full system, see main text for details. (b) The rate $\dot{\delta}$ as a function of the Overhauser shift δ (Eq. (4.2)) that is experienced by the electron near CPT conditions, for detunings Δ as labeled and $\bar{\Gamma}_h/\Gamma_d = 0.01$. (c) Thick solid (dashed) lines display the one or two (un)stable stationary δ values ($\dot{\delta} = 0$) as a function of laser detuning Δ . The relaxation parameters and laser powers for (b) and (c) equal those of Fig. 4.1.

due to fluctuations in the electron spin component perpendicular to \hat{z} . These happen on the order of the intrinsic electron spin coherence time T_2 due to coupling to the crystal lattice. Additionally it is influenced by laser excitation because the repeated absorption and sponaneous emission also randomize the in plane component of the electron spin. Thus the quenching of optical excitation due to CPT near $\delta = 0$ has an influence on Γ_h . In our model we take this into account by modulating the equilibrium hyperfine interaction rate $\bar{\Gamma}_h$ with the optical excitation rate obtained from the driven Λ -system dynamics of Fig. 4.1 (see Supplementary Information). Equation (4.1) shows that $\langle I_z \rangle$ can be controlled by bringing the electron spin out of thermal equilibrium. By summing Eq. (4.1) over all nuclei we can express the rate of change of δ as a function of δ , forming a closed-loop system, which includes the dependence on the out-of-equilibrium electron spin polarization,

$$\dot{\delta} = -\Gamma_h [\delta - K \langle S_z \rangle] - \Gamma_d \delta, \quad (4.2)$$

where K is a constant determined by the strength of the hyperfine coupling (see Supplementary Information) and we used again the high temperature approximation $\langle \bar{S}_z \rangle = \langle \bar{\delta} \rangle = 0$. The last term of Eq. (4.2) incorporates the loss of nuclear spin polarization by diffusion to the environment at a rate Γ_d which we assume constant.

4.5 Influence of CPT on DNP: feedback

The polarization of the nuclear spin system is governed by the control dynamics of Eq. (4.2). The dependence of this control on driving CPT for the electron is shown in Fig. 4.2(b). Stable points are identified by $\dot{\delta} = 0$ and $\frac{\partial \dot{\delta}}{\partial \delta} < 0$. The dashed line represents the system driven by two lasers with $\Delta = 0$, and has strong similarity with thermal equilibrium (no laser driving) because the Overhauser shift does not lead to a change of the electron spin polarization (cf. the dashed line in Fig. 4.1c). The position of the stable point is at $\langle \bar{\delta} \rangle$, which we assumed zero. When the lasers are tuned to TPR for $\delta = 0$ while having a finite detuning Δ , two qualitatively different control regimes emerge. For the red-detuned case $\Delta = -1$ there are two stable points at $\delta \approx \pm 0.3$, and the nuclear spin system will thus

display a bistability. For the blue-detuned case $\Delta = +1$, however, there is again one stable point at $\delta = 0$. The transition between these two control regimes is shown in Fig. 4.2(c) where the thick black lines represent the stable point(s) for a range of detunings Δ . Even though the blue-detuned case displays the same stable point as the equilibrium case there is an enhanced response towards $\delta = 0$ for a region around this point. The effect of this gain becomes apparent when we study the stochastics of the nuclear spin polarization. Notably, the small plateaux in the traces of Fig. 4.2(b) at $\delta = 0$ are due to the CPT suppression of Γ_h .

4.6 Stochastic dynamics of the nuclear spin polarization

The stochastics of the nuclear spin polarization gives rise to the electron spin dephasing time that is observed in measurements, whether on an ensemble of Λ systems [43] or by repeated measurements on a single system [4]. In such cases each system experiences a different Overhauser shift, sampled from a probability distribution $P(\delta)$, and this directly translates into a distribution for the electron precession frequencies. This can be used to calculate the dephasing time T_2^* , indicating when information on the electron spin state has decayed to $1/e$ of its initial value (see Supplementary Information). The evolution of $P(\delta)$ under the control dynamics of Eq. (4.2) can be described by a Fokker-Planck equation [27, 44], in the continuum limit where the number of nuclear spins $N \gg 1$,

$$\dot{P} = \frac{2}{N} \frac{\partial}{\partial \delta} \left(-\dot{\delta} P + \frac{\delta_{\max}^2}{N} \frac{\partial}{\partial \delta} [\Gamma_d + \Gamma_h] P \right). \quad (4.3)$$

Here N is the number of system nuclear spins and δ_{\max} is the Overhauser shift for complete nuclear spin polarization (for simplicity, we describe the dynamics in the approximation where N spins with $I=\frac{1}{2}$ couple to the electron with equal strength [4]). Without laser driving Eq. (4.2) gives $\dot{\delta} = -(\Gamma_d + \Gamma_h)\delta$ and the steady state solution to Eq. (4.3) is a Gaussian with standard deviation $\sigma_\delta = \delta_{\max}/\sqrt{N}$, as expected in thermal equilibrium. With laser driving the control gain becomes nonlinear, as in Fig. 4.2(b), and we evaluate the steady-state solution $P_{ss}(\delta)$ numerically (see Supplementary Information). With Eq. (4.3) we can study the

evolution of the initial thermalized distribution $\bar{P}(\delta)$ while laser control is imposed via Eq. (4.2). The initial distribution depends on N and δ_{\max} . For our example calculations we take $N = 10^5$, $\delta_{\max} = 16.3$ and $K = 10\delta_{\max}/3$ (see Supplementary Information), representing the donor-bound electron in GaAs [43] which has $\Gamma_3 \approx 1$ GHz.

4.7 Results of the model

The evolution of $P(\delta)$ corresponding to the response functions from Fig. 4.2(b) is depicted in Fig. 4.3(a,b). For the blue-detuned case $P(\delta)$ gets narrowed and focusses around the stable point $\delta = 0$, while for the red-detuned case $P(\delta)$ splits apart and in the steady state it is divided between two stable points. During evolution the rate of change of $P(\delta)$ is at first lagging at $\delta = 0$, causing the central dip in the gray lines of Fig. 4.3(a) and the central peak in Fig. 4.3(b). This is due to the suppressed hyperfine relaxation rate Γ_h at CPT resonance. At long time scales this effect smooths out.

A thermodynamic interpretation of the narrowing effect is that when the driven Λ system is detuned from TPR, optical excitation converts low entropy laser light to higher entropy fluorescence light, resulting in an entropy flux away from the electron system. In turn, the electron acts as a controller on the nuclear spins, removing entropy from the spin bath and providing increased state information of the nuclear spins. Because the slow dynamics of the nuclei this effect is sustained after laser control is turned off, giving an enhanced dephasing time for subsequent electron spin manipulation. The evolution of T_2^* calculated from $P(\delta)$ as in Fig. 4.3(a) is presented in Fig. 4.3(c), where the evolution time is expressed in units of the nuclear spin diffusion time $\tau_n = 1/\Gamma_d$ (on the order of seconds to minutes). The nuclear spin bath attains a stable state with an increase in T_2^* of a factor of ~ 3.7 in $0.2\tau_n$. While this increase is moderate for the GaAs parameters used, it can be much more significant for systems with weaker nuclear spin diffusion (which can also be the case for GaAs when this is suppressed due to a Knight shift [45]). Notably, the resulting $P_{ss}(\delta)$ does not change with variation of $\bar{\Gamma}_h$ and Γ_d provided their ratio remains fixed. For the system nuclear spins this represents the ratio of

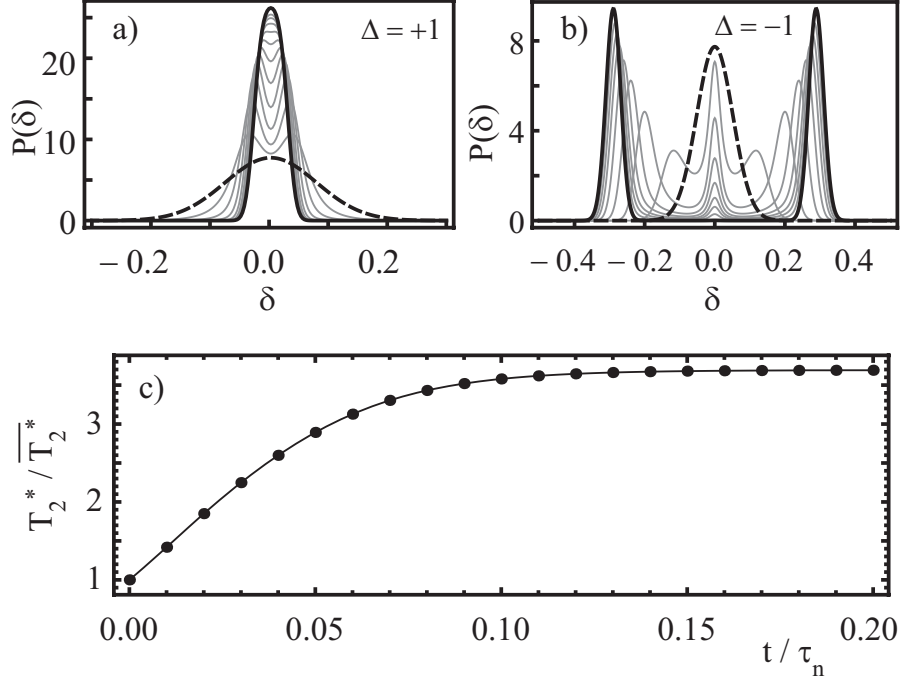


Figure 4.3: Evolution of the nuclear spin polarization probability distribution. Time evolution of $P(\delta)$ for a nuclear spin bath with $N = 10^5$, for cases that correspond to the curves in Fig. 4.2(b), with $\Omega_1 = \Omega_2 = 0.5$ and $\bar{\Gamma}_h/\Gamma_d = 0.01$. In (a) and (b) the dashed lines show the same initial (Gaussian) distribution at thermal equilibrium (before laser driving is switched on), black lines show the final steady-state distribution. The sign of the detuning Δ determines whether the driven system has mono- or bistable behavior. Panel (c) shows the improvement in electron spin dephasing time corresponding to the sequence of curves in (a).

coupling strength to the controller (electron spin) and the environment (Fig. 4.2(a)).

Figure 4.4 presents how the narrowing mechanism performs for different laser powers. At high power (Fig. 4.4(a,c), $\Omega_1 = \Omega_2 \equiv \Omega = 2$) the power broadening of the CPT resonance quenches the hyperfine rate Γ_h over a wide range around $\delta = 0$. This results in a weak response and the narrowing is only effective at the tails of the initial $P(\delta)$. At lower power (Fig. 4.4(b,d), $\Omega = 0.1$) there is a strong response around $\delta = 0$, indicating strong narrowing. However this does not extend far enough to include

the tails of the initial $P(\delta)$. The T_2^* improvement factor in both cases is minor, only 1.38 and 1.63 respectively. Optimal T_2^* enhancement is found at moderate laser powers. Figure 4.4(e) depicts the optimum values as a function of $\bar{\Gamma}_h/\Gamma_d$ where dots are calculated values. The inset shows how such an optimum is found from a map of T_2^*/\bar{T}_2^* for a range of laser powers and detunings, for $\bar{\Gamma}_h/\Gamma_d = 0.01$ (open circle in main figure). These numerical results show that the optimal enhancement closely agrees with the square root dependence $T_2^*/\bar{T}_2^* \propto (1/(1 + \Gamma_d/\bar{\Gamma}_h))^{1/2}$. This reflects how, for the system nuclear spins, the ratio between the coupling to the electron and to the environment nuclear spins (giving rise to $\bar{\Gamma}_h$ and Γ_d respectively) governs the optimal narrowing that can be achieved. This allows for estimating the maximal T_2^* enhancement in real solid state spin systems, where spin diffusion always plays a role.

In Ref. [12] a similar narrowing effect has been described and demonstrated for a quantum dot. The authors attribute it to the non-collinear hyperfine coupling for the hole spin in the optically excited state, while our result is based on electron-nuclear spin coupling. For paramagnetic defects, in general, either type of hyperfine coupling may dominate. To distinguish the two in experiment we point out two characteristics that are different and readily measurable. Firstly, the transition from narrowing to a regime of bistability with changing sign of the detuning only occurs for our model. Secondly, the narrowing in Ref. [12] improves with increasing power while for our model there is a particular laser power that gives the optimal narrowing (Fig. 4.4(e)).

4.8 Conclusion

The effects we have discussed are readily measurable since, for blue detuning, the transmission of the laser beams tuned central on a narrow CPT line increases when the electron spin dephasing time increases. Hence, the narrowing of the nuclear spin polarization distribution directly translates to enhanced laser transmission over time (or equivalently, in a reduced signal when detecting fluorescence) and as such comprises a self-improving CPT effect. Our method should be applicable to a wide range of spin defects in solid state.

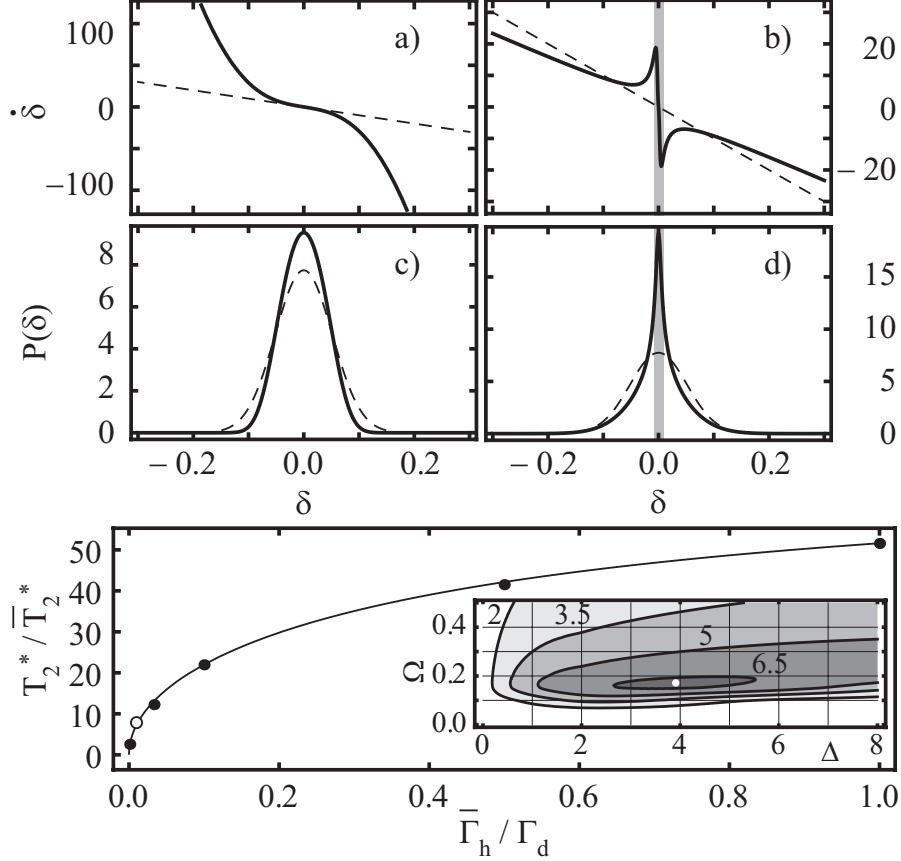


Figure 4.4: Optimization of the T_2^* improvement factor and dependence on nuclear spin relaxation rates. Traces of driving rate $\dot{\delta}$ as a function of δ (black lines in panels a,b) and their respective effect on the nuclear spin distributions (c,d), for Rabi frequencies $\Omega = 2$ (a,c) and $\Omega = 0.1$ (b,d). In (a,b) the dashed line is $\Gamma_d\delta$, representing the nuclear spin flip rate due to spin diffusion. In (c,d) the dashed line is the same (note different scale) nuclear spin probability distribution function at thermal equilibrium for $N = 10^5$ and $\bar{\Gamma}_h/\Gamma_d = 0.01$. The black line is the steady-state distribution under laser driving at detuning $\Delta = +1$ and Rabi frequencies $\Omega = 2$ (c) and $\Omega = 0.1$ (d). The gray area in (b,d) highlights the narrowing range. For low laser powers the driving curve (b) shows a steep response at $\delta = 0$ that acts as a strong force towards 0 for δ values around this point, and causes strong narrowing. The range over which narrowing takes place, however, is too small to cover the initial distribution. (e) Optimal T_2^* improvement as a function of $\bar{\Gamma}_h/\Gamma_d$. The simulated values (dots) reveal a dependence that scales with $(1/(1+\Gamma_d/\bar{\Gamma}_h))^{1/2}$. Inset: Improvement factor in T_2^* for a range of detunings and laser powers at $\bar{\Gamma}_h/\Gamma_d = 0.01$. The white dot marks the optimum where $T_2^*/\bar{T}_2^* = 6.75$.

4.9 Supplementary Information

4.9.1 Lindblad master equation for the driven three-level system

We present here more extensively our notation and approach for modeling the CPT physics in a driven three-level system. We directly follow Ref. [20]. The dynamics of the Λ system in Fig. 1(a) is governed by the Hamiltonian (in the rotating frame)

$$H_\Lambda = -\frac{\hbar}{2} \begin{pmatrix} 0 & 0 & \Omega_1^* \\ 0 & -4\delta & \Omega_2^* \\ \Omega_1 & \Omega_2 & 2(\Delta - 2\delta) \end{pmatrix}. \quad (4.4)$$

The equation of motion for the density matrix ρ_Λ that describes this electronic system as an open system with relaxation and decoherence is

$$\dot{\rho}_\Lambda = \frac{-i}{\hbar} [H_\Lambda, \rho_\Lambda] + \sum_{i,j} \left(L_{ij} \rho_\Lambda L_{ij}^\dagger - \frac{1}{2} \{ L_{ij}^\dagger L_{ij}, \rho_\Lambda \} \right) \quad (4.5)$$

(in our main text, elements ρ_{ij} are density matrix elements of ρ_Λ). Here, the Lindblad operators are defined by

$$L_{ij} = \alpha_{ij} |i\rangle \langle j|, \quad (4.6a)$$

$$\alpha = \frac{1}{2} \begin{pmatrix} \gamma_s & 2\Gamma_s & 2\Gamma_3 \\ 2\Gamma_s & \gamma_s & 2\Gamma_3 \\ 0 & 0 & \gamma_3 \end{pmatrix}. \quad (4.6b)$$

The matrix α contains all decay and decoherence rates of the system: spin flip rate Γ_s , excited state decay rate Γ_3 , spin decoherence rate γ_s and excited state decoherence rate γ_3 .

4.9.2 Sign change in the spin population

To understand the sign change in the spin population it is instructive to study the steady state solutions to equation 4.5. For this purpose we resort to the minimal case that describes the coherent population trapping by taking the only coupling to the environment to be Γ_3 , spontaneous decay

from $|3\rangle$ to $|1\rangle$ and $|2\rangle$. With all other incoherent processes set to zero, the steady state spin population can be written

$$\langle S_z \rangle = \frac{\rho_{22} - \rho_{11}}{2} = \frac{\Delta}{\gamma} \left(\text{Im}\rho_{12} + \frac{2\delta}{\Omega} \text{Im}\rho_{31} \right), \quad (4.7)$$

where $\text{Im}\rho_{12} = -\gamma\Omega^2\delta/\mathcal{D}$ and $\text{Im}\rho_{31} = \gamma\Omega\delta^2/\mathcal{D}$, with $\mathcal{D} = 2(\Omega^4 + (\Omega^2 + \Delta^2 + \gamma^2 + \delta^2)\delta^2)$. The part inside brackets in Eq. 4.7 changes sign when $\delta = \Omega/\sqrt{2}$, separating the optical orientation process into two regimes which can be intuitively understood: For $\delta \ll \Omega$ the term containing $\text{Im}\rho_{21}$ dominates. In this regime the excited state population as well as the single-photon absorption processes can be neglected. The level $|3\rangle$ can be removed from the dynamical equations 4.5 by adiabatic elimination [46] reducing the description of the state of the system to a 2-by-2 density matrix. Remarkably in this limit, close to the 2-photon Raman resonance, the dispersive interaction of the lasers causes a population transfer. It was demonstrated in [26] how in this regime, and additionally taking the limit of large detuning ($\Delta \gg \Gamma_3$), the effect of the optical excitation on the electron spin state can be described as an effective magnetic field acting along the external magnetic field direction and hence creating a steady state spin polarization. The resulting optical orientation is counterintuitive: This process populates the spin state that is coupled to the laser which is closer to resonance.

For $\delta \gg \Omega$ the term containing $\text{Im}\rho_{13}$ dominates. In this regime the system is far from the 2-photon Raman resonance, hence single-photon absorption and spontaneous emission determine the electron spin population. The resulting spin polarization has the sign that is expected from conventional optical pumping, i.e. the spin state that is coupled to the laser which is closer to resonance is now pumped empty.

4.9.3 Fermi contact hyperfine interaction

We consider the case where the hyperfine interaction between the Λ system and the nuclear spin is dominated by the Fermi contact interaction for the ground state electron. This interaction is described by the Hamiltonian

$$H_f = \frac{4}{3}\mu_0\mu_B \sum_i A_i \mathbf{I}_i \cdot \mathbf{S}, \quad (4.8)$$

where $A_i = \hbar\gamma_i|\psi_e(\mathbf{r}_i)|^2$. The gyromagnetic factor, γ_i , and the electron wave function at the position of a nucleus, $\psi_e(\mathbf{r}_i)$, characterize the interaction strength with the i 'th nuclear spin. The spin operators are defined to have eigenvalues $m_J = -J, \dots, J$ for any spin quantum number J . This interaction term may be viewed in the form of a Zeeman interaction, $H = -\boldsymbol{\mu} \cdot \mathbf{B}_n$, with $\boldsymbol{\mu} = -g\mu_B\mathbf{S}$ the electron spin magnetic moment. The effective magnetic field due to the nuclei acting on the electron is then

$$\mathbf{B}_n = \frac{4}{3g}\mu_0 \sum_i A_i \mathbf{I}_i. \quad (4.9)$$

In an external magnetic field it is convenient to expand the $\mathbf{I} \cdot \mathbf{S}$ product using ladder operators. The total Hamiltonian becomes

$$H = H_z + H_f, \quad (4.10a)$$

$$H_z = \hbar\omega_z S_z + \sum_i \hbar\omega_i I_{i,z}, \quad (4.10b)$$

$$H_f = \frac{2}{3}\mu_0\mu_B \sum_i A_i (2I_{i,z}S_z + I_{i,+}S_- + I_{i,-}S_+). \quad (4.10c)$$

Equation (4.10b) represents the Zeeman energy of the electron spin and the nuclear spins in an external magnetic field applied along $\hat{\mathbf{z}}$. The first term within the summation in Eq. (4.10c) adds to the external field an effective magnetic (Overhauser) field $B_{n,z}$. To calculate its expectation value $\langle B_{n,z} \rangle = \text{Tr}(B_{n,z}\rho_n)$, where ρ_n is the reduced density matrix comprising the nuclear spin state, it is in principle required to know the interaction strengths for all nuclei. In the case of GaAs this is well studied and $\langle B_{n,z} \rangle \approx \langle I_z \rangle \cdot 3.53 \text{ T}$ [40], and the maximum field is $B_{\text{max}} = 5.30 \text{ T}$. The Overhauser field $B_{n,z}$ translates to the Overhauser shift δ used in the main text according to $\delta = \frac{1}{2}g\mu_B B_{n,z}/\hbar$. This yields $\delta_{\text{max}} = 16.3 \text{ GHz}$. To describe DNP we use a so-called box model [4] where the electron couples equally to a number of N nuclear spins. This amounts to the change $\sum_i A_i \rightarrow A \sum_{i=1}^N$ with A the average interaction strength per nucleus. In our calculations we approximate GaAs by choosing $N = 10^5$.

The constant K in Eq. (2) is

$$K = \frac{4\mu_0\mu_B}{3\hbar} \sum_i A_i \frac{I_i^2 + I_i}{S^2 + S}. \quad (4.11)$$

For GaAs, $I_i = 3/2$ for all nuclei. So $K = 10\delta_{\max}/3 = 54.3$ GHz.

4.9.4 Hyperfine relaxation rate

The cross relaxation between the electron spin and the nuclear spins is facilitated by a modulation of the hyperfine coupling due to random jumps in the electron spin state. These jumps occur on average after a correlation time τ_c . The relaxation rate is then the product of the average hyperfine coupling, the fraction of time the electron is present (f_e) and the spectral density of the electron spin fluctuations [47, 4],

$$\Gamma_h = \left(\frac{A}{N\hbar} \right)^2 2f_e \frac{\tau_c}{1 + (\omega_z + \delta)^2 \tau_c^2}. \quad (4.12)$$

The relaxation process of the $\hat{\mathbf{z}}$ projection of the nuclear spin is allowed due to jumps in the perpendicular component of \mathbf{S} . For the undriven electron spin τ_c equals $T_2 = 1/\gamma_s$, *i.e.* the intrinsic decoherence time of the electron spin. Under conditions of laser driving τ_c is reduced when the laser driving leads to repeated excitation and spontaneous emission. The sharp variation of absorption around CPT has to be taken into account in our model. To deal with this we assume that we operate under conditions where $\omega_z \gg \delta$ and $\omega_z \gg 1/\tau_c$ so that the spectral density is approximately proportional to the inverse correlation time

$$\frac{\tau_c}{1 + (\omega_z + \delta)^2 \tau_c^2} \approx \frac{1}{\omega_z^2 \tau_c}. \quad (4.13)$$

In addition, we take the inverse correlation time to be enhanced by the amount of optical transitions that disturb the electron spin state, *i.e.* $1/\tau_c = (\rho_{11} + \rho_{22})\gamma_s + \rho_{33}\Gamma_e$, where we obtain the ρ_{ii} from the Λ system model. For the undriven spin ρ_{33} is zero and $1/\tau_c = \gamma_s$, whereas for the driven electron spin the last term $\rho_{33}\Gamma_e$ represents the interruption of coherent spin dynamics by absorption and spontaneous emission. Around $\delta = 0$, ρ_{33} varies strongly with δ .

In our simulations we specify a value for $\bar{\Gamma}_h/\Gamma_d$ (this value is reported in the captions of Figs. 2-4) where $\bar{\Gamma}_h$ is the hyperfine relaxation rate of the equilibrium system (no laser driving). This provides the basis for the effective value of Γ_h , for which we can calculate its dependence on δ

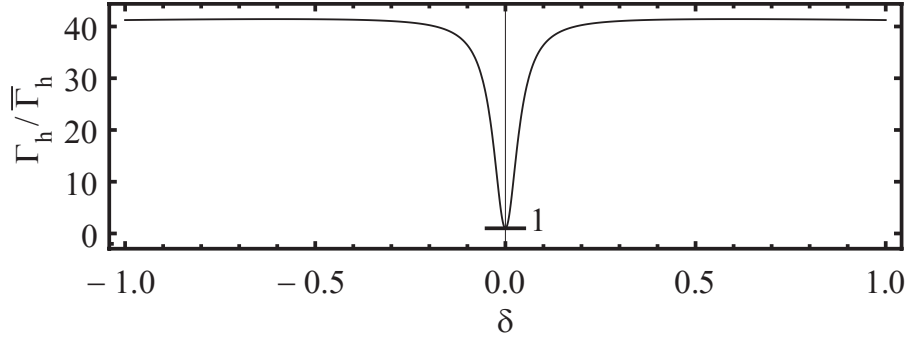


Figure 4.5: Modulation of the hyperfine relaxation rate Γ_h by the Overhauser shift δ under conditions of two-laser driving. Detuning $\Delta = 1$, parameters $\Omega_{1,2}$, Γ_s , γ_s , Γ_3 , γ_3 are as in Fig. 1. This graph has been used for the calculations for Figs. 2–4.

through τ_c . How this dependence controls a modulation of the effective value for $\Gamma_h/\bar{\Gamma}_h$ near CPT conditions is presented in Fig. 4.5 for a specific set of optical driving parameters (see caption).

4.9.5 Steady state solution to the Fokker-Planck equation

A steady state ($\dot{P} = 0$) solution to Eq. 3 is

$$P_{ss}(\delta) = \eta \exp\left(-\int_0^\delta f_1(x)/f_2(x)dx\right),$$

where

$$f_1(x) = -\dot{\delta}(x) + \delta_{\max}^2 \frac{\partial}{\partial x} (\Gamma_d + \Gamma_h(x))/N,$$

$$f_2(x) = \delta_{\max}^2 (\Gamma_d + \Gamma_h(x))/N$$

and η is a number that is fixed by the normalization condition $\int P(\delta) d\delta = 1$. A special solution arises in the case when $f_1(x) = ax$ and $f_2(x) = b$ with a, b constant. Then the steady state distribution is Gaussian with standard deviation $\sigma = (b/a)^{1/2}$.

4.9.6 Electron-spin dephasing from hyperfine interaction with a nuclear spin bath

Because of the slow dynamics of the nuclear spins compared to the electron spin, each measurement on the electron spin is subject to an Overhauser field $B_{n,z}$ sampled from a distribution. For example, at thermal equilibrium at the high temperatures that we consider (for nuclear spins), this is a Gaussian distribution with mean $\langle B_{n,z} \rangle = 0$ and standard deviation σ_B . For a measurement on an ensemble of electron spins (or many separate single spin measurements), one will observe inhomogeneous dephasing as a function of time t . This can be parameterized with a function $C(t)$ that evolves from no dephasing to complete dephasing on a scale from 1 to 0:

$$C(t) = \left| \int_{-\infty}^{+\infty} P(B) \exp\left(-\frac{ig\mu_B B t}{\hbar}\right) dB \right|. \quad (4.14)$$

Here $P(B)$ is the probability distribution for the total field $B = B_{ext} + B_{n,z}$ (where B_{ext} is the externally applied magnetic field), taken over an ensemble of electrons. This expression captures the gradual loss of information about S_x and S_y as a function of time. For the Gaussian distribution at thermal equilibrium

$$\bar{P}(B) = \frac{1}{\sqrt{2\pi\sigma_B^2}} \exp\left(-\frac{B^2}{2\sigma_B^2}\right). \quad (4.15)$$

The dephasing time scale T_2^* is defined as the time where Eq. (4.14) reduces to $1/e$. For the Gaussian distribution $\bar{P}(B)$, Eq. (4.14) yields $C(t)$ in the form $\exp[-(t/T_2^*)^2]$ with the inhomogeneous dephasing time

$$T_2^* = \frac{\sqrt{2}\hbar}{|g|\mu_B\sigma_B}. \quad (4.16)$$

The steady state distributions obtained from the feedback model with nonlinear response are not Gaussian, for those no simple expression for T_2^* is available. We define T_2^* as the time at which $C(t)$ has dropped to $1/e$ of its initial value, which is obtained by numerical evaluation of Eq. 4.14. Further, it is straightforward to calculate with this definition a value for T_2^* for any of the distributions $P(\delta)$ that is presented in the main text (using $\delta = \frac{1}{2}g\mu_B B_{n,z}/\hbar$).

References

- [1] Gaudin, M. Diagonalisation d'une classe d'hamiltoniens de spin. *Journal de Physique* **37**, 1087–1098 (1976).
- [2] Lampel, G. Nuclear dynamic polarization by optical electronic saturation and optical pumping in semiconductors. *Phys. Rev. Lett.* **20**, 491–493 (1968).
- [3] Brown, S. W., Kennedy, T. A., Gammon, D. & Snow, E. S. Spectrally resolved overhauser shifts in single GaAs/al_xga_{1-x}As as quantum dots. *Phys. Rev. B* **54**, R17339–R17342 (1996).
- [4] Urbaszek, B. *et al.* Nuclear spin physics in quantum dots: An optical investigation. *Rev. Mod. Phys.* **85**, 79–133 (2013).
- [5] Coish, W., Fischer, J. & Loss, D. Free-induction decay and envelope modulations in a narrowed nuclear spin bath. *Phys. Rev. B* **81**, 165315 (2010).
- [6] Barnes, E., Cywiński, L. & Das Sarma, S. Nonperturbative master equation solution of central spin dephasing dynamics. *Phys. Rev. Lett.* **109**, 140403 (2012).
- [7] Coish, W. A. & Loss, D. Hyperfine interaction in a quantum dot: Non-markovian electron spin dynamics. *Phys. Rev. B* **70**, 195340 (2004).
- [8] Greilich, A. *et al.* Nuclei-induced frequency focusing of electron spin coherence. *Science* **317**, 1896–1899 (2007).
- [9] Reilly, D. J. *et al.* Suppressing spin qubit dephasing by nuclear state preparation. *Science* **321**, 817–821 (2008).
- [10] Latta, C. *et al.* Confluence of resonant laser excitation and bidirectional quantum-dot nuclear-spin polarization. *Nature Physics* **5**, 758–763 (2009).
- [11] Vink, I. T. *et al.* Locking electron spins into magnetic resonance by electronnuclear feedback. *Nature Physics* **5**, 764–768 (2009).
- [12] Xu, X. *et al.* Optically controlled locking of the nuclear field via coherent dark-state spectroscopy. *Nature* **459**, 1105–1109 (2009).
- [13] Bluhm, H., Foletti, S., Mahalu, D., Umansky, V. & Yacoby, A. Enhancing the coherence of a spin qubit by operating it as a feedback loop that controls its nuclear spin bath. *Phys. Rev. Lett.* **105**, 216803 (2010).
- [14] Ladd, T. D. *et al.* Pulsed nuclear pumping and spin diffusion in a single charged quantum dot. *Phys. Rev. Lett.* **105**, 107401 (2010).
- [15] Togan, E., Chu, Y., Imamoglu, A. & Lukin, M. D. Laser cooling and real-time measurement of the nuclear spin environment of a solid-state qubit. *Nature* **478**, 497–501 (2011).
- [16] Hansom, J. *et al.* Environment-assisted quantum control of a solid-state spin via coherent dark states. *Nature Physics* **10**, 725–730 (2014).
- [17] Stanley, M. J. *et al.* Dynamics of a mesoscopic nuclear spin ensemble interacting with an optically driven electron spin. *ArXiv e-prints* (2014). 1408.6437.

- [18] Fu, K.-M., Santori, C., Stanley, C., Holland, M. & Yamamoto, Y. Coherent population trapping of electron spins in a high-purity *n*-type gas semiconductor. *Phys. Rev. Lett.* **95**, 187405 (2005).
- [19] Arimondo, E. & Orriols, G. Optical orientation in a system of electrons and lattice nuclei in semiconductors. theory. *Lett. Nuovo Cimento* **17**, 333–338 (1976).
- [20] Fleischhauer, M., Imamoglu, A. & Marangos, J. P. Electromagnetically induced transparency: Optics in coherent media. *Rev. Mod. Phys.* **77**, 633–673 (2005).
- [21] Aspect, A., Arimondo, E., Kaiser, R., Vansteenkiste, N. & Cohen-Tannoudji, C. Laser cooling below the one-photon recoil energy by velocity-selective coherent population trapping. *Phys. Rev. Lett.* **61**, 826–829 (1988).
- [22] Morigi, G., Eschner, J. & Keitel, C. H. Ground state laser cooling using electromagnetically induced transparency. *Phys. Rev. Lett.* **85**, 4458–4461 (2000).
- [23] Roos, C. F. *et al.* Experimental demonstration of ground state laser cooling with electromagnetically induced transparency. *Phys. Rev. Lett.* **85**, 5547–5550 (2000).
- [24] Stepanenko, D., Burkard, G., Giedke, G. & Imamoglu, A. Enhancement of electron spin coherence by optical preparation of nuclear spins. *Phys. Rev. Lett.* **96**, 136401 (2006).
- [25] Issler, M. *et al.* Nuclear spin cooling using overhauser-field selective coherent population trapping. *Phys. Rev. Lett.* **105**, 267202 (2010).
- [26] Korenev, V. L. Multiple stable states of a periodically driven electron spin in a quantum dot using circularly polarized light. *Phys. Rev. B* **83**, 235429 (2011).
- [27] Danon, J. & Nazarov, Y. V. Nuclear tuning and detuning of the electron spin resonance in a quantum dot: Theoretical consideration. *Phys. Rev. Lett.* **100**, 056603 (2008).
- [28] Shi, X.-F. Nuclear spin polarization in a single quantum dot pumped by two laser beams. *Phys. Rev. B* **87**, 195318 (2013).
- [29] Fischer, J., Coish, W. A., Bulaev, D. V. & Loss, D. Spin decoherence of a heavy hole coupled to nuclear spins in a quantum dot. *Phys. Rev. B* **78**, 155329 (2008).
- [30] Kavokin, K. V. & Koudinov, A. V. Dynamical polarization of nuclear spins by acceptor-bound holes in a zinc-blende semiconductor. *Phys. Rev. B* **88**, 235202 (2013).
- [31] Yang, W. & Sham, L. Collective nuclear stabilization in single quantum dots by noncollinear hyperfine interaction. *Phys. Rev. B* **85**, 235319 (2012).
- [32] Koudinov, A., Akimov, I., Kusrayev, Y. & Henneberger, F. Optical and magnetic anisotropies of the hole states in stranski-krastanov quantum dots. *Phys. Rev. B* **70**, 241305 (2004).
- [33] Dzhioev, R. I. & Korenev, V. L. Stabilization of the electron-nuclear spin orientation in quantum dots by the nuclear quadrupole interaction. *Phys. Rev. Lett.* **99**, 037401 (2007).

-
- [34] Barnes, E. & Economou, S. E. Electron-nuclear dynamics in a quantum dot under nonunitary electron control. *Phys. Rev. Lett.* **107**, 047601 (2011).
- [35] Economou, S. E. & Barnes, E. Theory of dynamic nuclear polarization and feedback in quantum dots. *Phys. Rev. B* **89**, 165301 (2014).
- [36] Sallen, G. *et al.* Nuclear magnetization in gallium arsenide quantum dots at zero magnetic field. *Nature communications* **5** (2014).
- [37] Yale, C. G. *et al.* All-optical control of a solid-state spin using coherent dark states. *Proceedings of the National Academy of Sciences* **110**, 7595–7600 (2013).
- [38] Abragam, A. *The Principles of Nuclear Magnetism*, chap. 4, 104–105 (Oxford University Press, London, 1961).
- [39] D'yakonov, M. & Perel', V. Optical orientation in a system of electrons and lattice nuclei in semiconductors. theory. *JETP* **38**, 177 (1974).
- [40] Paget, D., Lampel, G., Sapoval, B. & Safarov, V. I. Low field electron-nuclear spin coupling in gallium arsenide under optical pumping conditions. *Phys. Rev. B* **15**, 5780–5796 (1977).
- [41] Abragam, A. *The Principles of Nuclear Magnetism*, chap. 8, 311 (Oxford University Press, London, 1961).
- [42] Abragam, A. *The Principles of Nuclear Magnetism*, chap. 8, 272–289 (Oxford University Press, London, 1961).
- [43] Sladkov, M. *et al.* Electromagnetically induced transparency with an ensemble of donor-bound electron spins in a semiconductor. *Phys. Rev. B* **82**, 121308 (2010).
- [44] Danon, J. *Nuclear Spin Effects in Nanostructures*. Ph.D. thesis, Delft University of Technology (2009). The derivation of the Fokker Planck equation for the nuclear spin polarization can be found in chapter 3. Our Eq. (4.3) is identical to their equation (3.7), but we have expressed \dot{P} in terms of δ , Γ_d and Γ_h .
- [45] Deng, C. & Hu, X. Nuclear spin diffusion in quantum dots: Effects of inhomogeneous hyperfine interaction. *Phys. Rev. B* **72**, 165333 (2005).
- [46] Brion, E., Pedersen, L. H. & Mølmer, K. Adiabatic elimination in a lambda system. *Journal of Physics A: Mathematical and Theoretical* **40**, 1033 (2007).
- [47] Abragam, A. *The Principles of Nuclear Magnetism* (Oxford University Press, London, 1961).

Chapter 5

Stabilizing nuclear spins around semiconductor electrons via the interplay of optical coherent population trapping and dynamic nuclear polarization

Abstract

We experimentally demonstrate how coherent population trapping (CPT) for donor-bound electron spins in GaAs results in autonomous feedback that prepares stabilized states for the spin polarization of nuclei around the electrons. CPT was realized by excitation with two lasers to a bound-exciton state. Transmission studies of the spectral CPT feature on an ensemble of electrons directly reveal the statistical distribution of prepared nuclear spin states. Tuning the laser driving from blue to red detuned drives a transition from one to two stable states. Our results have importance for ongoing research on schemes for dynamic nuclear spin polarization, the central spin problem and control of spin coherence.

This chapter is based on reference 7 on page 151

5.1 Introduction

Following the emergence of electron spins in quantum dots and solid state defects as candidates for spin qubits it has become a major goal to realize control over the nuclear spins in such nanostructures. In many experimental settings, interaction with disordered nuclear spins in the crystal environment is detrimental to the coherent evolution of carefully prepared electron spin states [1, 2, 3]. Preparation of nuclear spins in a state that has reduced spin fluctuations with respect to the thermal equilibrium state will help to overcome this problem [4]. Proposals to achieve this goal have been put forward for electron spin resonance (ESR) on one- or two-electron quantum dots [5, 6], and for optical preparation techniques that either rely on a quantum measurement technique [7, 8] or a stochastic approach [9, 10, 11]. Experimental advances have been made with ESR and optical techniques on single quantum dots [12, 13, 14, 15, 16, 17, 18] and nitrogen-vacancy centers [19], and on quantum dot ensembles [20, 21].

Several of these works [8, 15, 9, 10, 19, 11, 18] make use of the optical response of the electronic system near the coherent-population-trapping resonance (CPT, explained below) because it is highly sensitive to perturbations from nuclear spins. Notably, these experiments so far have focussed on quantum dots where, due to the particular anisotropic confinement, hyperfine coupling with a hole-spin in the excited state is reported to dominate [15]. In recent work [22] we discussed how the interplay between electron-nuclear spin interaction and CPT influences the stochastics of the nuclear spin bath for a class of systems where hyperfine interaction with the ground-state electron spin dominates.

Here we report experiments on this latter class of systems. We demonstrate an all-optical technique that stabilizes the nuclear spin bath around localized donor electrons in GaAs into a non-thermal state under conditions of two-laser optical pumping. We show that the nuclear spin system is directed either towards a single stable state or (probabilistically) towards one of two stable states, depending on laser detuning from the excited state. Our results show how feedback control arises from the interplay between CPT and dynamic nuclear spin polarization (DNP), and confirm that the electron-spin hyperfine interaction dominates for our sys-

tem (despite the strong similarity with the negatively charged quantum dot). Our results indicate that this interplay can be used to create stable states of nuclear polarization with reduced fluctuations.

5.2 Experimental methods

We perform measurements on the nuclear spin dynamics in a 10- μm thick MBE-grown film of GaAs doped with Si donors at a concentration of $\sim 3 \times 10^{13} \text{ cm}^{-3}$, which is well below the metal-insulator transition (at $\sim 10^{16} \text{ cm}^{-3}$). The wafer is cleaved in 2-by-2 mm^2 parts along the $\langle 110 \rangle$ crystal axes. The film is removed from a GaAs substrate by wet etching an AlAs buffer layer in HF. The film is then transferred to a sapphire substrate which allows us to do transmission measurements in a cryogenic microscope [23]. Measurements are performed at a temperature of $T = 4.2 \text{ K}$ and magnetic field of $B_{ext} = 5.9 \text{ T}$. The sample is mounted such that the magnetic field direction is along the $\langle 110 \rangle$ axis. Light from tunable continuous-wave lasers (Coherent MBR-110) is delivered to the sample by a polarization-maintaining fiber and passes through the sample along the $\langle 100 \rangle$ axis. Transmitted light is collected in a multimode fiber and detected by an avalanche photodiode outside the cryostat. For getting reproducible data it was essential to stabilize laser powers within 1% and laser frequency drift within 10 MHz.

The optical transitions that we address are from the donor-bound electron spin states ($|\uparrow\rangle$, $|\downarrow\rangle$) to a level of the bound trion ($|D^0X\rangle$), that consists of two electrons and one hole bound at the silicon donor. These three states form a Λ -type energy level configuration, further defined in Fig. 5.1(a). The magnetic field is applied perpendicular to the light propagation direction (Voigt geometry) such that the optical transitions have polarization selection rules discriminating between horizontally ($\sigma_{+,-}$, coupling to $|\uparrow\rangle - |D^0X\rangle$) and vertically (π , coupling to $|\downarrow\rangle - |D^0X\rangle$) polarized light.

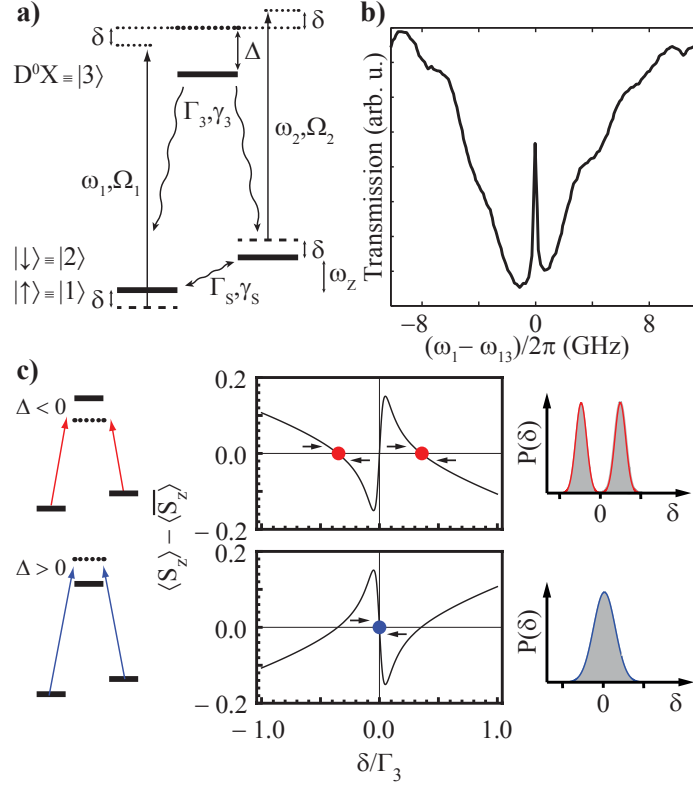


Figure 5.1: Energy levels and feedback control scheme. (a) Thick black lines are the spin states $|1\rangle$, $|2\rangle$ and optically excited state $|3\rangle$. Γ_s, γ_s and Γ_3, γ_3 are spin and excited state decay and dephasing rates, respectively. Two lasers at frequencies ω_1, ω_2 couple to the system with Rabi strengths Ω_1 and Ω_2 , excited state detuning Δ , and Overhauser shift δ (see main text). The energy splittings ω_{13}, ω_{23} and ω_Z are fixed at the values for $\delta = 0$ (\hbar omitted for brevity). (b) Measured CPT signature in the n -GaAs sample (here for $\omega_2 = \omega_{23}$ and $\delta = 0$). (c) Left panel: two distinct control regimes for nuclear spin control. Middle panel: optically-induced electron spin polarization ($\langle S_z \rangle - \langle \bar{S}_z \rangle$) as a function of Overhauser shift δ , with lasers fixed at $\omega_1 = \omega_{13} + \Delta$ and $\omega_2 = \omega_{23} + \Delta$, displays two stable states of the nuclear spin bath for $\Delta < 0$ (red dots) and one stable state for $\Delta > 0$ (blue dot). Right panel: expected steady state Overhauser shift distributions. Calculations with parameters $\gamma_3 = 10$, $\Gamma_s = 10^{-4}$, $\gamma_s = 10^{-3}$, $\Omega_1 = \Omega_2 = 0.5$, $\Delta = \pm 1$ normalized to $\Gamma_3 \equiv 1$ [22].

5.3 Measurement of the nuclear spin distribution by CPT

We first demonstrate CPT for our system. CPT is a narrow resonance in two-laser driving as in Fig. 5.1(a) [24] where the system gets trapped in a dark state (for ideal spin coherence $|\Psi\rangle \propto \Omega_2 |\uparrow\rangle - \Omega_1 |\downarrow\rangle$). In transmission this appears as a narrow window of increased transparency within the broader absorption dip when one laser is scanning while the other is fixed (Fig. 5.1(b)). Its position signals two-photon resonance, and occurs where $\omega_1 - \omega_2$ equals the the electron spin splitting. The lineshape of the CPT resonance can reveal information about the electron spin states, which can be obtained by fitting the curve in Fig. 5.1(b) to the Lindblad equation for the Λ -system [25]. Our *n*-GaAs samples yield an inhomogeneous dephasing time $T_2^* \approx 3$ ns [24]. However, the homogeneous dephasing time T_2 has been estimated to be at least $7 \mu\text{s}$ [26] with a spin-echo technique. The discrepancy between T_2 and T_2^* is largely due to dephasing caused by $\sim 10^5$ disordered nuclear spins per electron.

Due to the Fermi contact hyperfine interaction, a non-zero nuclear spin polarization exerts an effective magnetic (Overhauser) field B_n on the electron spin and causes a shift of the electron spin levels, denoted by δ in Fig. 5.1(a). The value of $\delta = p\delta_{\text{max}}$ is proportional to the nuclear spin polarization $p \in [-1, 1]$, where δ_{max} is the maximum shift set by the hyperfine interaction strength. For the donor electron in GaAs $\delta_{\text{max}} = 24.5$ GHz (obtained from the maximum Overhauser field [27] via $\delta = g\mu_B B_n / 2\hbar$ with g-factor $g = -0.41$ [24]). The thermal equilibrium properties of the nuclear spin bath are well approximated by considering N non-interacting spins I with gyromagnetic ratio γ . Then p and its variance σ_p^2 are in the high temperature limit $\hbar\gamma B_{\text{ext}} / k_B T \ll 1$ (our experimental conditions) $p = \hbar\gamma B_{\text{ext}}(I + 1) / 3k_B T \approx 0$ and $\sigma_p^2 = (I + 1) / 3IN - p^2$ [4].

Because nuclear spin dynamics is slow as compared to the electron's, light interacting with the system sees a snapshot of the Overhauser shift taken from a distribution $P(\delta)$. A measurement on an ensemble of these systems should account for averaging over $P(\delta)$. The CPT lineshape of Fig. 5.1(b) arises from the transmittance, with a susceptibility that is

averaged over $P(\delta)$,

$$T(\omega_i) = \exp\left(-\rho \frac{\omega_i d}{c} \int_{-\infty}^{+\infty} P(\delta) \chi_i''(\omega_i, \delta) d\delta\right), \quad (5.1)$$

where d is the thickness of the medium, ρ the density of donors, c the speed of light, $i = 1, 2$ labels the laser fields. Here χ_i is the susceptibility for the laser field for a fixed δ . It can be calculated from the Lindblad equation and depends on other system parameters implicitly [22]. At thermal equilibrium $P(\delta)$ is a Gaussian centered at zero with variance $\sigma_\delta^2 = \delta_{\max} \sigma_p^2$. For $I = 3/2$ and $N = 10^5$ it has a width (FWHM) of $2\sqrt{2 \log(2)} \sigma_\delta = 136$ MHz, which roughly corresponds to the width of the measured CPT.

5.4 DNP near the CPT resonance

However, $P(\delta)$ can undergo changes when the electron spin is brought out of thermal equilibrium by optical orientation. An optically-induced electron spin polarization will in turn induce nuclear spin polarization via a hyperfine-mediated cross-relaxation process known as DNP. In Ref. [22] it was described how the interplay between the laser-induced electron spin polarization near CPT resonance and DNP can change the shape of $P(\delta)$ by autonomous feedback control, leading to the formation of stable states for the nuclear spin polarization and offering the potential of reducing the variance σ_δ^2 . The essence of this method is pictured schematically in Fig. 5.1(c). It shows two distinct control regimes (color coded, red and blue) where both lasers are either red ($\Delta < 0$) or blue ($\Delta > 0$) detuned from the excited state. The change in laser coupling strength with δ is asymmetric when $\Delta \neq 0$ (one laser approaches resonance while the other moves away from it). For a single system with a particular Overhauser shift this causes a sharp change in the optically-induced electron spin polarization $\langle S_z \rangle - \langle \bar{S}_z \rangle$ (where the overbar implies that the expectation value is taken at thermal equilibrium), shown in the middle panels as a function of δ (the Overhauser shift is here normalized to Γ_3). The blue and red dots indicate stable points, where $\langle S_z \rangle = \langle \bar{S}_z \rangle$ and $\partial/\partial\delta(\langle S_z \rangle - \langle \bar{S}_z \rangle) < 0$. We thus expect $P(\delta)$ to evolve from the initial Gaussian to either a

distribution with two maxima, or to a distribution with one maximum. Such steady-state distributions are non-thermal and can thus have reduced fluctuations if the system's feedback response (slope of $\langle S_z \rangle - \langle \bar{S}_z \rangle$ near the stable point) is strong enough [22].

5.5 Observation of one and two stable states

We investigate this interplay between CPT and DNP for the donor-bound electrons in GaAs by monitoring the changes in the CPT lineshape induced by two-laser optical pumping, with both lasers at equal intensity near two-photon resonance. Figures 5.2(a,b) show the CPT lineshape before (gray lines) and after 10 min of optical pumping with blue- and red-detuned lasers. While scanning over the ensemble CPT peak, the probe laser meets exact two-photon resonances (near-ideal CPT peaks) of individual electrons for a range of δ -values. The susceptibility is thus proportional to the number of electron spins experiencing a particular Overhauser shift δ , hence reflecting the underlying nuclear spin distribution. The nuclear spin distribution stabilizes as predicted in both cases, observed as a non-shifted single CPT peak in Fig. 5.2(a) and a non-shifted split CPT peak in Fig. 5.2(b) (the splitting directly reflects the doubly peaked $P(\delta)$ of Fig. 5.1(c)). This is in clear contrast with a CPT peak recorded after 10 min of single-laser optical pumping (inset Fig. 5.2(a)), which shifts the CPT peak by ~ 400 MHz since DNP gives here a net nuclear spin polarization.

The lineshape in the main panel of Fig. 5.2(a) remains similar, while a narrower and higher CPT peak is expected if the width of the stabilized $P(\delta)$ would indeed be reduced. In Ref. [22] it was pointed out that for an open system the narrowing by the feedback mechanism is in competition with nuclear spin diffusion. For donors in GaAs this plays a stronger role than for quantum dots, where a material barrier surrounding the dot suppresses this spin diffusion. Not observing a narrowing of the CPT peak is also due to non-uniform laser intensities for the electron ensemble (further discussed below).

Figure 5.2(c) shows the transition from red- to blue-detuned two-laser pumping, for a range of detunings Δ . Splittings in these CPT peaks are

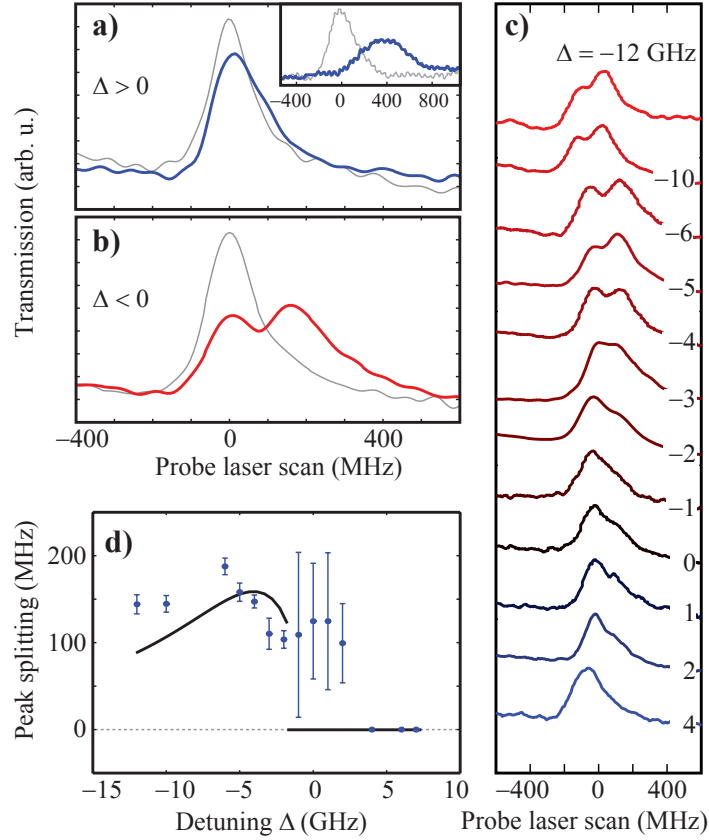


Figure 5.2: CPT signatures of DNP feedback. (a) The CPT peak in the transmission signal as a function of probe laser frequency, before (gray) and after (blue) a DNP pumping period with two lasers fixed on two-photon resonance (Fig. 1(c)) and detuning $\Delta = +4$ GHz. The inset shows how DNP pumping by one laser (on the $|\uparrow\rangle - |D^0X\rangle$ transition) causes a shift of the CPT resonance. Two-laser pumping stabilizes the nuclear spin polarization at its thermal equilibrium value (here without observing a significant narrowing). (b) Results obtained as for panel (a), but with $\Delta = -6$ GHz. In this case the CPT peak after DNP pumping (red) shows a splitting. (c) CPT traces taken after DNP pumping, for various values of Δ . (d) Values of the peak splitting, obtained from traces as in panel (c). All data was taken with both laser intensities stabilized at values of about 3 Wcm^{-2} (for DNP pumping and CPT probing). Black line: simulation with parameters as in Ref. [22], except $\Gamma_d/\bar{\Gamma}_h = 4000$ and $\gamma_3 = 20$ GHz.

analyzed in Fig. 5.2(d), obtained by fitting two Gaussians to each CPT peak. Where the fit does not improve with respect to a single-Gaussian fit we take the splitting to be zero. The data reproduces the essential features of the model [22] (black line), showing a discontinuous transition and a maximum splitting when the pump lasers are tuned to slope of the transition line at $\Delta \approx -5$ GHz, where the response to a shift of δ is largest. We analyzed that this transition is a unique feature that confirms the dominance of the electron spin for the relevant DNP mechanism [22]. For $\Delta \gtrsim 0$ there is no good match, but the fitting also yields larger error bars. We attribute this to inhomogeneous broadening in the optical transitions (effective spread in detunings Δ) which prevents all systems from making the transition simultaneously.

5.6 Laser power and frequency dependence of the CPT splitting

We now focus on the control regime $\Delta < 0$ to examine the dependence of the stabilization on the control parameters during the optical pumping phase. Figure 5.3(a) shows the importance of carefully tuning the relative frequencies for getting a balanced distribution. A detuning as small as 31 MHz for one of the lasers gives a significant shift within $P(\delta)$ to either one of the stable states. Figure 5.3(b) shows values for the splitting as a function of the laser powers (varied simultaneously). The splitting shows a discontinuous onset and subsequent increase due to power broadening of the CPT peak. The data qualitatively matches the prediction ([22], black line) but the slope is lower than the simulation. We attribute this to standing wave patterns in the GaAs layer (which acts as a weak cavity). The patterns for the two lasers do not fully overlap since they differ in frequency. This prohibits addressing the entire ensemble with equal laser intensities, and gives for the ensemble an averaged, less effective feedback mechanism. This also provides a limitation for the amount of CPT-peak narrowing in the blue-detuned case. The narrowing effect relies on carefully balanced laser intensities, and this is compromised due to the intensity variation inside the sample. Studying the achievable narrowing of $P(\delta)$ requires an experiment with uniform intensities for the ensemble.

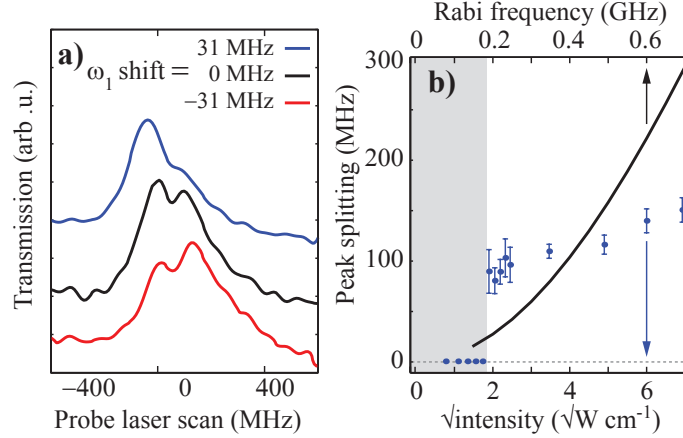


Figure 5.3: (a) CPT traces after DNP pumping with two lasers at $\Delta \approx -3.5$ GHz. The trace labeled $\omega_1 = 0$ MHz is taken after pumping on exact two-photon resonance. The blue (red) trace is measured after pumping with $\omega_1 = +(-)31$ MHz detuned from exact two-photon resonance (see Fig. 1(c)). (b) The peak splitting in CPT traces after pumping with $\Delta \approx -4$ GHz and exact two-photon resonance, as a function of the intensity of the two lasers (keeping the intensity ratio fixed near 1). The gray background shows the range where the CPT peak shape was analyzed as a single peak. Significant double-peak character was observed for the total laser intensity above $\sim 3 \text{ Wcm}^{-2}$. CPT traces were all taken with both lasers intensities at $\sim 3 \text{ Wcm}^{-2}$. Black line: simulation with same parameters as in Fig. 5.2, the top axis shows the Rabi frequency corresponding to the simulation [22].

5.7 Time-dependent measurements

Figure 5.4 presents time evolution of the effects. Figure 5.4(a) shows build-up of the splitting, obtained by taking CPT traces during the optical pumping phase every 30 s (each trace is collected within 1 s). The splitting stabilizes after approximately 4 min. Figure 5.4(b) shows decay of the splitting. It consists of traces collected after the optical pumping phase. After 10 min of optical pumping (repeated before each trace) the system is kept in the dark for a time ranging from 1 to 10 s. The splitting fades away in seconds, consistent with the relaxation of the lattice nuclear

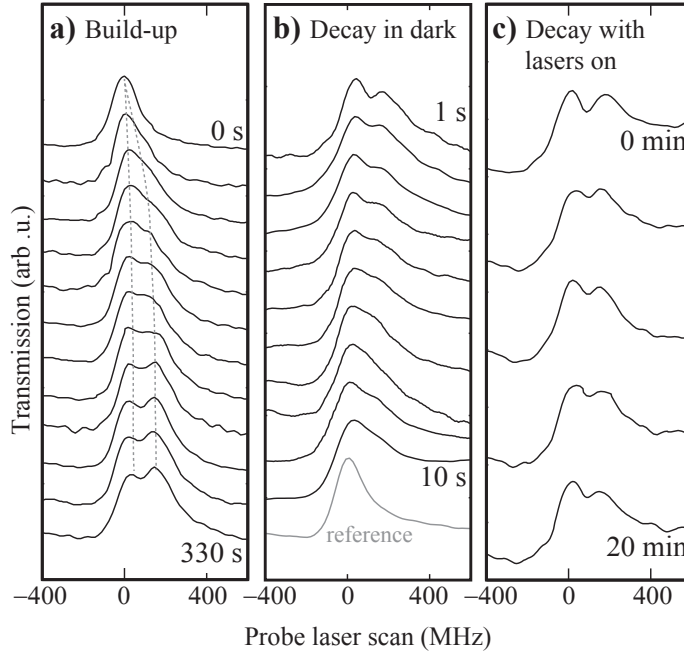


Figure 5.4: Time evolution of build-up (a) and decay (b,c) of stabilized nuclear spin ensembles, measured during and after the DNP pumping period (subsequent traces top to bottom, as labeled). Panel (b) gives a reference for the CPT peak before pumping. The data in (a) is obtained from CPT scans of 1 s in between periods of 30 s DNP pumping with two lasers fixed at two-photon resonance ($\Delta = -4$ GHz). Panel (b) presents CPT scans of 1 s, taken after a fully dark period of 1 s (top trace) to 10 s (bottom trace) after DNP pumping ($\Delta = -4$ GHz). The results in (c) are from continuously taking CPT scans of 1 s (only four traces shown), after a DNP pumping period at $\Delta = -2$ GHz. All data was taken with both laser intensities stabilized at values of about 3 Wcm^{-2} (for DNP pumping and CPT probing).

spins by spin diffusion away from the electron [28]. However, when CPT scans are taken continuously after the optical pumping phase the splitting decays much slower and persists up to at least 20 min (Fig. 5.4(c), we verified that taking such scans without the preceding pumping phase does not induce a splitting). We attribute this to a suppression of the spin diffusion while the system is illuminated: under optical excitation (during CPT scans) the electron spin is most of the time significantly polarized and

this suppresses nuclear spin diffusion because it creates an inhomogeneous Knight field for the surrounding nuclear spins [29, 30]. This effect could be used to improve the strength of the feedback control and the amount of narrowing: if the temperature of the experiment would be lower or the magnetic field stronger (increased $\langle \overline{S}_z \rangle$) the thermal-equilibrium electron spin polarization can suppress nuclear spin diffusion.

5.8 Conclusion

Our results open the possibility to use the interplay between CPT and DNP to operate a mesoscopic spin system as a feedback loop that converges towards a well defined steady state, determined by laser power and detuning, with the possibility of reduced nuclear spin fluctuations and less electron spin dephasing. The mechanism is generally applicable to localized spins where DNP is dominated by electron-nuclear spin hyperfine coupling and can also be used for other paramagnetic defects, as ensembles or single systems. A notable example is the fluorine donor in ZnSe [31, 32], a II-VI material with dilute nuclear spins (in GaAs all atoms have non-zero nuclear spin). Nuclear spin diffusion, mediated by dipole-dipole interaction (inversely proportional to distance between nuclear spins to the power 6), will here be much less a limitation for narrowing.

References

- [1] Dyakonov, M. I. & Perel, V. I. Optical orientation in a system of electrons and lattice nuclei in semiconductors-theory. *Zh. Eksp. Teor. Fiz.* **65**, 362–375 (1973).
- [2] Khaetskii, A. V., Loss, D. & Glazman, L. Electron spin decoherence in quantum dots due to interaction with nuclei. *Phys. Rev. Lett.* **88**, 186802 (2002).
- [3] Merkulov, I. A., Efros, A. L. & Rosen, M. Electron spin relaxation by nuclei in semiconductor quantum dots. *Phys. Rev. B* **65**, 205309 (2002).
- [4] Coish, W. A. & Loss, D. Hyperfine interaction in a quantum dot: Non-markovian electron spin dynamics. *Phys. Rev. B* **70**, 195340 (2004).
- [5] Danon, J. & Nazarov, Y. V. Nuclear tuning and detuning of the electron spin resonance in a quantum dot: Theoretical consideration. *Phys. Rev. Lett.* **100**, 056603 (2008).

-
- [6] Klauser, D., Coish, W. A. & Loss, D. Nuclear spin state narrowing via gate-controlled rabi oscillations in a double quantum dot. *Phys. Rev. B* **73**, 205302 (2006).
- [7] Giedke, G., Taylor, J. M., D'Alessandro, D., Lukin, M. D. & Imamoglu, A. Quantum measurement of a mesoscopic spin ensemble. *Phys. Rev. A* **74**, 032316 (2006).
- [8] Stepanenko, D., Burkard, G., Giedke, G. & Imamoglu, A. Enhancement of electron spin coherence by optical preparation of nuclear spins. *Phys. Rev. Lett.* **96**, 136401 (2006).
- [9] Issler, M. *et al.* Nuclear spin cooling using overhauser-field selective coherent population trapping. *Phys. Rev. Lett.* **105**, 267202 (2010).
- [10] Korenev, V. L. Multiple stable states of a periodically driven electron spin in a quantum dot using circularly polarized light. *Phys. Rev. B* **83**, 235429 (2011).
- [11] Shi, X.-F. Nuclear spin polarization in a single quantum dot pumped by two laser beams. *Phys. Rev. B* **87**, 195318 (2013).
- [12] Reilly, D. J. *et al.* Suppressing spin qubit dephasing by nuclear state preparation. *Science* **321**, 817–821 (2008).
- [13] Vink, I. T. *et al.* Locking electron spins into magnetic resonance by electron-nuclear feedback. *Nat Phys* **5**, 764–768 (2009).
- [14] Latta, C. *et al.* Confluence of resonant laser excitation and bidirectional quantum-dot nuclear-spin polarization. *Nature Physics* **5**, 758–763 (2009).
- [15] Xu, X. *et al.* Optically controlled locking of the nuclear field via coherent dark-state spectroscopy. *Nature* **459**, 1105–1109 (2009).
- [16] Bluhm, H., Foletti, S., Mahalu, D., Umansky, V. & Yacoby, A. Enhancing the coherence of a spin qubit by operating it as a feedback loop that controls its nuclear spin bath. *Phys. Rev. Lett.* **105**, 216803 (2010).
- [17] Ladd, T. D. *et al.* Pulsed nuclear pumping and spin diffusion in a single charged quantum dot. *Phys. Rev. Lett.* **105**, 107401 (2010).
- [18] Hansom, J. *et al.* Environment-assisted quantum control of a solid-state spin via coherent dark states. *Nature Physics* (2014).
- [19] Togan, E., Chu, Y., Imamoglu, A. & Lukin, M. Laser cooling and real-time measurement of the nuclear spin environment of a solid-state qubit. *Nature* **478**, 497–501 (2011).
- [20] Greilich, A. *et al.* Nuclei-induced frequency focusing of electron spin coherence. *Science* **317**, 1896–1899 (2007).
- [21] Carter, S. G. *et al.* Directing nuclear spin flips in inas quantum dots using detuned optical pulse trains. *Phys. Rev. Lett.* **102**, 167403 (2009).
- [22] Onur, A. R. & van der Wal, C. H. Two-laser dynamic nuclear polarization with semiconductor electrons: feedback, suppressed fluctuations, and bistabil-

- ity near two-photon resonance. *arXiv preprint arXiv:1409.7576* (2014). URL <http://arxiv.org/abs/1409.7576>.
- [23] Sladkov, M. *et al.* Polarization-preserving confocal microscope for optical experiments in a dilution refrigerator with high magnetic field. *Review of Scientific Instruments* **82**, – (2011).
- [24] Sladkov, M. *et al.* Electromagnetically induced transparency with an ensemble of donor-bound electron spins in a semiconductor. *Phys. Rev. B* **82**, 121308 (2010).
- [25] Fleischhauer, M., Imamoglu, A. & Marangos, J. P. Electromagnetically induced transparency: Optics in coherent media. *Rev. Mod. Phys.* **77**, 633–673 (2005).
- [26] Clark, S. M. *et al.* Ultrafast optical spin echo for electron spins in semiconductors. *Phys. Rev. Lett.* **102**, 247601 (2009).
- [27] Paget, D., Lampel, G., Sapoval, B. & Safarov, V. I. Low field electron-nuclear spin coupling in gallium arsenide under optical pumping conditions. *Phys. Rev. B* **15**, 5780–5796 (1977).
- [28] Paget, D. Optical detection of NMR in high-purity GaAs: Direct study of the relaxation of nuclei close to shallow donors. *Phys. Rev. B* **25**, 4444–4451 (1982).
- [29] Deng, C. & Hu, X. Nuclear spin diffusion in quantum dots: Effects of inhomogeneous hyperfine interaction. *Phys. Rev. B* **72**, 165333 (2005).
- [30] Gong, Z.-X., Yin, Z.-Q. & Duan, L.-M. Dynamics of the overhauser field under nuclear spin diffusion in a quantum dot. *New Journal of Physics* **13**, 033036 (2011).
- [31] Greilich, A. *et al.* Spin dephasing of fluorine-bound electrons in ZnSe. *Phys. Rev. B* **85**, 121303 (2012).
- [32] Kim, Y. *et al.* Optically controlled initialization and read-out of an electron spin bound to a fluorine donor in ZnSe. *Current Applied Physics* **14**, 1234 – 1239 (2014).

Chapter 6

Optically induced dynamic nuclear spin polarization in n-GaAs mediated by shallow donor electrons

Abstract

We show results on accurate control of optically induced dynamic nuclear polarization in n-GaAs using a technique that utilizes electromagnetically induced transparency as a probe for the local effective magnetic (Overhauser) field at shallow silicon donors in gallium arsenide. We find that the sign of nuclear polarization can be controlled by optical pumping of distinct energy levels, of free excitons and excitons bound to silicon donors, such that Overhauser fields of up to 200 mT either along or opposite to an external magnetic field can be built up. Our results directly probe and confirm the prominent role for shallow donors in various schemes for optically induced dynamic nuclear polarization, and can be applied for patterning micronscale magnetic structures in semiconductors with up and down polarities.

This chapter is based on reference 8 on page 151

6.1 Introduction

Magnetic nanostructures are of importance for spintronics applications, which require control of electron spins with magnetic and electric fields on small length scales. In semiconductors such as gallium arsenide, the disordered nuclear spins generally disturb electron spin coherence via the hyperfine interaction. However, this hyperfine coupling can be utilized to transfer electron spin polarization to the nuclei by a cross-relaxation process known as dynamic nuclear polarization (DNP). This can be used to create an effective magnetic (Overhauser) field in the material and various techniques have been proposed to pattern these internal magnetic fields on the micrometer scale [1, 2].

Several decades ago it was already realized that localized electrons bound to donor atoms form paramagnetic impurities that are important in the transfer process of DNP [3]. More recently, localized electron spins have emerged as candidates for information storage in solid state systems for spintronics and quantum information applications [4]. Therefore, a good understanding of electron and nuclear spin dynamics at these impurity sites is important. This can be achieved by monitoring the subpopulation of nuclear spins which is in contact with donor-bound electrons. Generally this is a very small percentage of the total number of nuclei and therefore hard to study directly by nuclear magnetic resonance. Our approach is an all-optical scheme, comprised of optically induced dynamic nuclear polarization, and optical monitoring of this polarization via the electromagnetically induced transparency (EIT) resonance. We show here that this method gives an accurate measurement of the nuclear spin polarization around donors and thereby sheds light on the mechanisms that govern spin coherence of the donor-bound electron. Our results directly probe and confirm the prominent role for shallow donors in various schemes for optically induced dynamic nuclear polarization.

Contrary to the conventional way of creating an out of equilibrium spin polarization by exciting spin-polarized conduction electrons, we use continuous-wave lasers to resonantly excite specific energy levels of the bound exciton or free exciton and observe the nuclear polarization that builds up in the cross-relaxation process. We find that we can controllably

create nuclear polarizations corresponding to effective magnetic (Overhauser) fields of a few hundred millitesla either directed along or opposite to the external field. The work gives insight in nuclear spin dynamics that is relevant for accurate control of impurity spins. Furthermore, the demonstration of negative and positive Overhauser field creation at well defined sites creates the interesting prospect of patterning small scale magnetic structures in semiconductors by controlled doping and optical pumping.

6.2 X and D⁰X magnetospectroscopy

Measurements are performed on a film of gallium arsenide (GaAs) doped with silicon (Si) donors at a concentration of $3 \times 10^{13} \text{ cm}^{-3}$, which is well below the metal-insulator transition around $3 \times 10^{16} \text{ cm}^{-3}$. The wafer is cleaved in 2-by-2 mm² parts along the $\langle 110 \rangle$ crystallographic axes. The epitaxially grown film is lifted off of its GaAs substrate by removing an AlAs buffer layer with a hydrofluoric acid wet etch. After lift-off the film is transferred to a sapphire substrate, which allows us to do transmission measurements in an experimental setup that has been described in detail elsewhere [5]. In summary, measurements are performed in a bath cryostat where the sample is kept at a temperature of 4.2 K inside the coil of a superconducting magnet that generates a magnetic field of 6.4 T at the sample position. The sample is mounted such that the magnetic field direction is along the $\langle 110 \rangle$ crystallographic axis. Under these conditions the donor electrons stay bound to the Si atoms by the Coulomb force, in a state that is below the conduction band edge by the binding energy of 6 meV. Because of the low doping density these electrons are well isolated from each other and form an ensemble of localized electrons, which are trapped by the spherically symmetric potential provided by the donor ion core.

Spectroscopy results on the sample are displayed in Fig. 6.1. The upper panel of Fig. 6.1a shows the single laser transmission spectrum without application of an external magnetic field and the lower panel shows this spectrum when a magnetic field of 6.4 T is applied. Besides absorption lines, both these spectra show chirped periodic modulation that is due to a Fabry-Perot effect inside the GaAs film, which acts as a

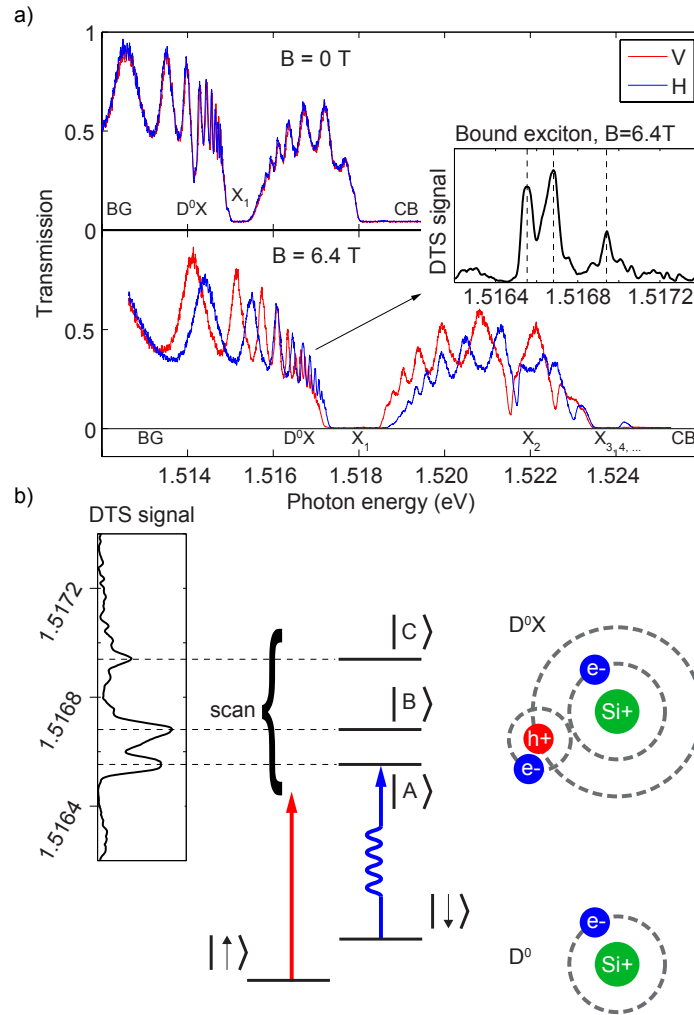


Figure 6.1: (a) The transmission spectrum at $T = 4.2$ K of the $10\ \mu\text{m}$ GaAs film showing the free- (X_1 , X_2 , etc.) and bound-exciton (D^0X) absorption lines near the band edge. At finite magnetic field the levels spread out (lower panel), rendering the donor-bound exciton levels practically invisible. The inset shows the position of D^0X levels obtained by pump-assisted spectroscopy (providing a differential transmission signal, DTS). Labels BG and CB indicate band gap and conduction band regions. (b) One configuration used for differential transmission spectroscopy (see also main text): The modulated probe is at resonance with $|\downarrow\rangle \rightarrow |A\rangle$ transition, while another laser scans over the range with transition to the D^0X levels $|A\rangle$, $|B\rangle$, $|C\rangle$, etc.

weak cavity. Polariton formation causes the chirping (change in period) of the modulation around the free exciton resonance [6]. The laser beam passes through the sample in Voigt geometry, where the light propagation direction is perpendicular to the magnetic field. The light is guided to the sample space by a polarization-maintaining optical fiber which supports two orthogonal linear polarization directions. We distinguish horizontally (H-)polarized light (blue line in Fig. 6.1a) and vertically (V-)polarized light (red line in Fig. 6.1a), where vertical implies linear polarization parallel to the applied magnetic field. H-polarized light induces σ -transitions which change the electronic angular momentum by \hbar , V-polarized light induces π -transitions which conserve electronic angular momentum [6].

Without magnetic field the donor-bound exciton resonance is visible (labeled as D^0X), with an additional binding energy of 0.6 meV with respect to the prominent $n = 1$ free exciton resonance (labeled as X_1). The free exciton lines of higher principal quantum number n blend in with the continuum of states (conduction band, CB) above the band edge. The fact that the spectra for H- and V-polarized light fall on top of each other in zero field indicates that the GaAs film on sapphire is negligibly strained. In a magnetic field the D^0X transitions cannot be resolved in the single laser spectrum because of population depletion by optical pumping. To overcome this effect we introduce a second laser that takes care of population re-pumping according to the method described in Fig. 6.1b.

An extensive experimental analysis of the D^0X levels in GaAs was also presented by Karasyuk et al. [7], who used photoluminescence detection, which is mostly in accordance with theory [8, 9]. Nevertheless the nature and spectral position of the energy levels at magnetic fields of a few Tesla poses a complex, unsolved, problem. Additionally, they depend on the orientation of the samples crystallographic axes with respect to the magnetic field direction and are sensitive to possible strain in the sample. Therefore, to be able to resonantly address the different bound-exciton levels at a particular magnetic field we perform two-laser differential transmission spectroscopy (DTS) as depicted in Fig. 6.1b. In our approach two lasers co-propagate through a polarization-maintaining fiber to the sample, where they overlap on a spot with a diameter of 10 μm . One of the

laser beams is modulated by a mechanical chopper at a frequency of 6 kHz. The transmitted light of both lasers falls on a Si p-i-n photodiode behind the sample. The modulated part of the photodiode signal is measured by lock-in detection. The modulated laser is held fixed at the position of a known energy level (found by trial-and-error) and another laser is scanned over the wavelength range where the transitions to D^0X levels are. Whenever the scanning laser is resonant with a transition from the other spin state, an increase in absorption is recorded.

There are four variations of this scheme: either placing the fixed laser at a transition for the $|\uparrow\rangle$ or $|\downarrow\rangle$ state, and scanning with each of the two polarizations (H and V). The curve labeled 'DTS signal' is obtained by multiplying a spectrum obtained with the fixed laser on a transition from $|\uparrow\rangle$ and one with the fixed laser on a transition from $|\downarrow\rangle$. This procedure reveals correlations between the spectra, and improves the contrast of absorption lines of transitions to D^0X levels with respect to fluctuating background signals (the method is presented in more detail in [10]). In this way all optically allowed D^0X transitions can be found systematically.

In the graph in Fig. 6.1b three energy levels show up prominently which implies that they have significant optical dipole coupling to both electron spin states, making them suitable for optical orientation of the electron spin. We label them $|A\rangle$, $|B\rangle$ and $|C\rangle$ in order of increasing energy. In the lower panel of Fig. 6.1a, the arrow and inset indicate the position of the D^0X lines in the broader transmission spectrum. The $n = 1$ free exciton appears as one prominent dip, like it did in zero field, even though its eight distinct states [11] have been split by the magnetic field (which can be seen from the broadening of the dip with respect to the zero field spectra). These cannot be resolved due to a combination of small splitting and large oscillator strength. The distinct features that show up around 1.522 eV we can attribute, after following their emergence by taking spectra at slowly increasing magnetic field values, to the $n = 2$ free exciton. They are better resolved than the X_1 states because the larger size of the X_2 wave function results in a larger diamagnetic shift of the levels.

6.3 Measurement of DNP near donors

The nuclear spin bath can be brought out of its equilibrium state by optical pumping of the electron spin [12]. Most commonly this has been achieved by illumination with circularly polarized light in a configuration where the light propagation direction is parallel to the external magnetic field. At a photon energy larger than the band gap (but less than the band gap plus the spin-orbit energy), σ^+ -polarized light polarizes electron spins along the external field while σ^- light polarizes electron spins against the external magnetic field. Spin lattice relaxation of the out of equilibrium electron spins then transfers the excess spin angular momentum to the nuclear spin bath, where it can remain for a very long time (up to hours [3]) because of the weak coupling of the nuclear spins to the environment. Early it became known that paramagnetic centers act as catalysts in this process due to their relatively strong hyperfine fields [3, 13], and thus will act as dominant sources of dynamic nuclear polarization [14]. Even though several studies focussed on the nuclear polarization dynamics around donors [14, 15, 16], it is not easy to single out the role of these impurities sites, for two main reasons: First, at a low D^0 concentration, for example 10^{14} cm^{-3} , the spheres with radius $a_0 \approx 10 \text{ nm}$ around Si donor sites cover only 0.02 % of the number of nuclear spins in the sample. Second, above band gap illumination causes photoexcited electrons to move throughout the whole crystal.

Here we use EIT [6] to measure the precise spin splitting of the bound electrons, which in turn depends on the nuclear polarization. This technique adopts part from the double resonance technique [17] (ENDOR), which measures precise nuclear spin splitting by observing the electronic resonance frequency, and from optically-detected NMR techniques [18], where the sensitivity of optical detection is exploited. For this method we proceed in the same way as for the two-laser transmission spectroscopy, but now we focus on a narrow resonance (EIT peak) inside the overall absorption dip where transmission increases. This effect is due to destructive quantum interference of the transition probabilities for absorption of a probe photon in the presence of a control laser [19]. The control laser thus increases the material's transmittance at the probe photon energy,

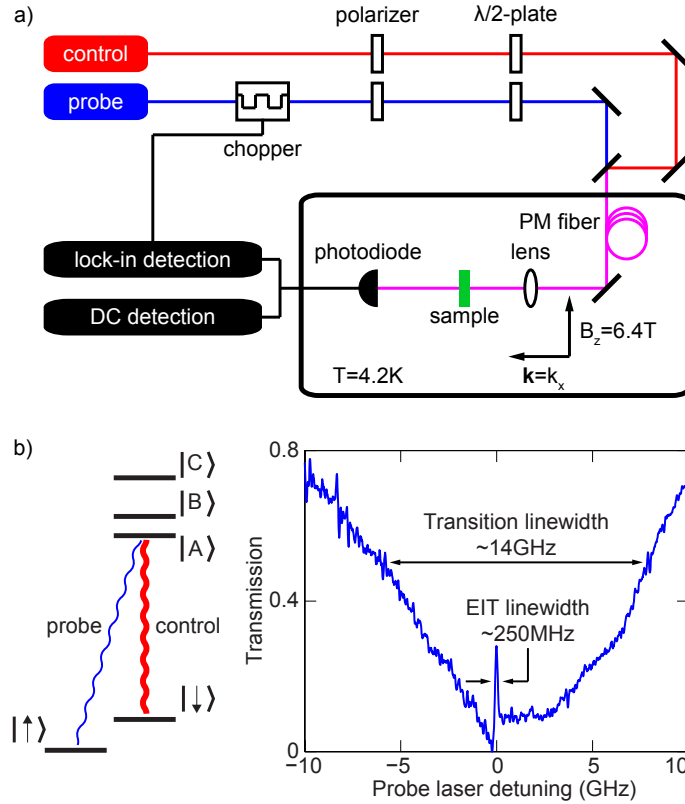


Figure 6.2: (a) Experimental setup for the EIT measurement. Two lasers co-propagate to the sample through a polarization-maintaining single-mode fiber. The probe laser is modulated by a chopper at 6 kHz. The sample is inside a He bath cryostat. A superconducting magnet creates a magnetic field of 6.4 T (Voigt geometry) at the sample position. (b) Both lasers are tuned close to resonance with the $|A\rangle$ level. Scanning the probe laser around this transition results in a broad transmission dip with a narrow two-photon resonance (EIT peak) at its center due to the presence of the control laser.

hence the name electromagnetically induced transparency (EIT) for this phenomenon. Because EIT is a coherent two-photon process the minimal width of the resonance is determined by the electron spin dephasing, in contrast to the overall absorption dip whose width is determined by excited state dephasing. The narrow linewidth of 250 MHz thus approximately corresponds to the 3 ns spin dephasing time estimated in Chapter 3. The electron spin splitting (possibly altered by an Overhauser shift) equals

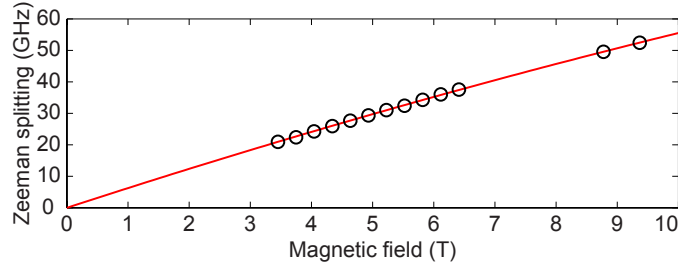


Figure 6.3: Determination of the electron Landé g-factor by measuring the electron spin splitting via the EIT resonance in a range of magnetic fields (using EIT data that is not significantly affected by DNP effects). The red line is a quadratic fit, $\gamma_1 B + \gamma_2 B^2$, to the data points resulting in $\gamma_1 = (6346 \pm 4) \text{ MHz T}^{-1}$, $\gamma_2 = (-796 \pm 5) \times 10^{-1} \text{ MHz T}^{-2}$.

the difference between the control laser photon energy and the probe photon energy at EIT resonance, a quantity which we determine with MHz precision using a wavemeter (Cluster LM-007).

The accuracy of the method is underlined by Fig. 6.3 where it is used to determine value of the Landé g-factor of the bound electrons in this sample. A fit of the observed Zeeman splitting (E_Z) in this figure to the function $\gamma_1 \mu_B B + \gamma_2 B^2$ determines $\gamma_1 = (6346 \pm 4) \text{ MHz T}^{-1}$ and $\gamma_2 = (-796 \pm 5) \times 10^{-1} \text{ MHz T}^{-2}$. The (field-dependent) effective g-factor $g = E_Z / \mu_B B = h / \mu_B \cdot (\gamma_1 + \gamma_2 B)$ can thus be determined with an accuracy of about one part in thousand. This yields $g = -(4534 \pm 3) \times 10^{-4}$ for zero field (minus sign taken from the literature). At a field of $B = 6.4 \text{ T}$, the value $g = -(4170 \pm 6) \times 10^{-4}$, and at 10 T the value $g = -(3965 \pm 7) \times 10^{-4}$.

To measure the effect of the optical pumping on the nuclear spins we carry out the experimental sequence of events as depicted in Fig. 6.4a. First we apply a pump laser at well-defined wavelength for thirty minutes. Immediately after that we switch to the two-laser configuration and take repeated EIT scans to detect any change that the optical pumping has induced in the EIT resonance. A result of a typical measurement sequence is shown in Fig. 6.4a. The pump laser was applied for 30 minutes to the $|\uparrow\rangle$ to $|A\rangle$ transition. The traces in the graph show EIT scans and the color scale represents the time at which the scan is taken, where $t = 0$

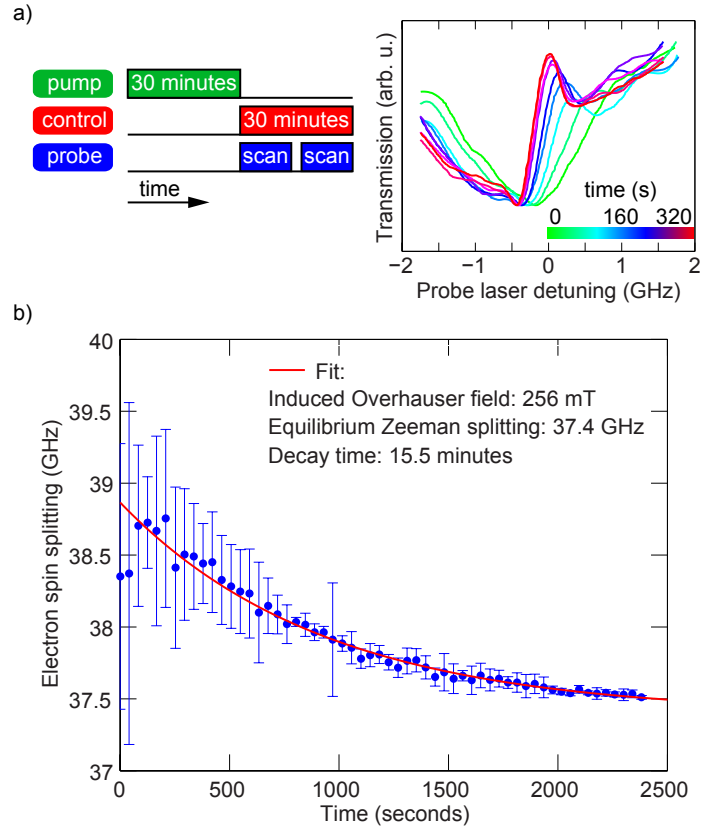


Figure 6.4: (a) Experimental setup and timing sequence for the DNP experiment, see main text for details. Evolution of the EIT profile after pumping shows relaxation of DNP that was built up during the pumping time. Time between traces is 40 seconds. (b) Exponential fit to the measured electron spin splitting, as deduced from the EIT traces in Panel a, as a function of time. The maximum induced Overhauser field is given by the shift of the electron spin splitting at time $t = 0$. The nuclear polarization decay time is defined as the time when the Overhauser field has relaxed to $1/e$ times its maximum value.

is the moment when the pump laser was blocked. The evolution of EIT traces over time depicts the relaxation of a nuclear polarization of 255 mT towards the equilibrium configuration. Figure 6.4b depicts the evolution of the maxima of the EIT resonances from the traces in Fig. 6.4a by the points in blue. The red solid line is an exponential fit to the data from which we extract the maximum induced Overhauser field and the decay

time, which are respectively 255 mT and 15.5 minutes for this particular measurement. The positive sign of the Overhauser field, i.e. increased electron spin splitting, is consistent with the explanation where the electron spin is oriented towards the $|\downarrow\rangle$ state during the pumping phase. Another important feature that deserves attention is that a broadening of the resonance comes together with the shift. This is reflected in the large error bars on the measurement points for the out-of-equilibrium nuclear polarization in Fig. 6.4b. This points to increased inhomogeneity of the nuclear spin polarization over the D^0 ensemble. We attribute this to the inhomogeneous intensity of the pump laser beam, due to the Gaussian spot and the formation of a standing wave pattern inside the sample which acts as a planar cavity

6.4 Spectral dependence of DNP

Using continuous wave lasers we can accurately select the excitation wavelength for the optical pumping. We use this to investigate the build up and relaxation of DNP induced by pumping at the bound- and free exciton resonances near the band edge. Figure 6.5 shows the result for the transitions to the bound-exciton levels. The upper panel shows the complete result of the differential transmission spectroscopy on D^0X , using all four combinations possible with the available light polarizations. These spectra are labeled in the legend according to $H/V \times H/V$ which has the meaning that a particular curve, say $H \times V$, is the result of the multiplication of the spectrum obtained from scanning with H-polarization while locking a laser to a transition from $|\downarrow\rangle$ and the spectrum obtained from scanning with V-polarization while locking a laser to a transition from $|\uparrow\rangle$. We thus find 3 levels that couple to both ground states, labeled A, B, C as in Fig. 6.1. From comparing the different types of spectra the polarization selectivity is derived. The pump photon energy on the horizontal axis is the energy difference between the $|\uparrow\rangle$ ground state and the optically excited states. These levels can all mediate optical electron spin orientation.

In the lower panel of Fig. 6.5 we examine how these levels mediate the DNP process when a pumping laser is resonant with the particular level from the $|\uparrow\rangle$ state and the induced DNP is subsequently measured as in

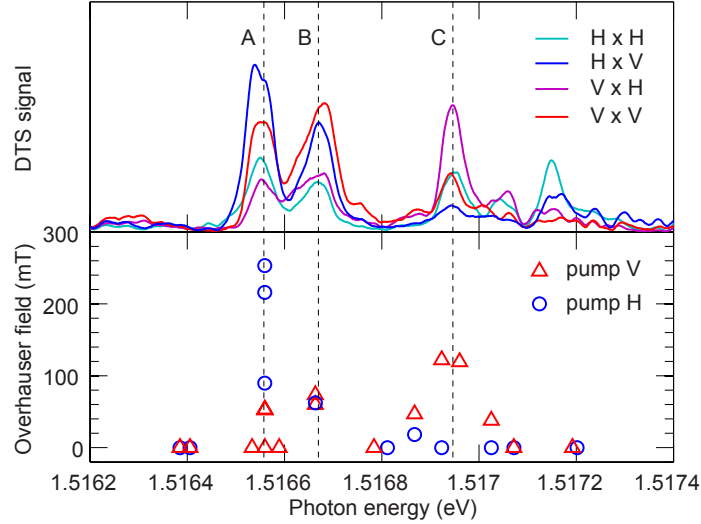


Figure 6.5: Maximum induced Overhauser field as a function of pump photon energy shows the correlation between level positions as found in spectroscopy and DNP pumping. Top panel: spectral position of the D^0X energy levels, as measured from the $|\uparrow\rangle$ ground state found with the method described in Chapter 7. Line coloring distinguishes the polarization dependence of the transitions (also described in Chapter 7). Bottom panel: resulting maximum Overhauser field after pumping for 30 minutes with either V (red triangles) or H (blue circles) polarization.

Fig. 6.4. The photon energy of the pump laser is on the horizontal axis and the maximum Overhauser shift is along the vertical axis. The method used for these measurements is derived from the findings described in Chapter 3. There we found that it is in fact possible to create an opposite Overhauser field using excitation light resonant with transitions from the $|\downarrow\rangle$ state. However because of the asymmetry described in that chapter, higher laser powers are required to accomplish this.

To demonstrate correlation between DNP and resonance excitation we focus on transitions from the $|\uparrow\rangle$ state by tuning the pump-laser power low enough (3 W cm^{-2}) so that unintentional excitation of transitions from the $|\downarrow\rangle$ state does not yield a significant Overhauser shift (on the scale of Fig. 6.4b). This is the reason that only data points of positive Overhauser shift are present in this figure. To confirm that it is the resonant excitation

that leads to DNP we include data points from off-resonance pumping as reference. This indeed does not yield any measurable Overhauser shift (see for example the result for pumping at 1.5164 eV). The data shows a correlation between the level positions and the induced Overhauser shift. Moreover, while the polarization selection rules are not very strict, the Overhauser shift dependence on pump laser polarization still correlates with the polarization selectivity derived from the spectroscopy (Fig. 6.5).

In Fig. 6.6 we extend the study of the spectral dependence of DNP to a larger range covering the complete band edge. Panels a and b show the spectrum (same as in Fig. 6.2) and the induced Overhauser shift after pumping 10 minutes with particular photon energy, analogously to Fig. 6.5. The data points around 1.5167 eV are the same as in Fig. 6.5. We examine the Overhauser shift induced by optical pumping of several free exciton lines in the spectrum. Again data points that show zero Overhauser shift are included for reference. In particular, we note that the excitation of free carriers (with above bandgap illumination at 1.53 eV) using linear polarization in Voigt geometry does not induce any Overhauser shift. Our method thus isolates the DNP effects of below band-edge, resonant excitation. Panel b shows that Overhauser shifts up to 300 mT are induced by excitation of free excitons. The two well-defined resonances of X_2 (the precise quantum states of which we do not know) at 1.523 eV show DNP in opposite directions. Also for X_1 , whose levels are not resolved in our spectroscopy, we find that the direction of the Overhauser field is different for different pump photon energies. We thus find that Overhauser fields of up to 300 mT can be induced in either direction by the relaxation process of free and bound excitons. This could be used to locally create internal magnetic fields in a semiconductor such as GaAs, simply by illuminating with narrow-band light.

To further investigate the nature of DNP build-up by exciton relaxation the decay times for the Overhauser field, corresponding to exponential decay as outlined in Fig. 6.4, are shown in Panel c. The EIT-based method used to investigate DNP is only sensitive to local nuclear polarization around the donors. Hence it is the effect of nuclear spin diffusion carrying non-zero nuclear spin polarization away from the donors that we

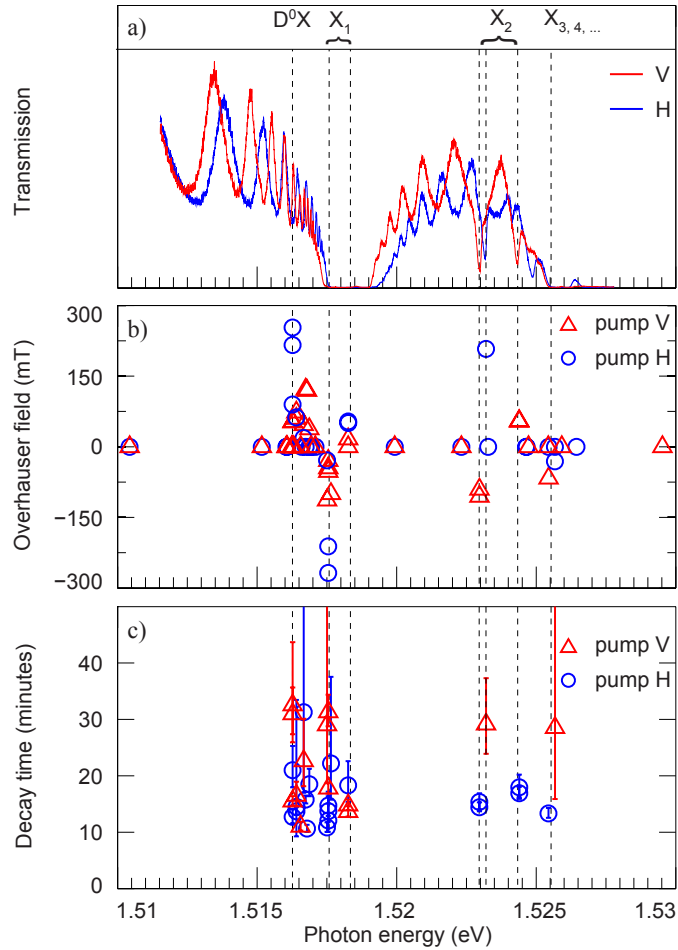


Figure 6.6: (a) Single-laser-scan transmission spectrum at 6.4 T where the labeling indicates position of transition to the bound-exciton states (D^0X) and free-exciton states (X_n) with principle quantum number n . (b) Maximum induced Overhauser field as a function of pump photon energy. These results shows that free exciton pumping generally also results in an induced nuclear polarization around the D^0 systems. This free exciton DNP pumping shows a very sensitive dependence on the pump-photon energy, where small spectral shifts within the free exciton spectral lines (which contains fine-structure features [11]) lead to strong variation of the sign and magnitude of the induced Overhauser field. (c) Decay times corresponding to all nonzero data points from Panel b. The average decay time measured after free-exciton pumping is 19 ± 7 minutes, the average decay time measured after bound-exciton pumping is 18 ± 8 minutes.

measure as an effective decay mechanism [14]. We observe no distinction in the decay time between DNP decay after free- and bound-exciton optical pumping within the error margin: Averaging the respective data points we obtain decay times of $\tau_X = (19 \pm 7)$ min and $\tau_{D^0X} = (18 \pm 8)$ min. These decay times are consistent with the hypothesis that in both cases the observed decay takes place by spin diffusion away from the donor sites, indicating that in both situations DNP is built up locally, at the donor site. We attribute the large error bar on the final averaged value to the fact that there are memory effects in the sample that can influence subsequent measurements: Nuclear spin polarization that has diffused from the donor site can remain in the sample for hours. The presence of this bulk nuclear polarization can influence spin diffusion (and hence perceived decay time) in subsequent measurements, yielding a spread in results measured on the same day. To remedy this one could bring the external magnetic field down to zero between measurements, which allows the nuclei to depolarize quickly. Our results are consistent with DNP being mediated by the strong hyperfine interaction of the donor-bound electrons, which during optical pumping become polarized by either of two ways: By optical excitation in the Λ -system formed of localized states (Fig. 6.1), or via capture of an exciton by a defect [20, 21] and subsequent decay to either of the bound-electron spin ground states.

6.5 Conclusions

We have demonstrated the use of electromagnetically induced transparency to monitor the dynamics of nuclear spin polarization around GaAs D^0 systems. We find that a nuclear spin polarization of up to 300 mT (corresponding to 5% of nuclear spin polarization) can be built up at the GaAs donor sites by illumination with linearly polarized light. Combined with a detailed spectroscopic study of the GaAs band edge, we mapped out the dependence of DNP on specific excitation of bound- and free-exciton states, and polarization of the light. We observed that resonant addressing of specific free- and bound-exciton states leads to a nuclear polarization that is controllably either positive or negative. This is in accordance with a hyperfine mediated interaction between electron spin polarization and

the nuclear spin bath. Controlling the local magnetic field in semiconductors can prove valuable for the development spintronic and optoelectronic device structures.

References

- [1] Kawakami, R. K. *et al.* Ferromagnetic imprinting of nuclear spins in semiconductors. *Science* **294**, 131–134 (2001).
- [2] King, J. P., Li, Y., Meriles, C. A. & Reimer, J. A. Optically rewritable patterns of nuclear magnetization in gallium arsenide. *Nature Communications* **3**, 918 (2012).
- [3] Bloembergen, N. On the interaction of nuclear spins in a crystalline lattice. *Physica* **15**, 386 – 426 (1949).
- [4] Awschalom, D. D., Bassett, L. C., Dzurak, A. S., Hu, E. L. & Petta, J. R. Quantum spintronics: Engineering and manipulating atom-like spins in semiconductors. *Science* **339**, 1174–1179 (2013).
- [5] Sladkov, M. *et al.* Polarization-preserving confocal microscope for optical experiments in a dilution refrigerator with high magnetic field. *Review of Scientific Instruments* **82**, 043105 (2011).
- [6] Sladkov, M. *et al.* Electromagnetically induced transparency with an ensemble of donor-bound electron spins in a semiconductor. *Phys. Rev. B* **82**, 121308 (2010).
- [7] Karasyuk, V. A. *et al.* Fourier-transform magnetophotoluminescence spectroscopy of donor-bound excitons in GaAs. *Phys. Rev. B* **49**, 16381–16397 (1994).
- [8] Rühle, W. & Klingenstein, W. Excitons bound to neutral donors in InP. *Phys. Rev. B* **18**, 7011–7021 (1978).
- [9] Rorison, J., Herbert, D. C., Dean, P. J. & Skolnick, M. S. A model for the neutral donor bound exciton system in InP at high magnetic field. *Journal of Physics C: Solid State Physics* **17**, 6435 (1984).
- [10] Chaubal, A. *et al.* High-resolution magneto-optical transmission spectroscopy on the donor bound exciton complex in GaAs (2013). Unpublished manuscript.
- [11] Cho, K., Suga, S., Dreybrodt, W. & Willmann, F. Theory of degenerate $1s$ excitons in zinc-blende-type crystals in a magnetic field: Exchange interaction and cubic anisotropy. *Phys. Rev. B* **11**, 1512–1521 (1975).
- [12] Lampel, G. Nuclear dynamic polarization by optical electronic saturation and optical pumping in semiconductors. *Phys. Rev. Lett.* **20**, 491–493 (1968).
- [13] Bloch, F. Nuclear induction. *Phys. Rev.* **70**, 460–474 (1946).
- [14] Paget, D. Optical detection of NMR in high-purity GaAs: Direct study of the relaxation of nuclei close to shallow donors. *Phys. Rev. B* **25**, 4444–4451 (1982).
- [15] Huang, J. *et al.* Electron-nuclei spin coupling in GaAs—Free versus localized electrons. *Applied Physics Letters* **100**, 132103 (2012).
- [16] Ramaswamy, K., Mui, S. & Hayes, S. E. Light-induced hyperfine ^{69}Ga shifts in semi-insulating GaAs observed by optically polarized NMR. *Phys. Rev. B* **74**, 153201 (2006).

- [17] Feher, G. Electron spin resonance experiments on donors in silicon. I. Electronic structure of donors by the electron nuclear double resonance technique. *Phys. Rev.* **114**, 1219–1244 (1959).
- [18] Manuel, J. & Cohen-Tannoudji, C. Détection optique de la résonance magnétique par modulation de l'effet faraday paramagnétique transversal à la fréquence de Larmor. *C.R. Acad. Sci.* **82**, 413 (1963).
- [19] Arimondo, E. & Orriols, G. Nonabsorbing atomic coherences by coherent two-photon transitions in a three-level optical pumping. *Lettere Al Nuovo Cimento Series 2* **17**, 333–338 (1976).
- [20] Gross, E., Permogorov, S. & Razbirin, B. Free exciton motion in crystals and exciton-phonon interaction. *Journal of Physics and Chemistry of Solids* **27**, 1647 – 1651 (1966).
- [21] Segall, B. & Mahan, G. D. Phonon-assisted recombination of free excitons in compound semiconductors. *Phys. Rev.* **171**, 935–948 (1968).

Chapter 7

Magneto-optics of the bound trion levels

Abstract

We present high-resolution magneto-optical transmission spectroscopy investigations of the trion levels in n-GaAs. Our results reveal the energy levels and the polarization selection rules of the corresponding transitions.

7.1 Introduction

The basic structure of the donor-bound electron and donor-bound exciton have been touched upon in section 2.1. Here we will proceed with a more detailed treatment and examine the energy levels by a spectroscopic study of these bound states. These results serve as a supplement for the earlier chapters because they show that the system we address is not strictly a three level Λ system, but actually consists of more levels. The results can be used to assess the accuracy of the Λ -system model and to judge the goodness of the three-level approximation in various experimental situations.

7.2 Motivation for the study

The structure of the donor bound exciton complex has been a subject of study since first proposed by Lampert [1]. In that work it was already pointed out that the energy levels of the complex can resemble those of the diatomic molecule H_2 . This concept was further developed by Rühle and Klingenstein [2]. They considered the electrons to form a spin singlet with the hole in orbit, the hole angular momentum $J = 3/2$ coupled to the angular momentum of its motion around the impurity site can then explain much of the spectrum. In turn experimental work [3] verified parts of the theory by photoluminescence experiments.

Our intention was to add to this body of work our transmission spectroscopy results on this system. However, after doing a series of measurements presented in this chapter, it was realized that we could not improve on existing literature using this data and an improved approach is needed. Instead we present the results here in support of earlier chapters and focus on the method used to obtain the spectra.

7.3 Complementary spectroscopy

To identify the position of the energy levels of the bound exciton complex we make use of the fact that the differential transmission spectroscopy as presented in Section 8.4 can be performed in four distinct ways, these are

depicted in Fig. 7.1. One laser is fixed at resonance and intensity modulated by a chopper in the beam path, this laser is indicated by the dashed arrow in the figure. For its position, two strong transitions are chosen that can easily be found. The polarization of the fixed laser matches the transition that it is resonant with, as indicated in the figure. In addition to the fixed laser there is a scanning laser, which is not modulated and whose polarization is either H(orizontal) or V(ertical). Alternating between the position of the fixed laser and polarization of the scanning laser gives the four different types. In each case, as the scanning laser moves over a transition a dip will show in the transmission of the fixed laser, this modulated signal is recorded by a lock-in amplifier.

This type of two-laser spectroscopy is needed because the transitions are not resolved in single laser scans due to optical pumping. In Figure 7.2 the single laser spectra are shown at zero magnetic field and in a magnetic field of 6.4 T. At zero magnetic field various D^0X states are indicated by red arrows. In our range of interest we find two of them which are distinguished, according to the model of Ruhle and Klingenstein by the orbital angular momentum of the hole. The inset shows a magnification of that region with the two resonances, here ℓ refers to the hole's orbital motion in the trapping potential.

Out of the four types, the ones that have the fixed laser coupled to a transition from the $|\downarrow\rangle$ state are complementary to the ones where it couples to a transition from $|\uparrow\rangle$. Complementary is meant in the sense that they reveal the same energy levels, the states of the D^0X system, only these will appear at an energy shifted by the electron spin Zeeman energy. We use the correlation between the spectra to identify level positions, as shown in Fig. 7.3.

7.4 Results

The position where resonances (shown as dips in transmission) occur in Fig. 7.3a depicts the distance of the excited state (in frequency units) to $|\downarrow\rangle$. The figure shows the result of the four different types of spectroscopy (labeled T1 to T4) with T3 and T4 shifted by the Zeeman energy so that their resonances overlap with T1 and T2. Because there is some inter-

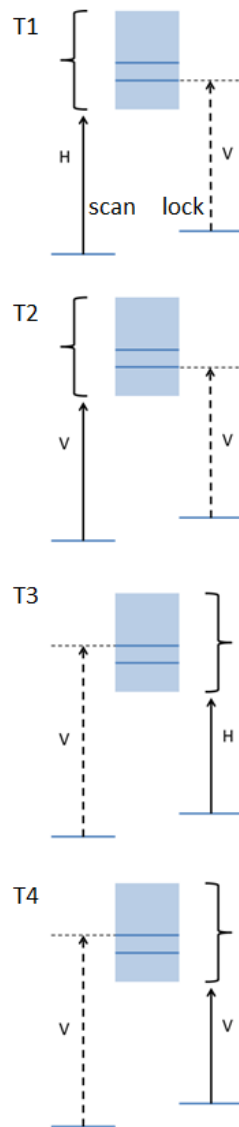


Figure 7.1: Four complementary types of DTS, labeled T1-4. One laser (dashed arrow) is locked at a known transition while the other scans over the D^0X region. Polarizations are H or V as indicated. The laser indicated by a dashed arrow is modulated by a beam chopper. Modulated transmission is recorded via lock-in detection as described in Section 8.4

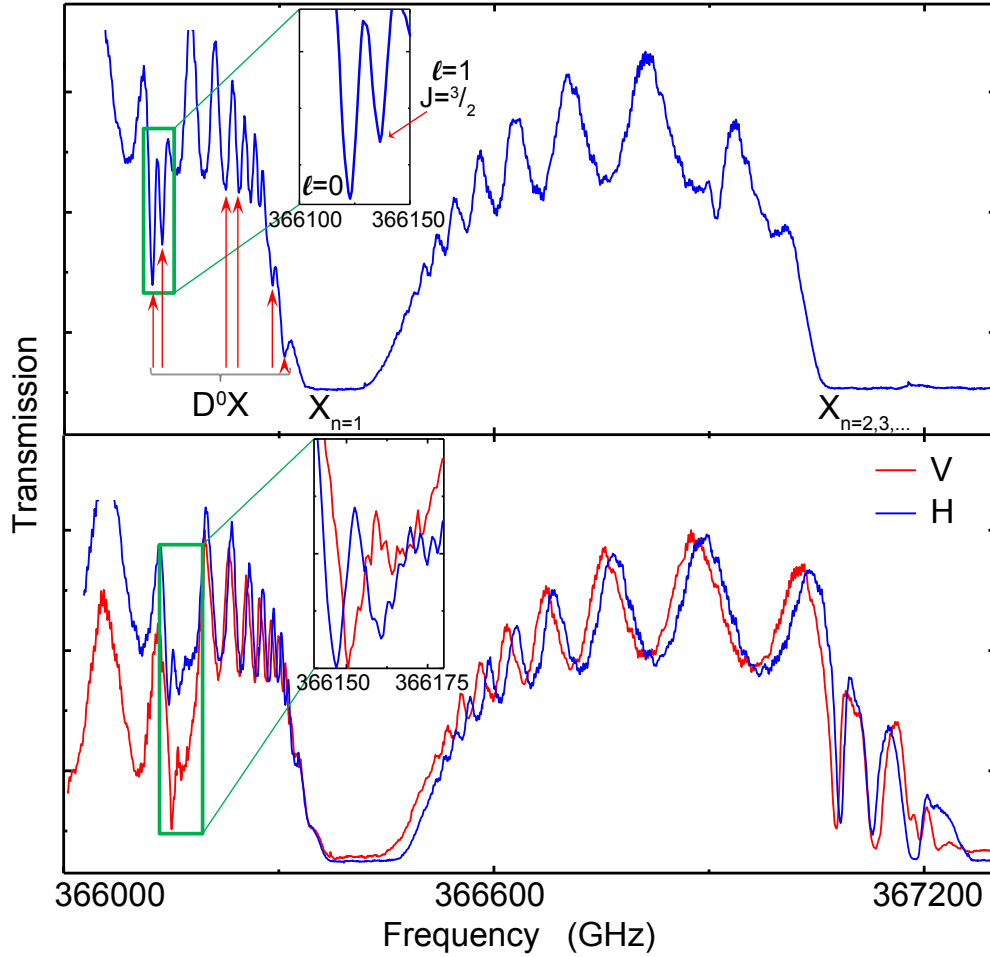


Figure 7.2: Transmission spectrum of the 10 μm thick GaAs film on sapphire. Upper panel: without external magnetic field. Red arrows indicate the positions of D^0X levels (see main text), $X_{n=1,2,\dots}$ are the free exciton resonances and the inset shows the two lowest energy levels of the D^0X complex. Lower panel: with external magnetic field of 6.4 T, the red (blue) line is the spectrum for V (H) polarized light. The inset focusses on the region of the D^0X levels. Individual resonances are not well resolved in the presence of noise and interference effects.

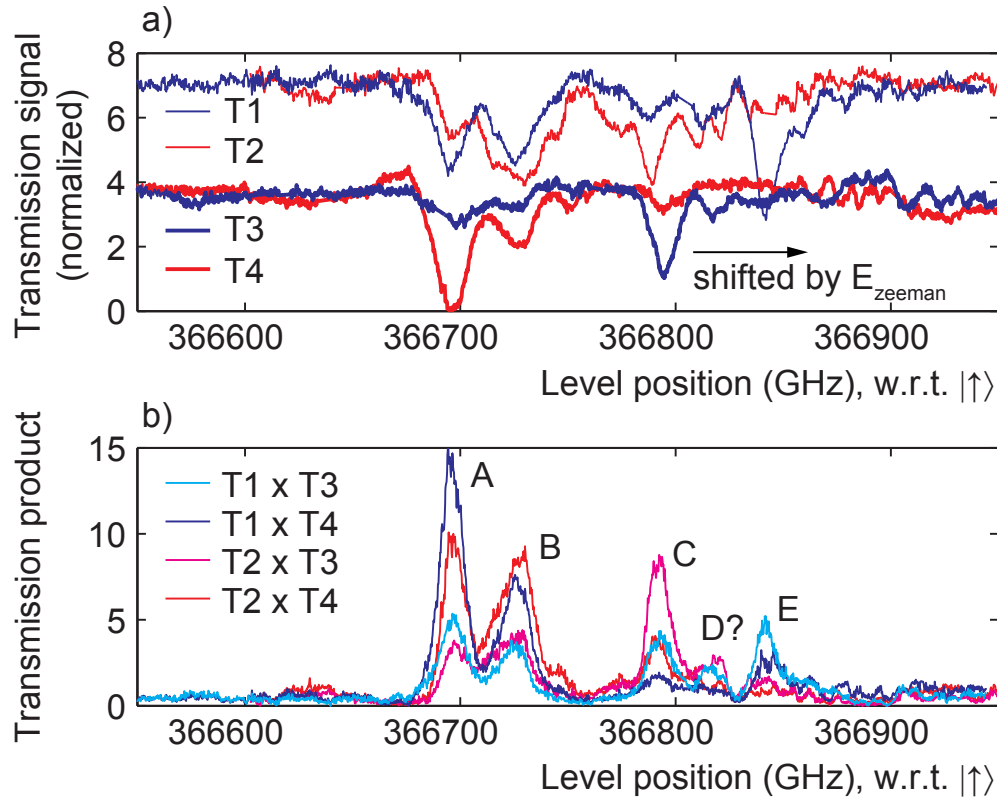


Figure 7.3: Differential transmission spectroscopy (DTS) at magnetic field of 6.4 T, using two lasers in the configurations described in Fig. 7.1. Top panel (scan configurations labeled according to Fig. 7.1), the pair of thick lines (T3, T4) has been shifted by the electron spin Zeeman energy (see Fig. 6.3) such that resonances in the plot occur at the energy of D^0X levels as measured from the ground state ($|\uparrow\rangle$). Lower panel: product of the graphs in the upper panel (as indicated in the legend), baseline subtracted and inverted. Peaks indicate the position of D^0X levels in frequency units, measured from $|\uparrow\rangle$. Relative peak heights of the different colors contain information about the polarization sensitivity of the transition to the particular level (from $|\uparrow\rangle$ as well as $|\downarrow\rangle$, see also main text).

ference on the signal and therefore especially smaller dips are difficult to identify, we look at the correlation between spectra as displayed in Fig. 7.3b. These graphs are obtained by subtracting a baseline from the graphs in Panel a, flipping them, and multiplying them as indicated in the legend. This method gives cleaner data in which resonances are more easily observed. Still by merely looking at the data it can remain unclear as to whether labels such as 'D?' truly indicate a resonance. This issue is resolved by looking at the full magnetospectroscopy result, meaning repetition of the measurement of Fig. 7.3 over a range of magnetic fields. For each magnetic field the correlation method is applied and peak positions and corresponding heights are indicated manually. The resulting graph is displayed in Fig. 7.4 where the colored closed dots are datapoints obtained from the two-laser spectroscopy and the open circles are obtained from single laser spectroscopy (which yields sufficient resolution only at fields up to 2 T). The y-axis of the plot indicates the difference of levels. The size of the closed dots indicates the corresponding peak height. Depending on the threshold set for peak selection (i.e. how high should a peak be as compared to the noise and other fluctuations) more candidates for levels can be found. For example a weak line is visible above the B level, more such lines show up when the threshold is reduced. From the relative heights (or dot sizes) of different colour for a particular resonance, information about the polarization selection rules of the transition can be obtained. For example the level labeled A, which is mostly used for EIT measurements throughout this thesis can be verified to correspond to the $\ell = 0$, $m_j = -1/2$ state. This is understood as the two electrons forming a spin singlet and the hole being in its lowest rotational state with spin down, which corresponds to e.g. the observations of Karasyuk [3] and Fu [4].

7.5 Conclusion

The observations presented in this Chapter are useful to the earlier presented work on the physics in the Λ -system, because it helps to gauge how good the approximation of a Λ -system actually is (whether other levels might be involved or interfering) for a range of magnetic fields. On

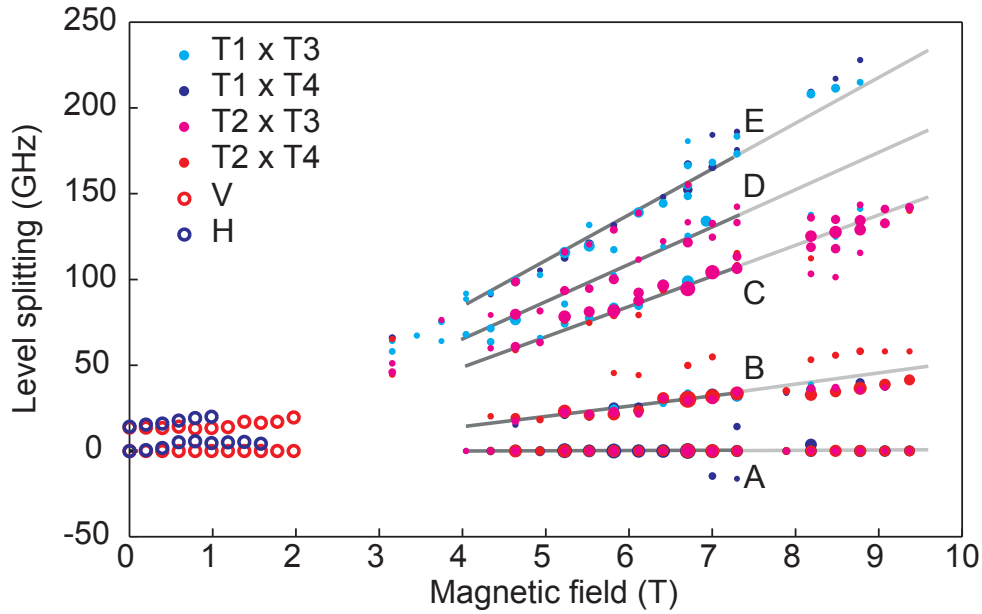


Figure 7.4: Magneto spectroscopy results at low and high magnetic fields combined. D^0X levels are displayed relative to the one with lowest energy (leftmost peak in lower panel of 7.3). The open circles, up to 2 T, are obtained by single laser spectroscopy (SLS) with V (red) or H (blue) polarized light. The two branches originate from the $\ell = 0$ (lower) and $\ell = 1$ (upper) levels indicated in Fig. 7.2. Between 2 T and 4 T the levels are not well resolved in both SLS and DTS. Upwards of 4 T the dots show DTS results (color coding as in legend, cf. 7.3). Between 7.5 T and 8 T there is a gap where the DTS signal becomes too noisy to resolve the levels.

the other hand it proved too difficult to derive the exact nature of the D^0X states based on the data so far collected. The resolution of the spectroscopy method is sufficient but polarization inside the microscope is imperfect, as explained in Chapter 8. Furthermore, extra data should be collected by rotating the sample with respect to the external magnetic field as this changes the observed level structure (this is demonstrated in the experimental work of [3] and the theory of [5]). Finally there is an unidentified feature in the data of Fig. 7.3: The absence of datapoints along a vertical line around 7.5-8 T. Here (and only here) the spectra are

too noisy to observe resonances, meaning the spectroscopy method does not work. The reason for this is not understood so far.

References

- [1] Lampert, M. A. Mobile and immobile effective-mass-particle complexes in non-metallic solids. *Phys. Rev. Lett.* **1**, 450–453 (1958).
- [2] Rühle, W. & Klingenstein, W. Excitons bound to neutral donors in InP. *Phys. Rev. B* **18**, 7011–7021 (1978).
- [3] Karasyuk, V. A. *et al.* Fourier-transform magnetophotoluminescence spectroscopy of donor-bound excitons in GaAs. *Phys. Rev. B* **49**, 16381–16397 (1994).
- [4] Fu, K.-M., Santori, C., Stanley, C., Holland, M. & Yamamoto, Y. Coherent population trapping of electron spins in a high-purity *n*-type GaAs semiconductor. *Phys. Rev. Lett.* **95**, 187405 (2005).
- [5] Cho, K., Suga, S., Dreybrodt, W. & Willmann, F. Theory of degenerate *1s* excitons in zinc-blende-type crystals in a magnetic field: Exchange interaction and cubic anisotropy. *Phys. Rev. B* **11**, 1512–1521 (1975).

Chapter 8

Experimental methods

Abstract

This chapter provides more details on the experimental methods used in this thesis. In particular the preparation of the sample, the two different home-built microscopes used and the technique of differential transmission spectroscopy.

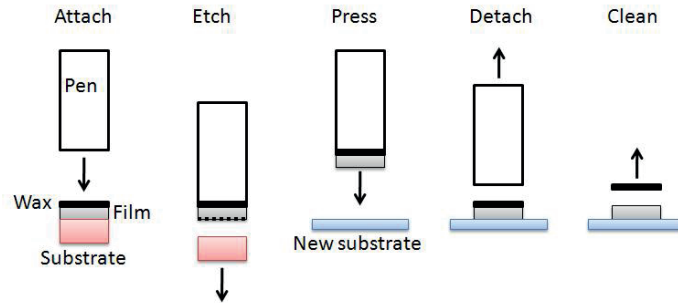


Figure 8.1: ELO procedure. Step 1, the pen is attached to the film by the adhesive strength of the wax. Step 2, the film is removed from its host substrate by etching the epitaxial boundary layer in between. Step 3, the bottom surface of the film is cleaned from any residues left after etching and pressed onto its new substrate of choice. Step 4, the pen is detached by melting the wax. Step 5, all residues of wax are dissolved and the film and substrate are cleaned.

8.1 Sample preparation

The sample is grown by molecular beam epitaxy* as a $10\ \mu\text{m}$ thick layer on top of a GaAs substrate, with an AlAs spacer layer in between. The $10\ \mu\text{m}$ thick layer contains the precisely controlled doping concentration. We have several 2 inch wafers in stock with varying doping concentration, the sample described in this work carries the label W13640 and has a silicon doping concentration of approximately $3 \times 10^{13}\ \text{cm}^{-3}$. This concentration was deduced from measurements of the sample's optical density as the concentration is too low to detect by electrical Hall-voltage measurement [1]. To be able to perform transmission measurement on the epitaxial layer, it is transferred to a transparent substrate using an epitaxial lift-off technique as described in Fig. 8.1. As a new substrate we use sapphire, which is transparent at the wavelengths we use in measurement and has good thermal conductivity to prevent heating of the sample. The sapphire is wedged, meaning that the surfaces are not parallel, preventing Fabry-Perrot type interference. The essence of the lift-off process is that the film is separated from its original substrate by a wet chemical hydrofluoric

*Wafer produced by D. Reuter and A.D. Wieck at Ruhr University of Bochum

acid etch with dissolves the AIAs spacer layer. Then it is transferred to the new substrate to which it binds by van-der-Waals force. To perform this transfer in a controlled manner we temporarily glue the film to the tip of a teflon pen for better handling in the intermediate process. An optical microscope picture showing four ELO films prepared for measurement. The top two and lower left samples had already survived several measurement cycles at the time the photo was taken. In the middle of the top two there are either cracks or debris visible. It is not certain whether these are cracks arising from strain that develops during the large temperature changes that the samples undergo or from the microscope objective touching and damaging the film when attempting to focus. The second option is more likely because the lower left sample has also been cooled down to liquid helium temperature and does not show this damage. The lower right sample was not yet used for measurements. When loaded into the cryogenic microscope it is still possible to assess which regions on the sample are best suited for measurement. The selected regions should be free of damage and debris and show good adhesion to the sapphire substrate. The technique for this is demonstrated and displayed in Figure 8.8. The lift-off procedure is adapted from [2]. For details on the particular recipe used see Appendix A.

8.2 Polarization maintaining fiber microscope

To perform the measurements described in chapters 3, 6 and 7 we use a home-built microscope. A schematic of the microscope is shown in Fig. 8.3 and the setup is described in more detail in [3]. The setup allows light from two lasers to be guided to the sample space by a polarization maintaining fiber, where it is focussed on the sample. The minimum spot size that can be achieved is $2\ \mu\text{m}$. Directly behind the sample is a silicon PIN photodiode that converts light transmitted by the sample to a current, which is amplified immediately outside of the cryostat and directed to a lock-in amplifier. The sample is inside a helium bath cryostat and inside a superconducting magnet which can generate a magnetic field of up to 10 T. An XYZ piezo nanopositioning stage is used to move the sample through the laser spot to adjust focus and position.

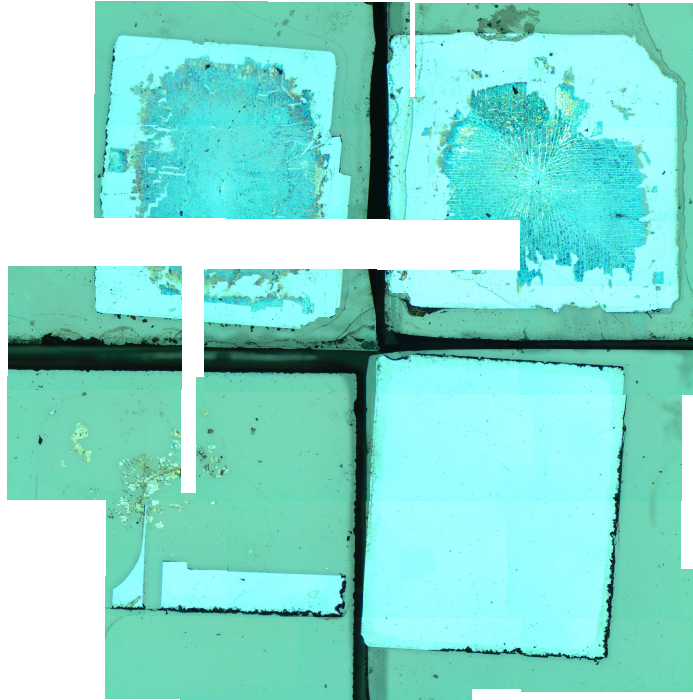


Figure 8.2: Photo of four prepared GaAs ELO films on sapphire. For scale: the top right film is approximately 2-by-2 mm². The top two films had already been used for measurements and have either damage or debris at their centers. The lower left film has also been used but does not have this. The lower right film was prepared recently before the photo was taken and had not been used for measurement yet.

8.3 Multi-fiber microscope

For the measurements in chapter 5 a microscope that incorporates three optical fibers is used. One (polarization maintaining) fiber is used to guide light to the sample and two multimode fibers are used to extract light from the setup after it has passed through the sample. A wire grid polarizer is present inside the microscope, behind the sample, to separate light of orthogonal, linear polarizations and direct it to either of the output fibers. This section contains a description and performance analysis of this setup.

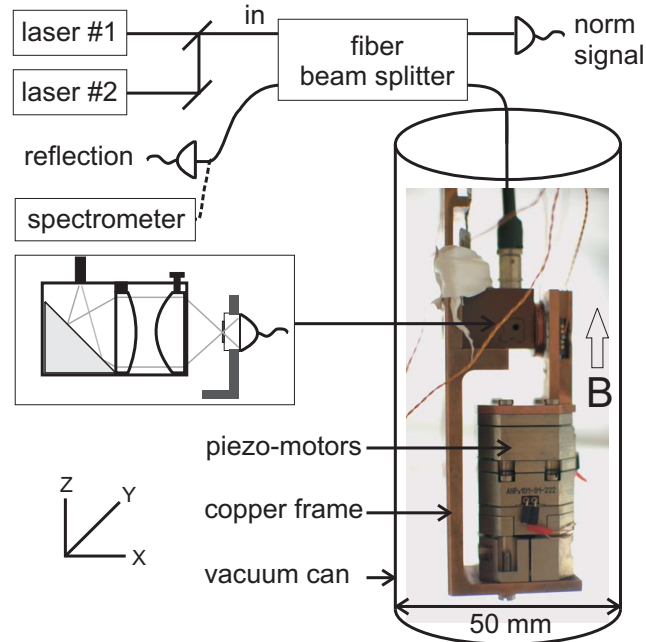


Figure 8.3: Schematic of the experimental setup. Excitation light of two tunable lasers is coupled into a polarization-preserving fiber-based beam splitter and one of the outputs is connected to the fiber that runs to the microscope. This fiber delivers excitation light to the sample, which is mounted on an XYZ-stack of piezo-motors. The sample position can be tuned to be in or out of the focal spot of the two-lens microscope. The microscope is mounted in a tube, which is vacuum pumped and immersed in a Helium bath (4.2 K) or used in a dilution refrigerator. A superconducting coil provides magnetic fields up to 9 T. A silicon PIN photodetector is positioned right behind the sample for detection of the optical transmission. Both the sample and the detector are mounted on a copper sample holder. The second output of the beam splitter is coupled to a photodetector for monitoring the optical powers. Signals that come from reflection off the sample, as well as emission by the sample, retraces the optical path through the fiber. After passing the beam splitter is can be diverted to a regular photodetector, or to a spectrometer. Inset: microscope components mounted on the copper frame that forms the cold finger.

8.3.1 Design and construction

The three fiber coupled confocal microscope is a compact instrument where two microscope objectives are aligned along one axis (Fig. 8.4). S- and/or P-polarized light is guided to the sample using an input fiber and attached to an input confocal microscope. In the sample space the light polarizations are designated relative to the direction of the applied magnetic field as H- and V-polarization (V is parallel to the external magnetic field). It is desirable to collect a maximum amount of the light that has passed through the sample, this is achieved by implementing an output confocal microscope axially aligned to the light propagation direction of the input confocal microscope. The output microscope has larger lenses as compared to the lenses of the input microscope. It has two output fibers with a polarization filter between them to separate H- and V-polarizations and guide them to different fibers. This setup can be used at room temperature as well as at cryogenic temperature measurements.

Experimental requirements set a technological challenge to make a setup which can sustain the temperature of liquid helium in a bath cryostat. Along with that, there is the challenge of having a magnetic field as high as 9 T. Hence required is a non-magnetic material to engineer the setup, which can sustain low temperature and can fit inside the super-conducting magnet bore of 5 cm diameter. The microscope is designed in such a way that if it is required, it can be easily disassembled and reassembled. To minimize the stray reflections and secure the dipstick cone from any damages Vespel, a plastic commonly used in space technology, is used for the body of the coupled confocal microscope. Vespel also allows to clamp the optical elements with low possibility of damaging it. The optical elements are selected for wavelengths near 820 nm since the entire set-up is devoted to the spectroscopy on the shallow donors in GaAs.

8.3.2 Input part

To send polarized light in, we use a PANDA-type polarization maintaining single mode fiber with numerical aperture of 0.13 and diameter of 5 μm . Intentionally designed birefringence of this fiber prevents crosstalk between two modes of orthogonal linear polarization, it maintains the polarization

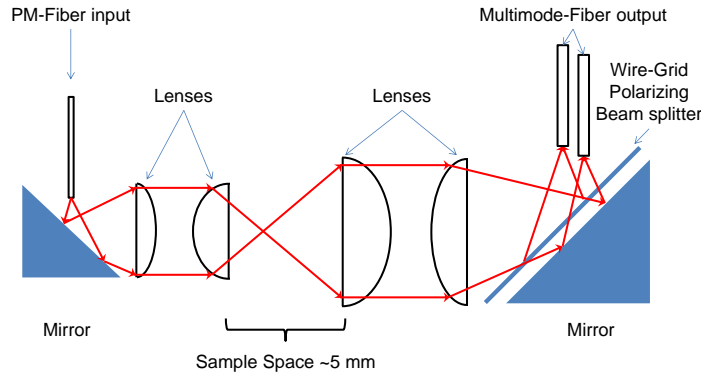


Figure 8.4: Schematic of the three-fiber microscope. The single mode polarization maintaining fiber, mirror and a set of aspheric lenses form the input part of the set-up. It is followed by sample space where the laser light is focused. The sample space is 5 mm. Samples are placed on a copper cold finger which is attached to XYZ piezo motors to for 3D positioning of the sample with nanometer precision. The next pair of aspheric lenses form a second confocal microscope which contains a wire grid polarizer to separate H- and V-polarizations and send it into two multi-mode fibers which guide the light out of the cryostat.

even in the presence of magnetic fields. The polarization robustness is tested and confirmed to be maintained up to 9 T of magnetic field [3]. The light propagation direction out of the polarization maintaining fiber (Fig. 8.4) is altered by 90° using a mirror (Thorlabs MRA05–E02) to ensure the experiment is performed in the Voigt geometry. The light coming out of the fiber is divergent and is subsequently collimated by an aspheric lens of 1.5 mm clear aperture having 5 mm focal length (Thorlabs 350430) with numerical aperture of 0.15. The light is focused on the sample using a lens with focal length 1.45 mm and with numerical aperture 0.55 (Thorlabs 350140).

8.3.3 The sample space and the holder

The sample space is after the input microscope and is 5 mm long (Fig. 8.4). The samples are adhered on sapphire substrate. The sapphire is mounted on the copper cold finger using silver paint to facilitate heat conduction

away from the sample. The copper cold finger is attached on piezo stages (Attocube anc120) for precise control over XYZ positioning. The detailed explanation of selecting a spot on the sample, aligning the focus and the minimum spot size analysis are explained in earlier work [3] which used an equivalent input part for the microscope.

8.3.4 Output part

The light which passes through or is emitted by the sample is further collected and collimated using an aspheric lens of clear aperture of 4.95 mm having focal length 4.51 mm with numerical aperture of 0.55. The second lens is an aspheric lens with focal length of 13.86 mm and clear aperture of 5.1 mm to focus the collimated light on the core of the multi-mode fibers which guide the collected light out of the cryostat (Fig. 8.4).

It is desired to separate linear H- and V-polarization in Voigt geometry for the experiments. To achieve it, a wire grid polarization (WGP) beam splitter (Edmund Optics #48-544), consisting of silver wires on 700 μm thick Corning 1737F glass with refractive index 1.51 is placed below the two output fibers, on top of a mirror (Thorlabs MRA05-E02). An analysis of reflection and transmission of light from the grating is done to determine the optimum orientation of the WGP. For this it should be taken into account that the incoming V-polarized light is P-type (parallel) with respect to the plane of reflection, and similarly H translates to S-type ('senkrecht', i.e. perpendicular). The WGP is coated on one side with antireflection coating for the wavelengths between 420 nm to 670 nm to minimize Fabry-Pérot effect for the two different polarizations. This means at the operating wavelengths in the present setup, the Fabry-Pérot effect is present more (at 820 nm) than the specified values for the wavelength range specified on the manufacturers' data sheet. The WGP is placed in such a way that H-(S-)polarized light will be reflected from the WGP and V-(P-)polarized light will be transmitted through the WGP surface (twice, once again after it reflects off the mirror). Once again all elements are fixed in Vespel to avoid any damage to optical elements as a consequence of deformations by large temperature changes.

Excitation and scattered light from the focal volume of the output part

of the microscope is directed towards the output fibers via the WGP. H-polarized light is reflected from the surface of the WGP and is collected in the first multi-mode fiber (OZ Optics, partnr. VAC-01-V-QMMJ-3, XF-IRVIS-1000/1100-3- 6.6, 1.4:AR2). The part of the light which is transmitted through the WGP is focused into second multi-mode fiber (OZ Optics, same partnr.) to collect V-polarized light (Fig. 8.4).

8.3.5 Performance

To study the performance, experiments were carried out with and without a sample at room temperature as well as at 4.2K. It includes checks on output stability as a function of time as well as wavelength, the fidelity of polarization separation in the two output channels and spectroscopy on an n-GaAs film.

8.3.6 Two channel output stability

The stability of the output intensity is important for sensitive quantum optics experiments to be performed in the future. The output stability was monitored as a function of time for both the output channels. During this experiment polarization mixing is also observed. It can be seen in the Fig. 8.5. H-polarized light was sent in the setup, the Fig. 8.5 shows stability of H-polarized light coming out of H and Voutput channels by the purple and the cyan colours respectively. The V-channel shows traces of the H-polarized light. Similarly, V-polarized light was sent in the setup and two output channels were monitored. The stability of the V-polarized light steered out of the H- and V-polarized output is shown by the red and the blue colour respectively. It also reflects some trace of V polarized light out of the H-polarized channle output. This experiment was performed at 4.2K and the output was normalized. There was no sample present in the laser sample space.

At 4.2K, the output of the two channels is compared as a function of wavelenghts (Fig. 8.6). For the same wavelength range the polarization was altered to check the output. It is clear that the coupling of light in both the channels is different. For the transmitted light from the glass

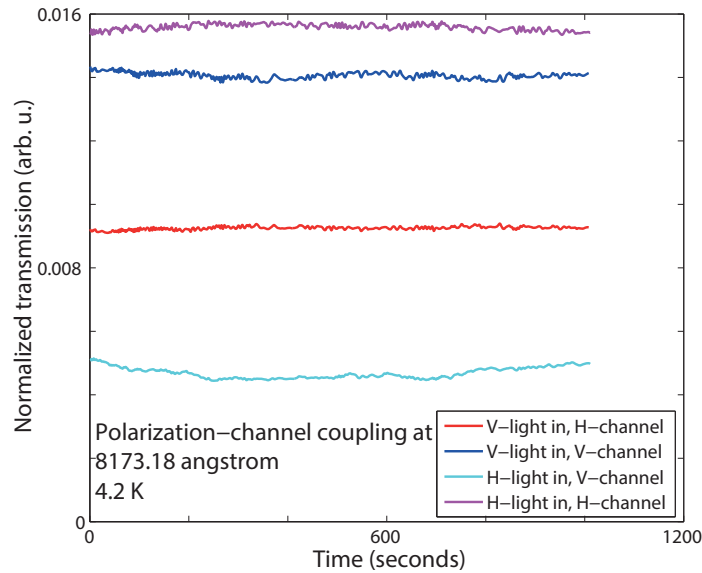


Figure 8.5: The figure shows the output stability of H- and V-polarization output as a function of time. H-polarized light is sent in the setup and detected at the two outputs. The H-polarized light reflected from the grating is shown in purple. The other channel for the V-polarized light transmitted from the grating is showing some trace of the H-polarized light and is shown in light blue. When V-polarized light is sent in, the V-polarized channel output is shown by the blue colour. The H-channel is giving out traces of V-polarized light is shown in the red colour.

plate (V-polarized), it is expected to have Fabry-Pérot pattern and can be seen by the trace in the blue colour. For H-polarized light this would not be expected strongly since this should reflect from the grating and not enter the plate. There is some interconnection between Fabry-Pérot and output of the two channels. The pattern is out of phase between the two channels.

8.3.7 Two channel polarization separation

The polarization separation was also checked in the two channels. The H- and V-polarization was first fixed on the table and it is recorded at the end of the input channel as a pure H- and V-polarization respectively. These

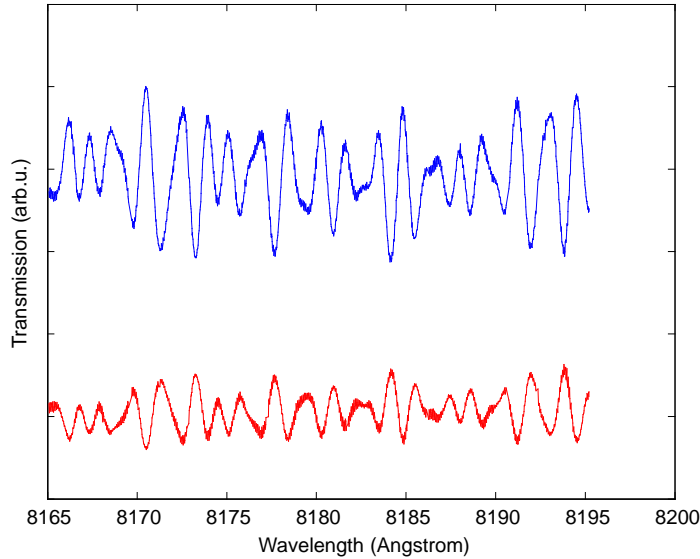


Figure 8.6: The output of the H(blue)- and V(red)-polarization channels is shown as a function of the wavelength. It shows out of phase Fabry-Pérot oscillations from the two different output channels.

are the only two stable polarizations as a function of time which a single mode fiber can carry. The lambda plate reading on the table was recorded and labeled stable angles. These stable angles are shown in the Fig. 8.7 by vertical black lines separated by 90° . The lambda plate is rotated in the steps of a few degrees over the entire range and output of both the channels is recorded. The output showed out of the phase relation to in the output intensity. This experiment was performed at room temperature (Fig. 8.7 (a)) as well as at 4.2 K (Fig. 8.7 (b)). The outcome of the experiment was very similar. It is plotted by normalizing it with respect to the intensity of the input light as well as with respect to the two polarization output channels. Fits are used to find the maxima and the minima from the recorded data. The two measure differences are observed at 4.2 K as compared to the room temperature. First, the amount of light coupled at 4.2 K is 10 times less as compared to the room temperature. It happens due to the contraction of all the setup at low temperature which is causing alignment errors. Second, the difference in stable angle versus detected

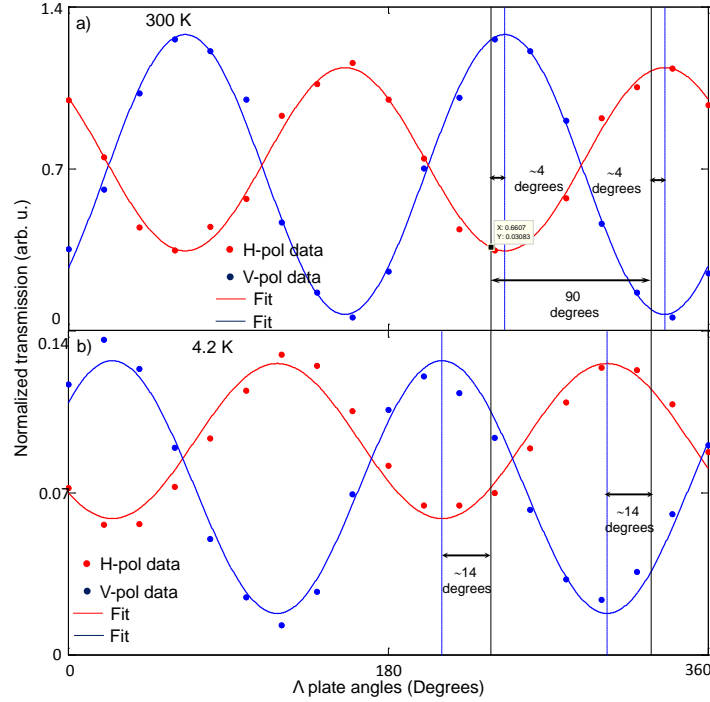


Figure 8.7: (a) Polarization separation in the channels. Normalized intensity output from the two different multi-mode fiber output channels as a function of input polarization angle at room temperature. (b) Normalized intensity output from two different multi-mode fiber output channels as a function of input polarization angle at 4.2 K.

absolute polarization maxima has increased a lot. At room temperature this difference is 4° (Fig. 8.7 (a)). At low temperature it changes and becomes 14° (Fig. 8.7 (b)). The speculation is that the temperature gradient along the input channel can cause the change in the polarization or ellipticity of the light at the end of the channel. The performance is further studied by executing measurements on a sample. We work with ultra-pure n-GaAs which is intentionally very low doped. The doping concentration is below $3 \times 10^{13} \text{ cm}^{-3}$. This is $10 \mu\text{m}$ thick n-GaAs which is grown by MBE technique on a semi-insulating GaAs substrate. This intentionally low doped GaAs contains silicon as a donor impurity. At such a low concentration donors are well separated. At low temperatures these donors

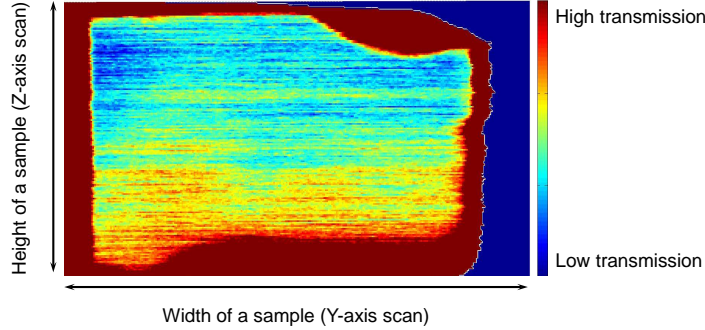


Figure 8.8: (a) A 2 dimensional scan of the n-GaAs film. To obtain such an image, laser wavelength is kept fixed at a wavelength in the transmission window between $X_{n=1}$ and $X_{n=2}$ and has maximum transmission. The piezo motors were scanned to take a transmission image of the entire film. The resolution of this image is limited by the minimum spot-size of the microscope.

are neutral (unionized) with an extra electron localized at a donor site. This forms an ensemble of a solid-state version of alkali atoms which is of interest for quantum optics experiments. The transition from donor-bound electron D^0 to donor-bound exciton D^0X [4, 5, 6] is of primary interest. $10\mu\text{m}$ thick film is separated from the substrate using epitaxial lift off process [2]. The separated film is placed on a sapphire substrate and adhered with Van der Waal's forces. Sapphire substrate provides good transparency near 820nm wavelength and also provides heat sink to the GaAs film. A transmission spectroscopy is performed on such a sample.

During the transfer of GaAs film on the sapphire substrate it is possible to have local strain at a few places within the film. Presence of strain or stress causes change in the band structure and one should expect shift and/or broadening of transitions. For experiments we need to have strain-free part of the film so that from the donor-bound electron to donor-bound exciton ($D^0 - D^0X$) transition is narrow with clean selection rules and they appear at expected energy (frequency).

To find a stress free spot for the experiments a technique is developed. It is well known from the GaAs spectrum at 4.2K , that there is a quite broad transmission between free exciton $n = 1$ ($X_{n=1}$) and free exciton $n = 2$ ($X_{n=2}$). The well-established effect of stress on exciton transitions

in GaAs [7, 8] is used to image a sample film. A wavelength having a maximum transmission at the edge of the transition ($X_{n=2}$) is chosen for the transmission spectroscopy of a GaAs sample. In this spectroscopy the frequency is kept fixed and the transmission is monitored as a function of the position on the film. It gives the intensity of transmitted frequency at each point on the film as shown in the Fig. 8.8. After plotting this data, the spectroscopy as a function of laser frequency is performed on the region of maximum transmission. The maximum transmission is shown in the red colour in the Fig. 8.8. If the film is strained or not properly heat sinked, then all the transitions are broadened and are shifted towards the lower frequency side [7]. In these cases the band edge shifts towards the lower frequency side and it gives bad transmission due to stress effects, strain effects or heating effects. This method saves a lot of time in finding a $\sim 10 \mu\text{m}^2$ spot on a 4mm^2 film which has lowest possible strain.

8.3.8 The transmission spectroscopy

The transmission spectroscopy is performed in details to study the transitions below the band gap and identify them. In the Fig. 8.9 (a) the transmission spectroscopy on n-GaAs at 0 T magnetic field is shown. In this figure we clearly see a very strong transition showing $X_{n=1}$. Next to it the donor-bound exciton transition can be observed. The lowest energy transition from all the $D^0 - D^0X$ transition is further identified using spectroscopic measurements. This transition is used to perform experiments like Electromagnetically induced transparency [4, 5, 6].

8.3.9 The luminescence spectroscopy

The luminescence spectroscopy is performed to observe GaAs spectral features Fig. 8.9 (b). These features are always present below the bandgap and between the range 815 nm to 825 nm. The principal interest is in the spectral features which appear due to donor-bound excitonic states. A sample is illuminated with the excitation light of the energy above the bandgap using single mode polarization maintaining fiber. The multi-mode

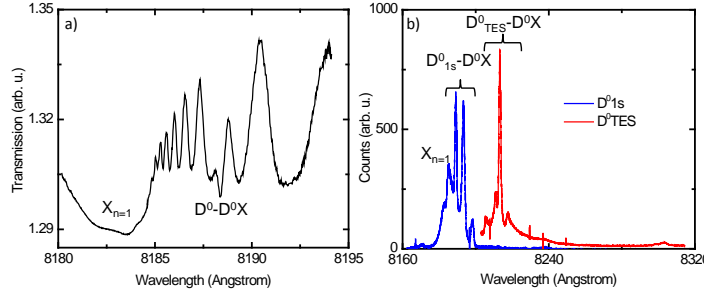


Figure 8.9: (a) Transmission spectrum of the GaAs film at zero magnetic field. Above figure shows a transmission spectrum at zero magnetic field which is collected from the sample. The transitions which are indicated are identified as $D^0 - D^0X$, Free exciton $X_{n=1}$. (b) Photoluminescence: The figure shows photo-luminescence from the n-GaAs film. One can clearly see the features marked and identified as exciton, neutral donor-bound exciton ($D_{1s}^0 - D^0X$), and ($D_{TES}^0 - D^0X$). This spectrum was detected from the channel which collects V-polarized light.

fiber which gives V-polarized output is aligned with the PI Acton spectrometer equipped with liquid nitrogen-cooled CCD camera. In the figure above a typical spectrum at 0 T can be seen. It shows several features in the spectral range these are observed and identified as free exciton, neutral donor-bound exciton, ionized donor-bound exciton, acceptor bound exciton and two electron satellite (TES) [9, 10]

8.4 Differential transmission spectroscopy[†]

We model a setup where two continuous-wave laser fields co-propagate through a medium, as shown in Fig. 8.10(a). One field, depicted by its angular frequency ω_{mod} , is undergoing on-off modulation at frequency f_{mod} by a chopper. The other field, with angular frequency ω_c , is not modulated and hence has a constant intensity. The total transmitted power is converted into an electrical signal by a linearly behaving photodiode after the sample. A lock-in amplifier isolates the electrical component at

[†] This section is based on reference 5 on page 151

frequency f_{mod} from all other components.

The modulation is orders of magnitude slower than the electronic dynamics in the medium and is assumed to have a square on-off envelop. This leads to two steady-state situations with transmittance $T_{\omega_{\text{mod}}}^{\text{on}}$ for the modulated field and transmittances $T_{\omega_c}^{\text{on}}$ and $T_{\omega_c}^{\text{off}}$ for the constant field. If the probed medium has nonlinear components in the susceptibility, *i.e.* the susceptibility depends on the presence of laser fields, $T_{\omega_c}^{\text{on}}$ and $T_{\omega_c}^{\text{off}}$ are in general not equal. Consequently, the transmittance of the constant field is time-dependent with frequency f_{mod} in the form of amplitude modulation of its transmission. This transfer of amplitude modulation from one field to another via the susceptibility will be called cross-modulation, and the contribution of the constant field to the transmission at frequency f_{mod} will be called differential transmission. The frequency component at f_{mod} of the total transmitted power thus consists of two parts and is given by

$$P_{f_{\text{mod}}} = \underbrace{P_{\text{mod}} T_{\omega_{\text{mod}}}^{\text{on}}}_{\text{normal transmission}} + \underbrace{P_c (T_{\omega_c}^{\text{on}} - T_{\omega_c}^{\text{off}})}_{\text{differential transmission}} \quad (8.1)$$

where P_{mod} (P_c) is the power of the modulated (constant) field, and where P_{mod} and P_c are incident on the medium while $P_{f_{\text{mod}}}$ is measured after the medium. We will focus on scenarios with $P_{\text{mod}} < P_c$ to ensure a prominent role for the differential transmission. Figure 8.10(b) illustrates the transmitted power for the individual fields and the total transmitted power, for qualitatively different levels of cross-modulation. If cross-modulation is absent, the contribution of differential transmission in Eq. (8.1) is zero, and the lock-in signal consists purely of the normal transmission of the modulated field. For increasing levels of cross-modulation, the contribution of the differential transmission to the lock-in signal increases. When the differential transmission is larger than the normal transmission, and of opposite sign (which is the case for lambda systems), the total transmitted power shows a 180° phase shift. This shift manifests itself in the lock-in signal either as a negative signal or a 180° phase shift, depending on lock-in operation settings.

The medium of interest consists of lambda systems, as shown in Fig. 8.10(c). Two ground states $|a\rangle$ and $|b\rangle$ have optical transitions to common excited states $|e\rangle$, $|e'\rangle$, *etc.* There is no optical transition between $|a\rangle$ and $|b\rangle$.

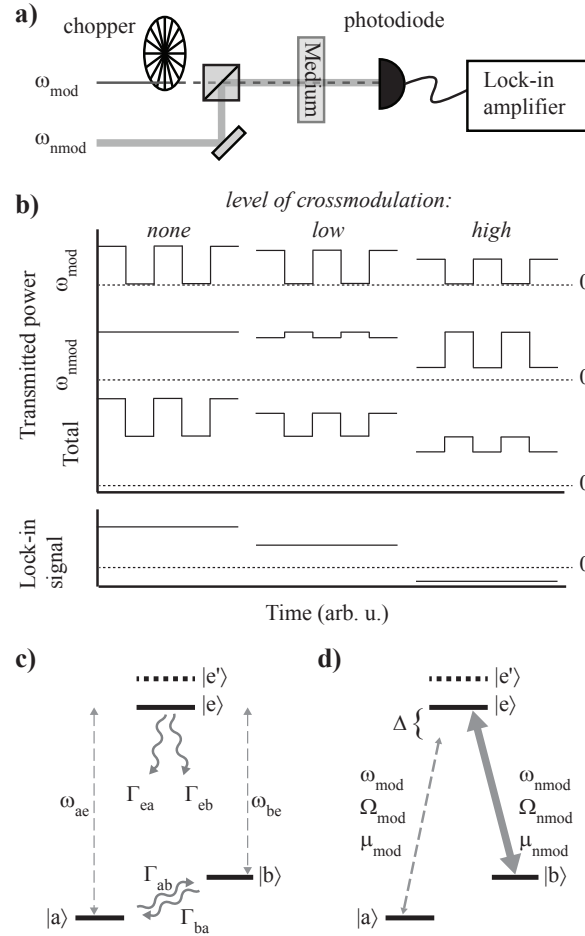


Figure 8.10: a) Experimental setup for differential transmission spectroscopy. Two overlapping laser fields, of which one is modulated by a chopper, co-propagate through the medium. Transmitted light is converted into an electrical signal by a photodiode. A lock-in amplifier filters out the signal component at the modulation frequency. b) Schematic illustration of the transmitted power of both laser fields, and the resulting lock-in signal. Signals are plotted for three qualitatively different levels of cross-modulation. c) Four-level Λ system with ground states $|a\rangle$ and $|b\rangle$ and excited states $|e\rangle$ and $|e'\rangle$, with optical transitions from both ground states. The transitions of $|a\rangle$ and $|b\rangle$ to $|e\rangle$ have energies $\hbar\omega_{ae}$ and $\hbar\omega_{be}$. Population relaxation rates Γ_{ij} are depicted by curly arrows. d) The modulated and constant laser, with frequency ω_{mod} and ω_c respectively, couple to the transitions with dipole moment μ_{mod} and μ_c , resulting in Rabi frequencies Ω_{mod} and Ω_c . When lasers only address transitions to $|e\rangle$ the system behaves as a three-level system. One laser is coupled resonantly, while the other (in this figure the modulated laser) is scanned over resonance by changing the detuning Δ .

Relaxation parameters Γ_{ij} describe both spontaneous emission rates from the excited states to the ground states and thermalization of population in the ground states. Furthermore, all states except $|a\rangle$ undergo pure dephasing γ_b, γ_e , etc. For the sake of simplicity, the simulations will be restricted to three-level lambda systems, without loss of validity.

Differential transmission spectroscopy is modeled with two laser fields coupled to the optical transitions with transition dipole moments μ_{mod} and μ_c , see Fig. 8.10(d). One field is held resonant with its transition frequency, while the other is scanned over the resonance by changing its detuning Δ . It is assumed that each laser couples only to one transition. The lasers drive transitions between the levels at Rabi frequencies Ω_{mod} and Ω_c .

The population in $|e\rangle$ spontaneously decays to both ground states, with relaxation rates Γ_{ij} . Hence, a field present at transition ω_{ae} (ω_{be}) will effectively pump population to state $|b\rangle$ ($|a\rangle$), increasing the absorption coefficient for the field at transition ω_{be} (ω_{ae}). In Eq. (8.1) this results in the contribution $(T_{\omega_c}^{\text{on}} - T_{\omega_c}^{\text{off}})$, which is always negative for lambda systems. The amount of population pumped from one ground state of the lambda system to the other depends on the ratio of relaxation coefficients Γ_{ea} and Γ_{eb} . The relaxation coefficient of a transition is related to its electric dipole moment by

$$\Gamma_{ij} = \frac{2n\omega_{ij}^3\mu_{ij}^2}{3\epsilon_0hc^3} \quad (8.2)$$

where n is the bulk refractive index. The branching ratio Γ_{ea}/Γ_{eb} is given by

$$\frac{\Gamma_{ea}}{\Gamma_{eb}} = \frac{\omega_{ea}^3\mu_{\text{mod}}^2}{\omega_{eb}^3\mu_c^2} \approx \left(\frac{\mu_{\text{mod}}}{\mu_c}\right)^2, \quad \text{for } \omega_{ae} \approx \omega_{be} \quad (8.3)$$

The ratio μ_{mod}/μ_c , which we will call *relative dipole moment*, is the main parameter that determines the amount of cross-modulation and differential transmission.

The transmittances are determined by the imaginary part of the susceptibility by

$$T(\omega) = \exp\left(-\frac{z\omega}{c}\text{Im}[\chi(\omega)]\right) \quad (8.4)$$

where z is the sample thickness and c is the speed of light in vacuum. For each field $\chi(\omega)$ is calculated by

$$\chi(\omega) = \frac{2N\mu_{ij}^2\sigma_{ij}(\omega)}{\epsilon_0\hbar\Omega} \quad (8.5)$$

where N is the number density of lambda systems in the material. The slowly oscillating part of the transition's coherence σ_{ij} is obtained from the steady-state solution of the master equation for the density operator

References

- [1] Maksym, S. *Quantum Optical Control of Donor-bound Electron Spins in GaAs* (University of Groningen, 2011).
- [2] Yablonovitch, E., Gmitter, T., Harbison, J. P. & Bhat, R. Extreme selectivity in the lift-off of epitaxial gaas films. *Applied Physics Letters* **51**, 2222–2224 (1987).
- [3] Sladkov, M. *et al.* Polarization-preserving confocal microscope for optical experiments in a dilution refrigerator with high magnetic field. *Review of Scientific Instruments* **82**, – (2011).
- [4] Wang, T., Rajapakse, R. & Yelin, S. Electromagnetically induced transparency and slow light with n-doped gaas. *Optics Communications* **272**, 154 – 160 (2007).
- [5] Fu, K.-M. C., Santori, C., Stanley, C., Holland, M. C. & Yamamoto, Y. Coherent population trapping of electron spins in a high-purity n -type gaas semiconductor. *Phys. Rev. Lett.* **95**, 187405 (2005).
- [6] Sladkov, M. *et al.* Electromagnetically induced transparency with an ensemble of donor-bound electron spins in a semiconductor. *Phys. Rev. B* **82**, 121308 (2010).
- [7] Schairer, W., Bimberg, D., Kottler, W., Cho, K. & Schmidt, M. Piezospectroscopic and magneto-optical study of the sn-acceptor in gaas. *Phys. Rev. B* **13**, 3452–3467 (1976).
- [8] Nam, S. B. *et al.* Free-exciton energy spectrum in gaas. *Phys. Rev. B* **13**, 761–767 (1976).
- [9] Karasyuk, V. A. *et al.* Fourier-transform magnetophotoluminescence spectroscopy of donor-bound excitons in gaas. *Phys. Rev. B* **49**, 16381–16397 (1994).
- [10] Bogardus, E. H. & Bebb, H. B. Bound-exciton, free-exciton, band-acceptor, donor-acceptor, and auger recombination in gaas. *Phys. Rev.* **176**, 993–1002 (1968).

Chapter 9

Conclusion and outlook

The phenomenon of electromagnetically induced transparency (EIT) with donor-bound electrons in GaAs (D^0 systems) is an important precursor to allow for light storage and all-optical switching in this material. The fact that this is achievable in a common semiconductor material as GaAs is relevant for future applications, because the large body of expertise on growth and processing techniques for this material can facilitate the step to device fabrication. The measured electron spin dephasing time of 3 ns (Chapter 2) is however rather short for progressing to experiments on stored light. The effective lifetime of the associated spin coherence so short that verifying properties like spin-spin or spin-photon entanglement is very challenging, even in a laboratory setting.

The fact that the EIT resonance can serve as a probe for the nuclear spin polarization makes it also a useful tool for investigating changes induced in the nuclear spin bath by dynamic nuclear spin polarization (DNP). Using a differential transmission spectroscopy technique we have shown the possibility to measure the build up and decay times of DNP near donor bound electrons in GaAs. We find the DNP dynamics to take place on a timescale of minutes (Chapter 3) under the experimental condition of a strong magnetic field of 6.4 T and low temperature of 4.2 K. This implies the possibility to first prepare the nuclear spins and then to perform the manipulations on the electron spin (in the modified nuclear spin bath).

The method developed to reduce fluctuations of the nuclear spins along

the external magnetic field can improve the electron spin coherence time. This all-optical method has as advantage that it can reduce the nuclear spin fluctuations while giving direct optical feedback by enhanced laser transmission through the sample. In Chapter 4 we use the model with parameters representative for case of the D^0 - D^0X in GaAs, to yield an improvement factor of 7. The implementation of the proposal, Chapter 5, shows half of the effect: A splitting is visible for the predicted configuration, but the narrowing is not. The fact that this splitting is indeed observed nevertheless confirms that the two-laser DNP driving scheme is compatible with both predicted effects. For further experiments to confirm this it is important to improve the intensity distribution of the pumping lasers inside the sample. Based on the current results we expect that because the DNP is an intensity dependent effect, the variation of intensity within the laser spot (due to the Gaussian beam profile and Fabry-Perot interference inside the sample) can obscure the nuclear spin narrowing effect. Anti-reflection coating on the sample and aperture to create a homogeneous laser spot could resolve this.

Chapters 6 and 7 provide supporting information for the DNP experiments in earlier chapters. The measurements in Chapter 6 were originally intended to reinforce the proof that DNP was observed by checking the dependence on pump laser frequency. If shifts in EIT resonance should occur for pumping off resonance with the exciton states (into the conduction band, or deeper inside the bandgap) this would shed a different light on the statements in Chapter 3. The results were in accordance with our expectations, but a surprising effect was that pumping inside the exciton line turned out an easy method to create large Overhauser fields (300 mT) of either sign, depending on the pump laser frequency. Because local magnetic fields are not an easy resource to come by in spintronics (magnetic fields are often generated over large volumes using electromagnets), such internal magnetic fields could prove useful.

Besides improvements on the GaAs measurements, there is the possibility to apply the techniques used in this thesis on other systems. The nuclear

spin narrowing proposal of Chapter 4 has some generality and it could be explored in quantum dots or localized spins in other semiconductors (as we also discuss in the chapter). The recently measured CPT on localized spins in silicon carbide is another example (described in reference 6 on page 151). This is a deep defect, as opposed to the shallow donor in GaAs. The possibility to eliminate the nuclear spins from this material is promising. A downside is that electrons of the deep defect, which are highly localized on the defect lattice sites, couple to vibronic modes of the defect. This results in a large portion of emission in the phonon-side band while emission into the zero phonon line is wanted for quantum information related work.

Appendices

Appendix A

Epitaxial lift-off recipe

1. Samples cut from a GaAs wafer, with approximate size of 2 by 2 mm, are placed on a heating plate (initially turned off) with the substrate facing down and the layer that is to be lifted off facing up. Initial cleaning of the protection resist layer that is sometimes present is not necessary, since it protects the surface from scratching when it gets attached to the pen. The protection resist layer will give extra support after the lift off is complete and will be finally removed after the ELO film is placed on its new substrate.
2. The ELO pen is made ready by mounting Teflon tape on the tip and the tip is set to the outer position by turning the screw on top of the pen.
3. A grain of black wax (Apiezon) is put on top of the sample and the heater is turned on. Heat up the plate just high enough to gradually melt the wax around 100°C.
4. While the tip is set in the outer position, the pen is lowered onto the sample and the heater is turned off. Wait for the heating plate to cool off and the wax hardens.
5. When the wax is hardened, the pen plus sample can be picked up and the sides of the sample can be cleaned with trichloroethylene (TCE). Note: When the sample comes loose during cleaning it means that the wax failed to connect between the sample/Teflon tape and steps 2-4 have to be repeated.

6. After cleaning the sides, the tip of the pen is retracted to induce strain on the film. It is important that all wax is removed at the sides to ensure that the etching fluid comes in contact with the AlGaAs layer that is to be removed.
7. Next the pen is mounted above hydrofluoric acid (HF) (solution of 10%) with only the tip plus sample submerged in the solution to start the etching process. A time period of 12 hours etching is sufficient for a 2 by 2 mm sample at room temperature.
8. After etching the pen is cleaned in water to remove traces of HF and the residues of wax are removed by submerging the pen in TCE for a few seconds. Note: Keeping the ELO film too long in TCE will dissolve the wax that is between the pen and the ELO film and the ELO film may come off. At this stage the film should stay connected to the pen and only the bottom layer is to be cleaned to ensure good contact to the new substrate. To complete the cleaning process of the bottom layer the pen is dipped first in acetone followed by isopropyl alcohol (IPA).
9. The sapphire substrate is aligned and placed in the holder. A layer of water is sprayed on top of the substrate. The holder together with the pen are placed on the cold heating plate. The pen is gently lowered to stick the sample onto the substrate. The weight of the pen will squeeze the sample in place. While the water evaporates the sample is pulled close to the substrate, van der Waals bonding eventually attaches the film to the sapphire. Typically, drying will take around 12 hours.
10. After drying the pen is retracted by adding enough heat to melt the last wax contacts between the sample and pen. About 5 minutes is enough, this also induces a bake out process where bonding strength increases.
11. The last step is removing all residues of contamination on the top layer off the sample plus the substrate with the use of TCE, Acetone and IPA in this particular order.

Appendix B

Microscope input/output analysis

NOTE: light labeled 'V' when referring to the magnetic field/sample is called 'p' here referring to the reflection plane at the wire grid polarizer (WGP). Similarly 'H' refers to 's'. However, it is argued here that polarization inside the microscope will generally not be purely H or V. The control of the polarization of ingoing light is done by rotating a lambda plate over a particular angle, measured in degrees. In the text we use the settings of the lambda plate to refer to the polarization setting: value 119 in practice means that the light enters the microscope V polarized (which is not necessarily purely V at the sample) and 164 in practice means that light enters H polarized. Here 119 and 164 refer to the degree indicator on the lambda plate.

B.1 General considerations

For the input/output parameters of the WGP (Edmund Optics, parntr. 48544, Polarizing Plate BS 12.5MM SQ) the following has to be taken into account:

- The object acts as a composite element made up of a glass plate and a grating. Since the grating is on the surface the case is hard to solve but we can say something about the two separate parts that make up the WGP.
- The transmittance and reflectance of a glass plate depend on the polarization of the incoming light, p or s, thickness and angle of

incidence. We have 700 μm thick Corning 1737F, which has refractive index $n = 1.51$ and hence reflectances of $R_p \approx 8.9 \times 10^{-3}$ and $R_s \approx 9.4 \times 10^{-2}$ under angle of incidence $\pi/4$. if there is no anti-reflection coating, transmittance is given by:

$$T = \frac{(1 - R)^2}{(1 + R^2 - 2R \cos(\delta(\lambda)))}$$

$$\delta(\lambda) = \frac{2\pi}{\lambda} 2nl \cos(\theta)$$

which for the case described is plotted in figures B.1 and B.2. However, as can be seen from the company datasheet, there is a coating which is specified to give reflectance from the backside being less than 0.8% for both s- and p-light at wavelength 420 nm to 670 nm (we are unsure of it's performance at 820 nm). So the magnitude of a Fabry-Perot effect might be more similar to figure B.1, on the order of a few percent. It can be concluded here that it is important to orient the grating such that p-light is transmitted, and s-light which shows deeper FP is reflected at the grating and doesn't enter the plate much.

- The grating will induce losses in this setup. According to literature on the subject (Palmer, Christopher A., and Erwin G. Loewen. *Diffraction grating handbook*. Springfield, Ohio, USA: Newport Corporation, 2005.) it is plausible that 10% of light goes to the first order diffraction spots and thus does not enter the outgoing fiber (only zero'th order specular reflection is collected). The company datasheet describes also losses of the order of 10%, again only specified up to 700 nm.

B.2 Data

- So since the WGP is quite complex we measured the reflection and transmission properties of the isolated WGP under an angle of 45° , at room temperature. This data can be summarized as follows: We work in the configuration where the grating lines are perpendicular to the reflection plane. Denote fraction of reflected p-light

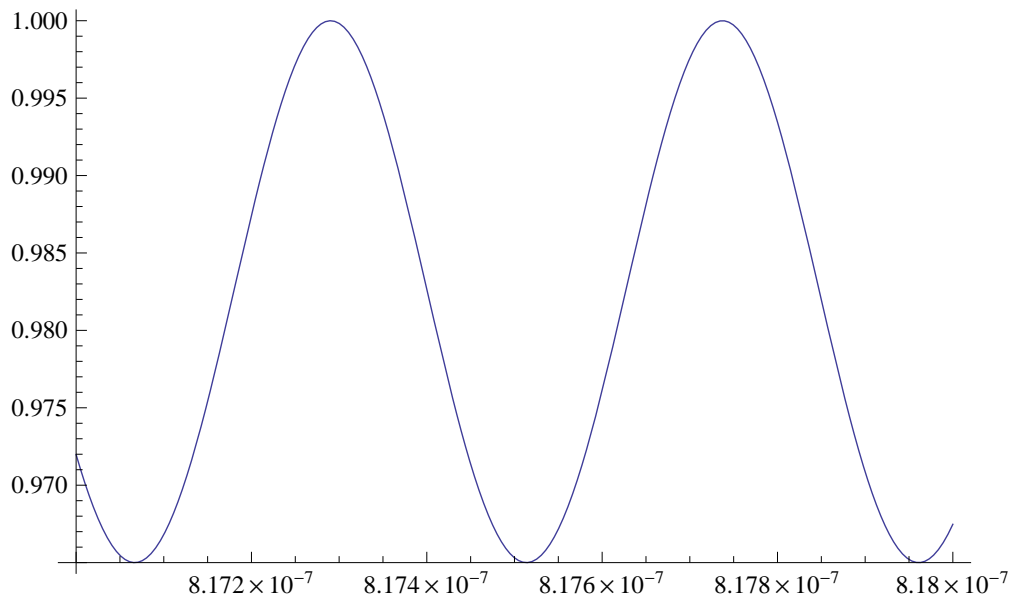


Figure B.1: Etalon under $\pi/4$, p-light transmittance vs wavelength.

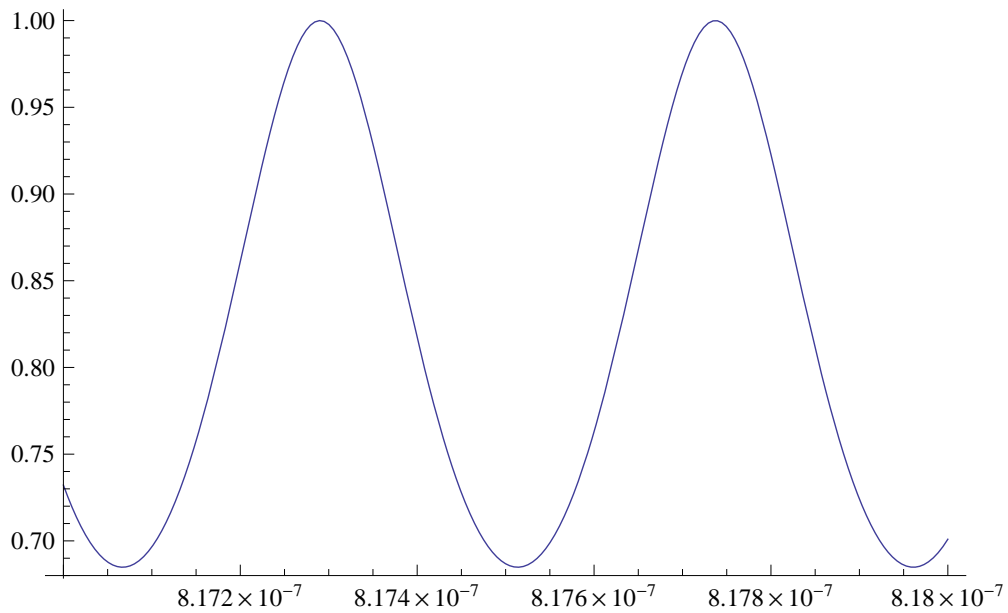


Figure B.2: Etalon under $\pi/4$, s-light transmittance vs wavelength.

by $f_{11} = 0.149$, transmitted p-light (anticipating two passes) as $f_{12} = 0.524$, reflected s-light by $f_{21} = 0.641$ and transmitted s-light (anticipating two passes) by $f_{22} = 0.00880$. These numbers govern input/output of the WGP and let us assume they remain constant as the temperature drops to 4.2K. Note that the losses in these measurements are up to 35%.

- A FP type effect is shown in figure 8.6, where p-light is incident on the grating. Since this is transmitted, FP from the glass plate can be expected. For s-light this would then not be expected (strongly) since this should reflect from the grating and not enter the plate.
- The microscope's input/output data is in figure 8.7. There are only two types of polarization that remain stable (over time) while travelling through the fiber, these are marked with vertical black lines. This stability is shown in figure 8.5. They are the only polarizations we can use in order to have the input/output relation stable in time during the experiment. When they arrive at the sample space these polarizations are not pure s- or p-light, they can have acquired some rotation and/or ellipticity. We call the incoming polarizations i_{119} and i_{164} . The grating now works as an analyzer that decomposes this incoming light into p and s components and directs it to the output channels in accordance with the f_{ii} numbers mentioned above. We take the decomposition of the polarizations as:

$$p_{119} = \cos(\zeta_{119})^2 i_{119}$$

$$s_{119} = \sin(\zeta_{119})^2 i_{119}$$

$$p_{164} = \cos(\zeta_{164})^2 i_{164}$$

$$s_{164} = \sin(\zeta_{164})^2 i_{164}$$

This means that given an input intensity e.g. i_{119} (i.e. set lambda plate to 119, read i on the power meter), the intensity of p-polarized light at the WGP is p_{119} . The ζ 's are not real rotation angles, they capture both rotation and ellipticity.

- Light that is directed to either fiber enters that particular fiber with a certain coupling efficiency: η_1 and η_2 .

B.3 Results

We have three sets of measurement points that can be used to derive the input output characteristics. One at room temperature, figure B.3, and two at 4.2K, figures B.4 and B.5. Output powers are all denoted as fractions of power going into the microscope. They are denoted as u_{ij} where i labels the polarization of the incoming light (setting of the lambda plate) and j labels the output channel. The 'transfer function of the microscope' is made up of the mixing angles ζ_i , the coupling efficiencies η_i and the WGP's f_{ij} numbers. They can be found from the measured output values u_{ij} as:

$$u_{11} = \eta_1(\cos(\zeta_{119})^2 f_{11} + \sin(\zeta_{119})^2 f_{21}) \quad (\text{B.1})$$

$$u_{12} = \eta_2(\cos(\zeta_{119})^2 f_{12} + \sin(\zeta_{119})^2 f_{22}) \quad (\text{B.2})$$

$$u_{21} = \eta_1(\cos(\zeta_{164})^2 f_{11} + \sin(\zeta_{164})^2 f_{21}) \quad (\text{B.3})$$

$$u_{22} = \eta_2(\cos(\zeta_{164})^2 f_{12} + \sin(\zeta_{164})^2 f_{22}) \quad (\text{B.4})$$

Solving this gives for the room temperature data from figure B.3:

$\zeta_{119} \approx 17.8^\circ$, $\zeta_{164} \approx 14.6^\circ$, $\eta_1 \approx 0.16$, $\eta_2 \approx 0.23$. This means that light with lambda plate setting 119 arrives 91 % p-polarized at the WGP, so 91 % V-polarized at the sample. And light with lambda plate setting 164 arrives 94 % p-polarized at the WGP, so 94 % H-polarized at the sample. Similarly for the 4.2K data of figure B.5: $\eta_1 \approx 0.029$, $\eta_2 \approx 0.041$. At liquid helium temperature the setting 119 implies 66 % V-polarized and 164 implies 78 % H-polarized at the sample. And for the 4.2K data of figure B.4 (as a consistency check): $\eta_1 \approx 0.021$, $\eta_2 \approx 0.032$. 119 implies 62 % V-polarized and 164 means 79 % H-polarized at the sample.

B.4 Conclusion

Using the measured values f_{ij} and the derived values ζ_i and η_i , we can convert any input to H and V components just before the sample and any output to H and V components just behind the sample.

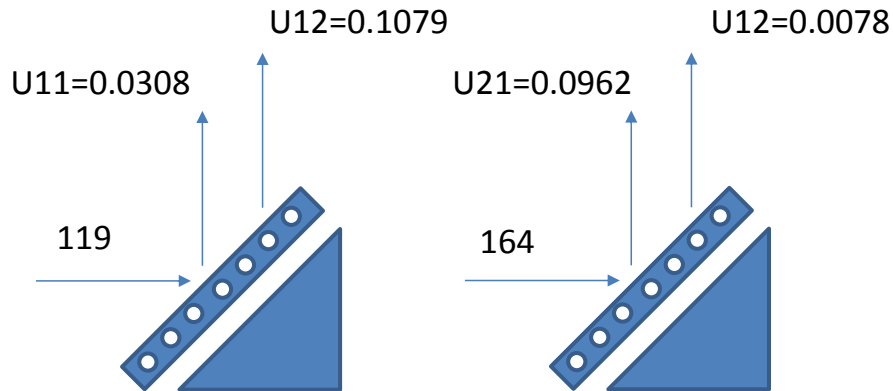


Figure B.3: Microscope output at $T = 300$ K. Data from figure 8.7a.

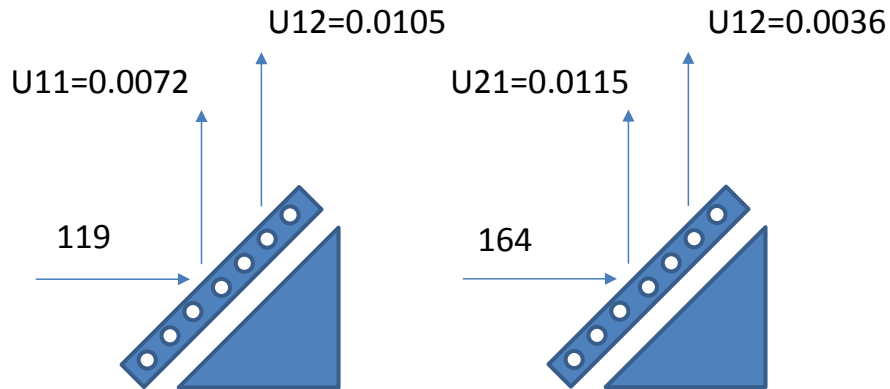


Figure B.4: Microscope output at $T = 4.2$ K. Data from figure 8.7b.

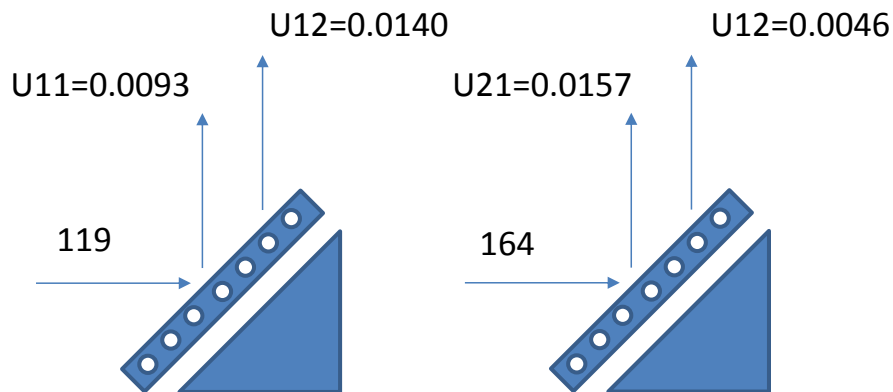
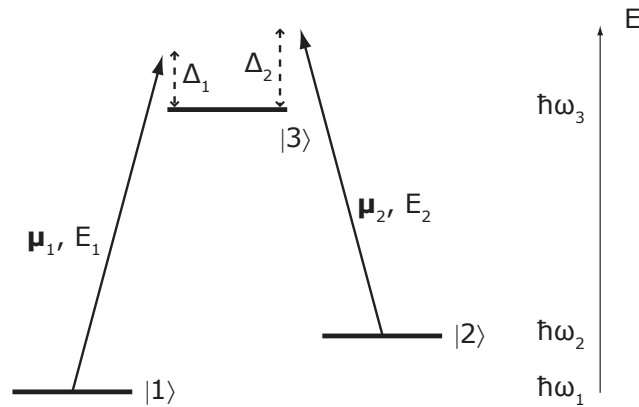


Figure B.5: Microscope output at $T = 4.2$ K. Data from figure 8.5.

Wetenschappelijke samenvatting

In dit proefschrift vormen twee onderwerpen de rode draad: Ten eerste het effect van elektromagnetisch geïnduceerde transparantie (aangeduid met de afkorting uit het engels, EIT) in gallium arsenide; en ten tweede de koppeling tussen de spins van elektronen en atoomkernen in dit materiaal.

Het eerste wordt zichtbaar gemaakt in een spectroscopische meting waarbij het materiaal belicht wordt door twee coherente lichtbronnen (lasers). Hiervoor zijn drie energieniveaus nodig met overgangen die een zogenaamde Λ -configuratie vormen, zoals afgebeeld in Figuur 1. De energieovergangen die door de lasers aangedreven worden zijn die van elektronen die gebonden zijn aan silicium atomen die tijdens het groeiproces ingebed zijn in het galliumarsenide kristal. Silicium treedt in dit geval op als donator door een extra elektron in het materiaal te introduc-



Figuur 1: Een Λ -systeem bestaande uit de energie eigentoestanden $|1\rangle$, $|2\rangle$ en $|3\rangle$ waarbij lasers de 1-3 en 2-3 overgangen aandrijven. Er is geen elektrische dipoolovergang corresponderend met de 1-2 overgang, hierdoor is de levensduur van toestand $|2\rangle$ lang vergeleken met die van $|3\rangle$.

eren. Bij voldoende lage temperaturen, $T \leq 70$ K, blijven deze elektronen gebonden aan het positief geladen donoratoom door de elektrostatische aantrekkingskracht. De zo gevormde systemen gedragen zich als atomen in het kristalrooster. De energiestructuur lijkt op die van de alkali-atomen (met één elektron in de buitenste schil) waarbij de elektronbaan echter veel groter is (effectieve Bohr straal van 99 \AA) vanwege de lage effectieve massa van het elektron als gevolg van afscherming van de lading die plaatsvindt in het kristal. In de experimenten die in dit proefschrift beschreven zijn wordt dit materiaal in een extern magneetveld geplaatst, waardoor de twee spintoestanden van het elektron energetisch gescheiden worden. Deze toestanden worden gekoppeld aan een optisch geëxciteerde toestand die bestaat uit het donorgebonden elektron plus een, eveneens gebonden aan de donor, elektron-gat paar. Dit complex van drie gelokaliseerde deeltjes heet een donorgebonden exciton.

Als de overgangen tussen deze toestanden worden aangedreven door twee lasers, zullen in de meeste gevallen ($\Delta_1 \neq \Delta_2$ in Fig. 1) processen van excitatie naar $|3\rangle$ middels foton absorptie en verval vanuit toestand $|3\rangle$ middels spontane emissie optreden. Voldoet de aandrijving echter aan de twee-foton resonantie conditie, $\Delta_1 = \Delta_2$, dan wordt het systeem in een toestand gebracht die een kwantumsuperpositie is van de toestanden $|1\rangle$ en $|2\rangle$. Het contact met de laservelden bestaat nu uit absorptie en gestimuleerde emissie, wat een coherent proces is waarbij de uitgezonden fotonen dezelfde frequentie, fase en richting hebben als de fotonen van de lasers. Het resultaat van deze aandrijvingsconfiguratie is dat de laservelden niet verstrooid worden en het materiaal dus transparant wordt op een frequentie waarop anders absorptie plaatsvindt. Als dit wordt uitgevoerd met een sterke (controle) laser en een zwakke (probe) laser dan heet dit elektromagnetisch geïnduceerde transparantie (EIT), omdat transparantie van het materiaal voor de probe laser geïnduceerd wordt door de aanwezigheid van de controle laser. Dit proces is interessant voor de ontwikkeling van optisch actieve circuit-elementen aangezien het een transistor achtig effect betreft: een transmissiekanaal wordt geopend of gesloten afhankelijk van de aanwezigheid van een tweede signaal.

Een ander belangrijk aspect is de toestand die het systeem aanneemt

onder deze condities. Na een initiële kortstondige respons wordt het in een constante toestand gebracht die bepaald wordt door de laserintensiteiten. Deze toestand is $(\Omega_2 |1\rangle - \Omega_1 |2\rangle) / \sqrt{\Omega_1^2 + \Omega_2^2}$, waar $\Omega_{1,2}$ de complexe Rabi frequenties zijn. Het vangen van het systeem in een deze superpositie van de grondtoestanden heeft de engelse benaming coherent population trapping (CPT). Dat deze toestand geen component van de optisch aangeslagen toestand $|3\rangle$ bevat heeft als gevolg dat (klassieke) statistische onzekerheid niet ontstaat op de snelle tijdschaal van spontane emissie (1.0 ns voor dit systeem), maar op de langzamere tijdschaal van elektronspin-decoherentie (gemeten als zijnde minstens 7 μ s voor dit systeem). Op tijdschalen korter dan een microseconde evolueert het systeem dus op puur kwantummechanische (deterministische) wijze. Dit, in combinatie met de mogelijkheid om de superpositie tussen toestanden $|1\rangle$ en $|2\rangle$ te beïnvloeden met de lasers op een tijdschaal van nanoseconden, maakt dit systeem tot een kandidaat voor gebruik als een kwantumbit. Er zijn momenteel verschillende voorstellen van kwantumcomputatie en kwantumcommunicatie (vooral met betrekking op cryptografie) gebaseerd op dergelijke Λ -systemen, waarvan sommige gerealiseerd zijn in het laboratorium. Waar de eerste succesvolle implementaties gedaan zijn met atomen in gasvorm, is het momenteel nog een grote uitdaging om dit te doen met systemen in de vaste stof. Het onderzoek in dit proefschrift heeft als doel om dergelijke experimenten mogelijk te maken met de donorgebonden elektronen in galliumarsenide, die als artificieel atomen gevangen in de vaste stof zouden kunnen dienen.

De bedoeling is om een ensemble van deze elektronen te gebruiken en hieraan wordt in dit proefschrift dan ook gemeten. Bij gebruik van een ensemble is de homogeniteit hiervan van groot belang. Bij sterke homogeniteit koppelen de eenheden collectief aan het laserveld, wat voor sterke licht-materie interactie zorgt. Bovendien is homogeniteit in de energetische splitsing tussen de spintoestanden van belang. Tijdens de evolutie van de geprepareerde spintoestand precedeert deze met de Larmorfrequentie. Wanneer deze ongelijk is voor de eenheden van het ensemble leidt dit tot verlies van informatie over de kwantumtoestand, in de vorm van defasering. In galliumarsenide treedt dit type inhomogeniteit

op door de aanwezigheid van kernspins in het materiaal. Deze zijn bij de huidige experimenteel haalbare temperaturen en magneetvelden niet geordend. De kernspinpolarisatie in regio's rond de verschillende dono- ratomen vertoont statistische fluctuaties en dit wordt gevoeld door de elektronspins via de hyperfijn-interactie. Omdat de elektronen een s-type golffunctie hebben (niet nul op de atomaire roosterpunten en sferisch sym- metrisch daaromheen) betreft het hier de Fermi contactinteractie tussen de elektron- en kernspins. De contactinteractie veroorzaakt een effectief magneetveld met fluctuaties die, wanneer de spins in thermodynamisch evenwicht zijn, normaal verdeeld zijn met een standaardafwijking van ongeveer 15 mT (uitgedrukt als een effectief magneetveld gevoeld door de elektronspin).

De eerste metingen van elektromagnetisch geïnduceerde transparantie, in het hierboven omschreven materiaal, worden getoond in Paragraaf 2.5. Deze laten inderdaad een snelle defaseringsstijd van 3 ns zien ten gevolge van de hyperfijn-interactie met de kernspins. De hoofddoelstelling van dit proefschrift, beschreven in hoofdstukken 4 en 5, is om deze defaseringsstijd te verlengen door de kernspinpolarisatie meer homogeen te maken. Dit brengt ons bij het tweede hoofdonderwerp, dynamische kernspinpolarisatie (met engelstalige afkorting, DNP). Dit is een methode om de kernspins uit thermodynamisch evenwicht te brengen door gebruik te maken van de nabije elektronspin en de hyperfijn koppeling. In het hier beschreven geval, waar de elektronische niveaustruktuur een Λ -systeem vormt, is het eenvoudig om de elektronspin uit thermodynamisch evenwicht te brengen door met een laser een van de twee overgangen aan te drijven. Dit proces heet optische orientatie, omdat de spin hierdoor parallel of antiparallel aan het magneetveld georiënteerd wordt. De hyperfijn koppeling zorgt ervoor dat een dergelijke elektronspinpolarisatie kan worden overgedragen aan de kernspins. Op microscopisch niveau gebeurt dan het volgende: De kernspins voelen een effectief magneetveld van de nabije elektronspin. Dit magneetveld fluctueert omdat de elektronspin relaxatieprocessen onder- gaat. De elektronspinpolarisatie herstelt zich echter zeer snel (via optische excitatie en verval) tot het evenwicht dat wordt opgelegd door de laser. Deze fluctuaties zijn van nature statistisch en bevatten frequentiecomp-

ment die resonant is met de splitsing tussen de kernspin-energieniveaus. De kernspins reageren op deze frequentiecomponent van het fluctuerende veld en kunnen daardoor van toestand veranderen.

Het aanleggen van een kernspinpolarisatie leidt slechts tot significante reductie van fluctuaties wanneer deze polarisatie de 100% benaderd. In hoofdstuk 3 van dit proefschrift laten wij zien dat dit in praktijk niet mogelijk is omdat de aangelegde kernspinpolarisatie te snel wegvloeit van de donoratomen middels een diffusie-achtig proces (in feite de dipool-dipool koppeling tussen de kernspins). Om deze reden wordt in hoofdstuk 4 een nieuw theoretisch model voorgesteld waarbij het DNP proces aangedreven wordt door twee lasers met gelijke sterkte. Dit resulteert in een terugkoppelproces voor DNP waardoor kernspin-ensembles ernaar streven om zo dicht mogelijk bij de volledig ongepolariseerde toestand te blijven. Hierdoor kunnen fluctuaties in het effectieve magnetisch veld van de kernspins (Overhauser veld genoemd) worden teruggedrongen. Door dit proces te simuleren met realistische parameters voor galliumarsenide wordt een verbetering in de elektronspinoherentietijd met een factor 7 voorspeld. Het is belangrijk dat de lasers in frequentie naar boven afwijken van de resonantie. In dat geval is er een stabiel punt waar alle systemen naar toe convergeren. Dit leidt tot een scherpere waarschijnlijkheidsdistributie voor de kernspinpolarisatie en dit zal zichtbaar worden in een scherpere EIT resonantie. Echter, wijken de lasers in frequentie naar onder af van resonantie dan zijn er twee stabiele punten. Dit leidt tot een dubbelgepiekte waarschijnlijkheidsdistributie voor de kernspinpolarisatie en uit zich in een dubbelgepiekte EIT resonantie.

De theorie ontwikkeld in hoofdstuk 4 wordt experimenteel getest in hoofdstuk 5. De verbetering van de EIT resonantie wordt hier niet gevonden. Wel wordt de splitsing van de EIT resonantie waargenomen onder de voorspelde omstandigheden. Dit is een bevestiging van het voorgestelde model. Een reden dat het reduceren van de fluctuaties niet lukt is waarschijnlijk dat de intensiteit van de lasers binnen het materiaal sterk varieert. Om deze hypothese te testen zijn nieuwe metingen nodig met een anti-reflectielaag op het materiaal en eventueel een verbeterde microscoop. Het voorgestelde effect is niet uniek voor galliumarsenide. Het is een wisselw-

erking tussen een aangedreven Λ -systeem en een omgevingsvariabele. Het kan dus in principe ook waargenomen worden in andere gelokaliseerde spins in de vaste stof waarbij het doel is om een meer homogene omgeving te creëren. De overige hoofdstukken van dit proefschrift presenteren instrumentatie-verbeteringen en karakteristaties van het galliumarsenide materiaal die een basis vormen voor de resultaten van hoofdstuk 4 en hoofdstuk 5.

Scientific summary

In this PhD thesis two subjects are central: Firstly, the effect of electromagnetically induced transparency (EIT) in gallium arsenide; and secondly, the coupling between the spins of electrons and nuclei in this material.

The former can be made visible in a spectroscopic measurement where the material is illuminated by two coherent light sources (lasers). This requires three energy levels with transitions that form a so-called Λ -configuration, such as depicted in Figure 1. The transitions that are driven by the lasers are associated with electrons that are bound to silicon atoms (D^0 systems) that are embedded in the gallium arsenide crystal during the growth process. In this case silicon acts as a donor by introducing an extra electron in the material. At sufficiently low temperatures, $T \leq 70$ K, these electrons

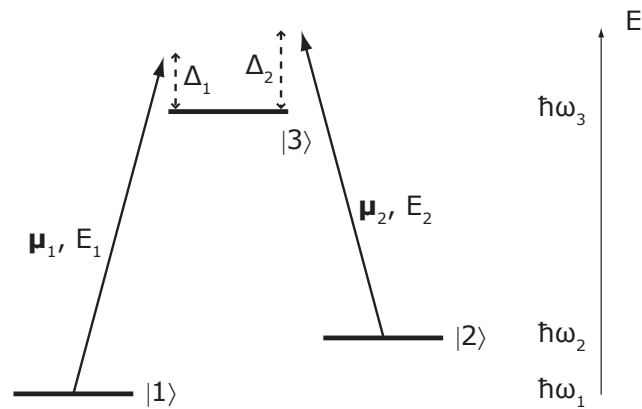


Figure 1: A Λ -system consisting of energy eigenstates $|1\rangle$, $|2\rangle$ and $|3\rangle$ for which lasers drive the 1-3 and 2-3 transitions. There is no electric dipole transition corresponding to the 1-2 transition. Because of this the lifetime of state $|2\rangle$ is long as compared to that of $|3\rangle$.

remain bound to the positively charged donor atom by the electrostatic force. The localized systems hence formed act like atoms trapped in the crystal lattice. Their energy structure resembles that of alkali atoms (with one electron in the outer shell), but their electronic orbit is much larger (effective Bohr radius of 99 Å) because of the low effective mass of the electron as a consequence of charge screening in the crystal. In the experiments that are described in this thesis, the material is placed in an external magnetic field, which separates the electron spin states in energy. These states are coupled to an optically excited state that exists of the donor-bound electron plus an electron-hole pair that is also bound to the donor. This complex of three localized particles is called donor-bound exciton.

If the transitions between these states are driven by two lasers this will in most cases ($\Delta_1 \neq \Delta_2$ in Fig. 1) result in processes of excitation to $|3\rangle$ by means of photon absorption and decay from state $|3\rangle$ by spontaneous emission. However, if the driving fulfills the two-photon resonance condition, $\Delta_1 = \Delta_2$, the system is brought into a state that is a quantum superposition of states $|1\rangle$ and $|2\rangle$. The contact with the laser fields now consists of absorption and stimulated emission, which is a coherent process in which the emitted photons have the same frequency, phase and direction as the laser photons. The result of this driving configuration is that laser photons are not scattered and hence the material becomes transparent at a frequency at which it normally would absorb light. When this procedure is carried out with a strong (control) laser and a weak (probe) laser it is called electromagnetically induced transparency (EIT), because transparency of the material to the probe light is induced by the presence of the control laser. This process is of interest for the development of optically active circuit elements because it resembles the behavior of a transistor: a transmission channel is open or closed depending on the presence of a secondary signal.

Another important aspect is the state that the system assumes under these conditions. After an initial short transient response, it is brought in a steady state that is governed by the laser powers. This state is $(\Omega_2 |1\rangle - \Omega_1 |2\rangle) / \sqrt{\Omega_1^2 + \Omega_2^2}$, where $\Omega_{1,2}$ are the complex Rabi frequencies.

Trapping the system in this ground state superposition is called coherent population trapping (CPT). That this state does not carry a component of the optically excited state $|3\rangle$ has as a consequence that (classical) statistical uncertainty of the state does not emerge at the timescale of spontaneous emission (1.0 ns for this system), but at the slower timescale of the electron spin decoherence (measured to be at least $7\ \mu\text{s}$ for this system). At times shorter than roughly a microsecond the system can be considered to evolve in a pure quantum mechanical (deterministic) fashion. This, in combination with the possibility to influence the superposition of states $|1\rangle$ and $|2\rangle$ with the lasers at the nanosecond timescale, makes this system a candidate for use as a quantum bit. Currently there are various proposals for quantum computation and quantum communication (mainly with relevance for cryptography) that are based on Λ -systems, some of which have been realized in the laboratory. While the first successful implementations were done using atomic gases, it is currently still a great challenge to do this with systems in solid state. The research in this thesis has the goal to make such experiments possible using donor-bound electrons in gallium arsenide, which could serve as artificial atoms trapped in solid state.

The intention is to use an ensemble of these electrons and this is what is being measured in this thesis. When using an ensemble, its homogeneity is of great importance. With strong homogeneity the individual systems couple collectively to the laser field, ensuring strong light-matter interaction. Furthermore, homogeneity in the energy splitting between the spin states is crucial. During evolution, the prepared spin state precesses with the Larmor frequency. When this is not equal for the various members of the ensemble this leads to loss of information about the quantum state, in the form of dephasing. In gallium arsenide this type of inhomogeneity arises due to the presence of nuclear spins in the material. At the currently achievable experimental temperatures and magnetic fields these spins are not ordered. The nuclear spin polarization in regions around the various donor atoms shows statistical fluctuations and these are felt by the electron spins via the hyperfine interaction. Because the electrons have an s-type wave function (non-zero at the lattice points and spheri-

cally symmetric around them) this concerns the Fermi contact interaction between the electron and nuclear spins. The contact interaction gives rise to an effective magnetic field with fluctuations that are, when the spins are in thermal equilibrium, normally distributed with standard deviation of about 15 mT (expressed as an effective magnetic field felt by the electron spin).

The first measurements of electromagnetically induced transparency, in the material as described above, are demonstrated in Section 2.5. These indeed show a fast dephasing time of 3 ns due to the hyperfine interaction with the nuclear spins. The main goal of this thesis, contained in Chapters 4 and 5, is to extend this dephasing time by making the nuclear spin polarization more homogeneous throughout the material. This brings us to the second main topic, dynamic nuclear spin polarization (DNP). This is a method for bringing the nuclear spins out of thermodynamic equilibrium by making use of the nearby electron spin and the hyperfine coupling. In the case described here, where the electronic level structure forms a Λ -system, it is straightforward to bring the electron spin out of thermal equilibrium by driving one of the two transitions with a laser. This process is called optical orientation, because the spin is oriented parallel or antiparallel to the magnetic field. The hyperfine coupling enables that the electron spin polarization is carried over to the nuclear spins. At a microscopic level the following happens: The nuclear spins sense an effective magnetic field of the nearby electron spin. This magnetic field fluctuates because the electron undergoes relaxation processes. The electron spin polarization however recovers very quickly (via optical excitation and decay) to reach the equilibrium that is dictated by the laser. These fluctuations are of statistical nature and their spectrum contains a frequency component that is resonant with the nuclear spin level splitting. Nuclear spins react to this frequency component of the fluctuating field, which enables them to change their state.

Inducing a nuclear spin polarization only leads to significant reduction of the fluctuations when this polarization approaches 100%. In Chapter 3 of this thesis we show that in practice this is cannot be achieved because the induced spin polarization flows away too quickly by a diffu-

sion type of process (which is in fact dipole-dipole coupling between the nuclear spins). For this reason we introduce in Chapter 4 a new model in which the DNP is driven by two lasers of equal strength. This results in a feedback process for DNP that causes all nuclear spin ensembles to tend towards the maximally unpolarized state. By this means fluctuations in the effective magnetic field of the nuclear spins (called Overhauser field) can be reduced. By simulating this process using realistic parameters for the case of gallium arsenide an improvement of the electron spin dephasing time by a factor 7 is predicted. It is important that the lasers are blue detuned (optical frequency slightly larger than the corresponding transition). In that case there is one stable point towards which all systems converge. This leads to more sharply peaked probability distribution for the nuclear spin polarization and this in turn will reveal itself as a sharper EIT resonance. On the other hand, when the lasers are red detuned there are two stable points. This leads to a doubly-peaked probability distribution for the nuclear spin polarization and results in a doubly-peaked EIT resonance

The theory developed in Chapter 4 is tested experimentally in Chapter 5. The improvement of the EIT resonance is not found in these results. However, the predicted splitting is observed for the red-detuned circumstances. This confirms the validity of the proposed model. The reason for not observing a reduction in the nuclear spin fluctuations for the blue-detuned case is probably that the intensity of the lasers inside the material varies strongly (and the proposed effect is intensity dependent). Testing hypothesis requires new measurements using a different sample structure, including an anti-reflection coating and perhaps an improved microscope design. The proposed effect is not unique to gallium arsenide. It is an example of interplay between a driven Λ -system and a particular environment variable. Hence it could in principle be observed in other localized spin systems in solid state, and be of use when the goal is to create a more homogeneous environment. The other chapters in this thesis present instrumentation improvements and characterization studies of the gallium arsenide material that form a basis for the results of Chapters 4 and 5.

List of publications

1. Electromagnetically induced transparency with an ensemble of donor-bound electron spins in a semiconductor
Maksym Sladkov, A. U. Chaubal, M. P. Bakker, A. R. Onur, D. Reuter, A. D. Wieck, C. H. van der Wal, *Phys. Rev. B* **82**, 121308(R) (2010).
2. Electromagnetically induced transparency in low-doped n-GaAs
C. H. van der Wal, M. Sladkov, A. U. Chaubal, M. P. Bakker, A. R. Onur, D. Reuter, A. D. Wieck, *AIP Conf. Proc.* **1399**, 1039 (2011) [Proceedings of the 30th International Conference on the Physics of Semiconductors (ICPS 2010)].
3. Quantumoptica met spins in halfgeleiders [in Dutch]
Sander Onur, Caspar van der Wal, *Nederlands Tijdschrift voor Natuurkunde* **78**, 231 (juli 2012).
4. Two-laser dynamic nuclear polarization with semiconductor electrons: feedback, suppressed fluctuations, and bistability near two-photon resonance
A. R. Onur, C. H. van der Wal, submitted (2014); available at arXiv:1409.7576.
5. Analysis of optical differential transmission signals from co-propagating fields in a lambda system medium
J. P. de Jong, A. R. Onur, D. Reuter, A. D. Wieck, C. H. van der Wal, submitted (2014); available at arXiv:1409.7679.
6. All-optical coherent population trapping with defect spin ensembles in silicon carbide
Olger V. Zwier, Danny O'Shea, Alexander R. Onur, Caspar H. van der Wal, *Scientific Reports* **5**, 10931 (2015).
7. Stabilizing nuclear spins around semiconductor electrons via the interplay of optical coherent population trapping and dynamic nuclear polarization
A. R. Onur, J. P. de Jong, D. O'Shea, D. Reuter, A. D. Wieck, C. H. van der Wal, submitted (2015); available at arXiv:1501.04524.
8. Spectral dependence of optically induced dynamic nuclear spin polarization in n-GaAs
A. R. Onur, A.U. Chaubal, D. Reuter, A. D. Wieck, C. H. van der Wal, in preparation;

